Institute of Thermoelectricity, Academy of Sciences and Ministry of Education and Science of Ukraine

Journal of THERMOELECTRICITY

International Research

Founded in December, 1993

published 6 times a year

No. 3 *2016*

Editorial Board

International Editorial Board

Founders – National Academy of Sciences, Ukraine
Institute of Thermoelectricity of National Academy of Sciences and Ministry of Education and Science of Ukraine

Certificate of state registration № КВ 15496-4068 ПР

Editorial office manager N. Kharbaka

Approved for printing by the Academic Council of Institute of Thermoelectricity of the National Academy of Sciences and Ministry of Education and Science, Ukraine

Address of editorial office:
Ukraine, 58002, Chernivtsi, General Post Office, P.O. Box 86.
Phone: +(380-372) 90 31 65.
Fax: +(380-3722) 4 19 17.
E-mail: jt@inst.cv.ua
http://www.jt.inst.cv.ua

Signed for publication 25.07.16. Format 70×108/16. Offset paper №1. Offset printing.
Printer's sheet 11.5. Publisher's signature 9.2. Circulation 400 copies. Order 5.

Printed from the layout original made by "Journal of Thermoelectricity" editorial board
in the printing house of "Bukrek" publishers,
10, Radischev Str., Chernivtsi, 58000, Ukraine

CONTENTS

Ya.O. Shablovsky

Ya.O. Shablovsky

P.O. Sukhoi State Technical University of Gomel,
48, October Av., Gomel, 246746, Belarus

ELECTRICALLY AND MAGNETICALLY INDUCED CRYOGENERATION IN CRYSTALLINE DIELECTRICS

Thermodynamic analysis of the induced caloric response of dielectric materials to the application of the electric and magnetic fields is performed. Quantitative characteristics of the electrocaloric and magnetocaloric effects are determined. It is shown that the electrocaloric effect (ECE) is not reverse to the pyroelectric effect, and the magnetocaloric effect (MCE) is not reverse to the pyromagnetic effect. For this reason the electrocaloric effect can be observed in nonferroelectric dielectrics, and the magnetocaloric effect can be observed in nonferromagnetic materials.

Key words: cryogeneration, electrocaloric effect, magnetocaloric effect.

Introduction

One of the promising directions of thermoelectricity development is creation of new types of thermoelements that can expand the range of technical capabilities implemented nowadays by means of "classical" thermoelements [1, 2]. This applies especially to the development of new cooling element designs.

The need for them is caused by increasing miniaturization of microelectronic elements whose stable operation requires extraction of rather large (up to 1 kW/cm^2) heat flows from very small areas on the surface of microcircuit. At the present time this technical task is successfully solved by thermoelectric methods [3], however in the future the application of thermoelectric elements for cooling and thermal stabilization of microelectronic devices may run into limitations caused by relatively low cooling capacity of such elements [4].

A possible way to overcome this difficulty is cryogeneration due to electrically and magnetically induced caloric effects in crystals. Many specialists are convinced (see, for instance [5, 6]) that solid-state cryogenerators are capable of supplanting traditional vapor compression refrigerating units. For that reason a search for materials suitable for creation of working media of such cryogenerators has become much more active.

It must immediately be emphasized that this search is pursued exceptionally among substances having a domain structure, namely ferroelectric and ferromagnetic materials. It is commonly supposed [5, 7] that the efficiency of material application as electrocaloric (or magnetocaloric) is determined by its structure capacity for spontaneous electrical (or magnetic) ordering. In light of this, electrocaloric materials are traditionally selected from among ferroelectric materials, and magnetocaloric materials – from among ferromagnetic materials. In so doing, for cryogeneration use is made of the temperature region close to the point of ferroelectric (or ferromagnetic) conversion. In this region, the domaining materials have extremely high susceptibility to application of electromagnetic field. However, the temperature instability of characteristics of such materials is also

very high. As a result, it appears that efficient cryogeneration requires unique materials with practically incompatible characteristics.

L.P. Bulat was the first to call attention to this peculiarity [4, 6] and he suggested that highly intensive magnetocaloric effect is also possible in nonferromagnetic materials. This idea was further developed in the present paper. In the following we will carry out the thermodynamic analysis of the caloric properties of crystalline materials induced by the electromagnetic effect, and reveal a number of nontrivial qualitative and quantitative regularities of the electrocaloric and magnetocaloric effects in crystalline dielectrics.

Thermodynamic analysis

On introducing the sample substance into electric or magnetic field, an own field is created in the bulk of the sample which differs from the initial field affecting the sample from the outside. If the sample substance in electric field of intensity E is quasi-two-dimensional (single-crystal plate perpendicular to field E), the intensity E' of electric field in the bulk of such sample is determined by the equality [8]

$$E' = \frac{E}{\varepsilon}, \tag{1}$$

where ε is dielectric permeability of the substance. If, however, the sample substance in the electric field is not quasi-two-dimensional, the electric field intensity in the bulk of this substance can be estimated by the formula [8]

$$E' = \frac{3\bar{\varepsilon}}{\varepsilon + 2\bar{\varepsilon}} E, \tag{2}$$

where $\bar{\varepsilon}$ is dielectric permeability of the medium surrounding the sample substance. In the case when the sample substance is exposed to a magnetic field with induction B, in the bulk of this substance the magnetic induction B' and magnetic field intensity h' will be, respectively [9]

$$B' = \mu B, \qquad h' = \frac{B}{\mu_0 (1 + \iota\varsigma)}. \tag{3}$$

Here μ_0 is magnetic permeability of vacuum, $\mu = (1 + \varsigma)$ is magnetic permeability of the substance, ς is magnetic susceptibility of the substance, ι is degaussing factor governed by the sample substance geometry (see [9]).

Elementary work δR to create own fields in the substance is expressed through volume integrals in the form of the following equality [10]:

$$\delta R = \int_{\upsilon} E' \delta D \, d\upsilon + \int_{\upsilon} h' \delta B' d\upsilon, \tag{4}$$

where $D = \varepsilon_0 \varepsilon E'$ is electric induction, ε_0 is dielectric permeability of vacuum. As long as the values E', D, h' and B' in Eq. (4) refer to the unit volume of the substance, the expression for differential of molar internal energy U of homogeneous substance in electromagnetic field is given by:

$$dU = TdS - p_{\circ} dV + V E' dD + V h' dB', \tag{5}$$

where T is temperature, S is molar entropy, V is molar volume of substance, $p_{\circ}$ is pressure of medium surrounding the sample substance.

The sample on which work δR is performed is not in thermally isolated state. Therefore, said work determines not only a change in the bulk of the sample substance, but also a change in its entropy. Indeed, substituting (1) – (3) into (5), we get that when the substance is exposed to electric field

$$dU = TdS - p_\circ dV + V\,d(LE^2) = TdS - (p_\circ + LE^2)dV + d(VLE^2), \tag{6}$$

and when it is exposed to magnetic field

$$dU = TdS - p_\circ dV + V\,d(\ell B^2) = TdS - (p_\circ + \ell B^2)dV + d(V\ell B^2), \tag{7}$$

where
$$\ell = \frac{\mu}{2\mu_0(1+\varsigma)}. \tag{8}$$

In so doing, for quasi-two-dimensional single-crystal dielectrics

$$L = \frac{\varepsilon_0}{2\varepsilon}. \tag{9}$$

If, however, the sample substance cannot be considered quasi-two-dimensional, then

$$L = \frac{9\varepsilon_0 \varepsilon \overline{\varepsilon}^2}{2(\varepsilon + 2\overline{\varepsilon})^2}. \tag{10}$$

From (6) and (7) it follows that increments in molar internal energy and molar entropy of substance due to electric field (Δ_e) and magnetic field (Δ_m) are expressed by the equalities

$$\Delta_e U = VLE^2, \qquad \Delta_m U = V\ell B^2, \tag{11}$$

$$\Delta_e S = \frac{VLE^2}{T}, \qquad \Delta_m S = \frac{V\ell B^2}{T}. \tag{12}$$

Pressure $p = -\left(\partial U/\partial V\right)_S$ corresponding to thermodynamic equilibrium of the sample substance in electromagnetic field is determined by the equality

$$p = p_\circ + p_e + p_m \tag{13}$$

where

$$p_e = LE^2, \qquad p_m = \ell B^2. \tag{14}$$

The isobaric-isothermal increments of molar enthalpy $H = U + pV$ and molar Gibbs energy $G = U + pV - TS$ caused by exposure to electric and magnetic fields are expressed by the equalities

$$\Delta_e G = p_e V, \qquad \Delta_m G = p_m V; \tag{15}$$

$$\Delta_e H = 2p_e V, \qquad \Delta_m H = 2p_m V, \tag{16}$$

and molar free energy $A = U - TS$ of substance in electromagnetic field is not changed.

Discussion of the results

A quantitative characteristic of ECE is electrocaloric coefficient $\Xi_e = \left(\partial T/\partial E\right)_S$. Let us use formal thermodynamic equations

$$\left(\frac{\partial T}{\partial E}\right)_S = -\left(\frac{\partial S}{\partial E}\right)_T \frac{T}{C_E}, \tag{17}$$

$$C_E = C_p - T\left(\frac{\partial V}{\partial T}\right)_p \left(\frac{\partial p}{\partial T}\right)_E, \tag{18}$$

where C_p is isobaric heat capacity, C_E is heat capacity at constant electric field. From (13), (14) it follows that

$$\left(\frac{\partial p}{\partial T}\right)_E = E^2 \cdot \left(\frac{\partial L}{\partial T}\right)_E.$$

The value $\left(\partial L/\partial T\right)_E$ is governed by the temperature dependence of dielectric permittivity ε. However, if a dielectric is not ferroelectric, the above temperature dependence can be neglected: $\left(\partial L/\partial T\right)_E \approx 0$. Therefore, for nonferroelectric dielectrics instead of (18) we will have $C_E = C_p$. Then coming back to equality (17), with regard to (12) we will get:

$$\Xi_e = -\frac{2VLE}{C_p}. \tag{19}$$

From (19) it follows that if electric field intensity changes with time *t* by the law *E*(*t*), by the moment $t = \tau$ the temperature of nonferromagnetic crystal will change by the value

$$\Delta T_e(\tau) = -\frac{2VL}{C_p}\int_0^\tau E(t)\frac{dE}{dt}\,dt, \tag{20}$$

where the moment of onset of electric field intensity variation is taken to be time reference point $(t = 0)$.

Similarly, using the equalities

$$\left(\frac{\partial T}{\partial B}\right)_S = -\left(\frac{\partial S}{\partial B}\right)_T \frac{T}{C_B}, \qquad C_B = C_p - T\left(\frac{\partial V}{\partial T}\right)_p \left(\frac{\partial p}{\partial T}\right)_B,$$

where C_B is heat capacity at constant magnetic induction, for magnetocaloric coefficient $\Xi_m = \left(\partial T/\partial B\right)_S$ we obtain:

$$\Xi_m = -\frac{2V\ell B}{C_p}. \tag{21}$$

Hence it follows that if magnetic induction changes with time *t* by the law *B*(*t*), by the moment $t = \tau$ the temperature of nonferromagnetic substance will vary by the value

$$\Delta T_m(\tau) = -\frac{2V\ell}{C_p}\int_0^\tau B(t)\frac{dB}{dt}\,dt, \tag{22}$$

where the moment of onset of magnetic induction variation is taken to be time reference point.

Formulae (19) – (22) show that the intensity of induced caloric effects is the higher, the larger molar volume of caloric material and the lower its heat capacity, as it was to be expected on the basis of traditional crystallographic concepts (see, for instance, [11]). At the same time, the results

obtained encourage to reconsider common point of view that only substances having domain structure can be efficient caloric materials.

By tradition, ECE is considered as an effect opposite to pyroelectric effect [11]. In reality it is not the case. In conformity with general differential thermodynamic relations [12], we have the equality

$$\left(\frac{\partial P}{\partial T}\right)_E = \left(\frac{\partial S}{\partial E}\right)_T = -\frac{\Xi_e C_E}{T}. \tag{23}$$

It is essential that P value in Eq. (23) is full electric polarization of substance including not only spontaneous (pyroelectric) polarization, but also induced polarization, created by external electric field. For this reason ECE is not only an effect opposite to pyroeffect, but even is not in a direct relationship with it.

This conclusion has an important consequence: the possibility of ECE observation is not restricted by pyroelectric materials. On account of (9), (10) and (19), the requirement $\Xi_e \neq 0$ is met fir all dielectric materials (for electrically conducting media $\Xi_e = 0$, since for such media $\varepsilon \to \infty$, in consequence of which $L = 0$). In so doing, ferroelectrics do not have evident advantages. As is seen from (20), the efficiency of electrocaloric cryogeneration is determined not only by own characteristics of material, but also by the shape of its sample {cf. formulae (9) and (10)}, as well as by the rate of increase of external electric field intensity.

Special attention should be paid to the above dependence of the efficiency of electrocaloric cryogeneration on the geometrical shape of working medium. In the course of experimental data processing [13 – 54] by formulae (9) and (10) we have calculated the values of parameter L for the best studied dielectric crystals (see the Table). Calculations show that the transition from a quasi-two-dimensional to a three-dimensional sample matches a change in the value of parameter L by a factor of 8 – 10.

Table

Dielectric properties of electrocaloric materials

Substance	Parameter L		Substance	Параметр L		Substance	Параметр L	
	Quasi-two-dimensional sample, $L \cdot 10^{13}$	Three-dimensional sample, $L \cdot 10^{12}$		Quasi-two-dimensional sample, $L \cdot 10^{13}$	Three-dimensional sample, $L \cdot 10^{12}$		Quasi-two-dimensional sample, $L \cdot 10^{13}$	Three-dimensional sample, $L \cdot 10^{12}$
AgBr	3.379	2.289	$CaCeO_3$	2.108	1.582	*GaP*	4.137	2.643
AgCl	3.599	2.397	CaF_2	5.251	3.088	*GaSb*	2.750	1.958
AgI	6.324	3.443	$Ca(NO_3)_2$	6.769	3.573	*Ge*	2.767	1.968
Ag_2O	5.031	3.006	*CaO*	3.752	2.469	α-HIO_3	1.581	1.240
AlAs	4.401	2.756	$CaWO_4$	1.346	1.076	$HgCl_2$	3.162	2.179
AlP	4.517	2.804	$CaZrO_3$	1.581	1.240	*HgSe*	1.723	1.335
$AlPO_4$	3.144	2.170	*CdO*	2.021	1.528	*HgTe*	2.108	1.582
AlSb	3.677	2.434	*CdS*	1.525	1.201	*InAs*	3.053	2.122
$(AlF)_2SiO_4$	2.197	1.636	*CdSe*	1.473	1.166	*InP*	3.525	2.361
Al_2O_3	1.595	1.249	$CdSnAs_2$	3.231	2.214	*InSb*	2.501	1.817
BP	3.816	2.499	*CdTe*	4.257	2.695	*KBr*	9.262	4.143

Table (continued)

Substance	Parameter L		Substance	Параметр L		Substance	Параметр L	
	Quasi-two-dimensional sample, $L \cdot 10^{13}$	Three-dimensional sample, $L \cdot 10^{12}$		Quasi-two-dimensional sample, $L \cdot 10^{13}$	Three-dimensional sample, $L \cdot 10^{12}$		Quasi-two-dimensional sample, $L \cdot 10^{13}$	Three-dimensional sample, $L \cdot 10^{12}$
$BaCl_2$	4.513	2.802	Co_2O_3	4.616	2.844	KCl	9.459	4.179
BaF_2	6.048	3.358	$CsBr$	6.800	3.582	KF	7.317	3.720
$Ba(NO_3)_2$	8.943	4.083	$CsCl$	6.149	3.389	KI	8.962	4.087
BaO	1.302	1.045	CsI	7.835	3.847	KNO_2	1.771	1.366
$BaZrO_3$	2.214	1.646	$CuBr$	5.534	3.187	KNO_3	8.854	4.066
BeO	6.023	3.350	$CuCl$	4.427	2.767	$LaScO_3$	1.476	1.167
$Bi_4(GeO_4)_3$	2.767	1.968	CuI	6.811	3.584	$LiBr$	3.659	2.425
$Bi_{12}SiO_{20}$	1.265	1.019	EuF_2	5.749	3.261	$LiCl$	4.006	2.585
C	7.794	3.837	$GaAs$	3.379	2.289	LiF	4.776	2.908
$CaCO_3$	1.800	1.385	GaN	1.506	1.188	$LiGaO_2$	1.876	1.435
LiI	4.014	2.588	$PbBr$	1.476	1.167	SrF_2	5.757	3.263
Li_2GeO_3	1.652	1.287	PbI_2	2.128	1.594	$Sr(NO_3)_2$	8.306	3.952
MgF_2	8.943	4.083	$Pb(CO_3)_2$	1.845	1.415	SrO	3.329	2.264
MgO	4.517	2.804	$PbCl_2$	1.321	1.059	$SrSO_4$	3.850	2.514
$MgSO_4$	5.399	3.140	PbF_2	1.511	1.192	β-Ta_2O_5	1.845	1.415
$MgTiO_3$	2.459	1.793	$Pb(NO_3)_2$	2.635	1.894	ThO_2	2.342	1.724
MnO	2.446	1.785	PbO	2.012	1.522	$TlBr$	1.481	1.171
NH_4Cl	6.361	3.454	PbO_2	1.703	1.321	$TlCl$	1.388	1.106
NH_4I	7.633	3.798	$RbBr$	9.090	4.111	$TlNO_3$	2.683	1.921
$NaBr$	7.391	3.738	$RbCl$	9.016	4.097	Tl_3TaS_4	3.304	2.251
$NaBrO_3$	7.767	3.830	RbF	7.491	3.763	Tl_3TaSe_4	4.383	2.749
$NaCl$	7.877	3.856	RbI	8.962	4.087	Tl_3VS_4	3.162	2.179
$NaClO_3$	8.384	3.969	$RbInSO_4$	6.463	3.485	UO_2	1.845	1.415
$NaClO_4$	7.686	3.811	S	3.647	2.419	$Y_3Al_5O_{12}$	3.784	2.484
NaF	7.378	3.735	Se	7.378	3.735	ZnO	1.500	1.184
NaI	6.708	3.555	Si	3.720	2.454	α-ZnS	1.703	1.321
$NaSO_4$	5.604	3.212	α-SiO_2	3.196	2.197	β-ZnS	5.334	3.117
$NdAlO_3$	2.530	1.834	Sm_2O_3	2.059	1.551	$ZnSe$	4.865	2.943
$NdScO_3$	1.640	1.279	SnO_2	1.845	1.415	$ZnTe$	4.383	2.749
Ni_2O_3	3.440	2.319	$SrCl_2$	4.817	2.924			

Making evident formal replacements and redesignations in the reasoning related to Eq. (23), it is easy to show in a similar way that MCE is not an effect opposite to pyromagnetic effect, therefore it can be observed not only in ferromagnetic materials. From formulae (21), (22) it is seen that by the main formal signs MCE is similar to ECE: the efficiency of magnetocaloric cryogeneration is determined by the shape of time-based sweep of magnetic induction and the sample geometry. However, the governing factor is the type of the dependence $B(t)$. Due to the fact that in ferromagnetic materials the magnetic permeability μ is slightly different from unity, and the magnetic susceptibility $\varsigma \ll 1$, own magnetic properties of

such materials scarcely affect MCE: according to formula (8) for nonferromagnetic materials $\ell \approx \frac{1}{2\mu_0} = 3.979 \cdot 10^5$ m/H .

The possibilities of electrically and magnetically induced cryogeneration described by formulae (20) and (22) are naturally compared to "classical" electrically induced solid-state cryogeneration due to the Peltier effect.

Dimensional factor is the main characteristic giving a clear advantage to thermoelectric coolers over the above described cryogeneration methods. Electrocaloric and, even more, magnetocaloric coolers are inferior to thermoelectric coolers in compactness, as long as in view of formulae (20) and (22) for the implementation of electrically and magnetically induced cryogeneration it is necessary to have devices assuring cyclic changes of the electrical and magnetic fields with the asymmetrical shape of time-base sweep.

In a variety of factors (noise-free operation, ecological safety, possibility of quick cooling and "cooling-heating" reversal) the electrically and magnetically induced cryogeneration is similar to thermoelectric cooling. Of greatest interest are the advantages of electrically and magnetically induced cryogeneration as compared to thermoelectric cooling.

These advantages are primarily due to the absence of the Joule losses owing to which the coefficient of performance η of corresponding generators can be much in excess of the coefficient of performance of the most efficient thermoelectric coolers. Namely, at electrocaloric cryogeneration

$$\eta_e = \frac{T_0 - \Delta T_e}{\Delta T_e}, \tag{24}$$

and at magnetocaloric cryogeneration

$$\eta_m = \frac{T_0 - \Delta T_m}{\Delta T_m}, \tag{25}$$

where T_0 is initial temperature (ambient temperature), and ΔT_e and ΔT_m are determined by formulae (20) and (22), respectively.

Another important advantage is a relatively weak dependence of the intensity of electrically induced and, in particular, magnetically induced cryogeneration on the properties of working medium. As mentioned above, the decisive factors are the geometrical shape of working medium and, even more, the shape of time-base sweep of electrical (or magnetic) field. The latter factor is of particular significance, since it eliminates not only the necessity of seeking "efficient" materials, but also the need for using superstrong fields. Indeed, optimizing the shape of time-base sweep of the field, i.e. increasing the value $\frac{dE}{dt}$ or $\frac{dB}{dt}$, one can achieve high values of coefficients of performance η_e and η_m even in relatively weak electromagnetic fields [see formulae (20), (22), (24), (25)].

Conclusion

1. A thermodynamic analysis of induced caloric response of dielectric materials to application of electric and magnetic field was performed [formulae (6) – (16)], which allowed quantitative description of ECE and MCE [formulae (19) – (22)].

2. It was shown that ECE is not an effect reverse to pyroelectric effect, and MCE is not an effect reverse to pyromagnetic effect. For this reason ECE can be observed in nonferromagnetic dielectrics, and MCE can be observed in nonferromagnetic materials.
3. It was established that the influence of caloric material own characteristics on the efficiency of cryogeneration through ECE and MCE is not critically important. The decisive factor is the rate of increase in the intensity of external electromagnetic field. This conclusion is in agreement with the results of [55], where the effect of influence of electric field timebase form on the intensity of ECE was experimentally observed.

References

1. L.I.Anatychuk, Rational Areas of Investigation and Application of Thermoelectricity, *J.Thermoelectricity* 1, 5 – 20 (1993).
2. A.G.Samoilovich, *Thermoelectric and Thermomagnetic Methods of Energy Conversion* (Chernivtsi: Ruta, 2006), 226 p.
3. L.P.Bulat, *Thermoelectric Cooling* (Saint-Petersburg, Saint-Petersburg University of Low-Temperature and Food Technologies, 2002), 147 p.
4. L.P.Bulat, O.V.Pakhomov, and A.S.Starkov, Nontraditional Methods for Thermal Stabilization of Photo- and Microelectronics Elements, *Applied Physics* 2, 73 – 80 (2010).
5. Yu.V.Sinyavsky, G.E.Lugansky, Experimental Investigation of the Breadboard Prototype and Predicted Characteristics of Electrocaloric Refrigerators, *Doklady AN* **323**(2), 322 – 325 (1992).
6. L.P.Bulat, Solid-State Cooling Systems, *J.Thermoelectricity* 3, 15 – 21 (2007).
7. I.N.Flerov, Caloric Effects in Solids and Their Application Prospects, Izvestiya *of Saint-Petersburg University of Low-Temperature and Food Technologies* 1, 41 – 63 (2008).
8. A.N.Gubkin, *Theory of Dielectric Polarization* (Moscow: Vysshaya Shkola, 1971), 272 p.
9. Ya.G.Dorfman, *Magnetic Properties and Substance Structure* (Moscow: State Publ. of Technical and Theoretical Literature, 1955, p.60), 376 p.
10. L.D.Landau, E.M.Lifshits, *Electrodynamics of Continuous Media* (Moscow: Nauka, 1982, p.71)
11. I.S.Zheludev, *Physics of Crystalline Dielectrics* (Moscow: Nauka, 1968), 464 p.
12. V.V.Sychev, *Differential Equations of Thermodynamics* (Moscow, MEI Publ., 2010), 256 p.
13. P.T.Narasimhan, R. S. Krishnan, *Dielectric Properties of Ionic Crystals*. *Progress in Crystal Physics. Vol. 1, Thermal, Elastic and Optical Properties* (Madras: S. Viswanathan, 1958, Ch. 7, P. 184 – 198).
14. G.L.Bottger, A.L.Geddes, Infrared Lattice Vibrational Spectra of *AgCl*, *AgBr*, and *AgI*, *The Journal of Chemical Physics* 46(8), 3000 – 3004 (1967).
15. S.Roberts, Dielectric Constants and Polarizabilities of Ions in Simple Crystals and Barium Titanate, *Physical Review* **76**(8), 1215 – 1220 (1949).
16. S.Adachi, *GaAs and Related Materials: Bulk Semiconducting and Superlattice Properties* (Singapore: World Scientific, 1994), 675 p.
17. L.I.Berger, *Semiconductor Materials* (Boca Raton, Florida: CRC Press, Inc., 1997), 496 p.
18. *Springer Handbook of Condensed Matter and Materials Data* / Ed.: W. Martienssen, H. Warlimont. – Berlin-Heidelberg: Springer, 2005. – 1121 p.
19. K.F.Young, H.P.R.Frederikse, Compilation of the Static Dielectric Constant of Inorganic Solids, *Journal of Physical and Chemical Reference Data* **2**(2), 313 – 409 (1973).
20. *Optical Materials for Infrared Technology*, Ed. by A. A. Askochensky (Moscow: Nauka, 1965), 335 p.

21. *Tables of Physical Quantities*, Ed. By I.K.Kikoin (Moscow: Atomizdat, 1976), 1008 p.
22. R.P.Lowndes, Dielectric Response of the Alkaline Earth Fluorides, *Journal of Physics C: Solid State Physics* 2(9), 1595 – 1605 (1969).
23. G.I.Skanavi, Physics of Dielectrics (The Range of Weak Fields) (Moscow: Gostekhizdat, 1949), 500 p.
24. H.Schweppe, Electromechanical Properties of Bismuth Germanate $Bi_4(GeO_4)_3$, *IEEE Transactions on Sonics and Ultrasonics SU-16*, 4, 219 (1969).
25. B.N.Litvin, Yu.V.Shaldin, and I.E.Pitovranova, Synthesis and Electrooptical Properties of Single Crystals of Si-Sillenite, *Crystallography Reports* **13**(5), 1106 – 1108 (1968).
26. *Physical Properties of Diamond, Reference Book,* Ed.by N.V.Novikov (Kyiv: Naukova Dumka, 1987), 188 p.
27. W.S.Brower Jr., P.H.Fang, Dielectric Constants of Scheelite Structure Crystals, *J. Applied Physics* 40(12), 4988 – 4989 (1969).
28. E.Burstein, A.Pinczuk, and R.F.Wallis, Lattice Dynamical Properties of Narrow-Gap Semiconductors, *The Physics of Semimetals and Narrow-Gap Semiconductors: Proceedings of the Conference,* Dallas, 20 – 21 mar. 1970 yr. / ed.: D. L. Carter, R. T. Bate (New York: Pergamon Press, 1971), pp. 251 – 272.
29. D.Berlincourt, H.Jaffe, and L.R.Shiozawa, Electroelastic Properties of the Sulfides, Selenides, and Tellurides of Zinc and Cadmium, *Physical Review* **129**(3), 1009 – 10107 (1963).
30. J.Baars, F.Sorger, Reststrahlen Spectra of *HgTe* and $Cd_xHg_{1-x}Te$, *Solid State Communications* **10**(9), 875–878 (1972).
31. *Physico-Chemical properties of Oxides. Handbook.* Ed. By G.V.Samsonov (Moscow: Metallurgiya, 1978), 472 p.
32. *Handbook of Chemistry and Physics* / ed.: D. R. Lide. 90th ed. New York: CRC Press LLC, 2010. 2758 p.
33. J.D.Axe, G.D. Pettit, Lattice Spectrum and Dielectric Properties of EuF_2, *J. Physics and Chemistry of Solids* **27**(4), 621 – 624 (1966).
34. A.S.Barker Jr., M. Ilegems, Infrared Lattice Vibrations and Free-Electron Dispersion in *GaN*, *Physical Review B: Condensed Matter and Materials Physics* **7**(2), 743 – 750 (1973).
35. K.Kumazaki, Dielectric Constant in $Zn_xHg_{1-x}Se$ Determined by Raman Scattering, *Physica Status Solidi B* **160**(2), K173 – K176 (1990).
36. *Handbook on Physical Properties of Semiconductors: in 3 vol. Ed.: S. Adachi (New York: Kluwer Academic Publishers, 2004), Vol. 3: II–VI Compound Semiconductors*, 472 p.
37. M.Alzamil, Study of Static Dielectric Constant of *n*-type *InAs*, *Research Journal of Applied Sciences, Engineering and Technology* **5**(2), 481 – 484 (2013).
38. S.Nanamatsu, K.Doi, and M.Takahashi, Piezoelectric, Elastic and Dielectric Properties of $LiGaO_2$, *Japanese J. of Applied Physics* 11(6), 816 – 822 (1972).
39. B.A.Scott, K.A.Ingebrigtsen, and C.C.Tseng, Crystal Growth and Properties of Pyroelectric Li_2GeO_3, *Materials Research Bulletin* **5**(12), 1045 – 1049 (1970).
40. A.K.Chaudhury, K.V.Rao, Dielectric Properties of Single Crystals of *MnO* and of Mixed Crystals of *MnO*/*CoO* and *MnO*/*NiO*, *Physica Status Solidi* **32**(2), 731 – 739 (1969).
41. S.M.Sharif, Study of Elastic Properties of Ammonium Iodide (NH_4I) with *NaCl* Structure, *SUST Studies* **14**(2), 76 – 83 (2011).
42. W.P.Mason, Elastic, Piezoelectric, and Dielectric Properties of Sodium Chlorate and Sodium Bromate, *Physical Review* **70**(7/8), 529 – 537 (1946).

43. V.Di Giura, G.Spinolo, Measurement of the Low-Frequency Dielectric Constant in Some Alkali Halides, *Il Nuovo Cimento B* **56**(1), 192 – 194 (1968).
44. V.M.Yezuchevskaya, Ya.K.Syrkin, and E.N.Deichman, Dielectric Polarization of Indium-Rubidium Sulphate Vrystalline Hydrates, *Russian J. Inorganic Chemistry*, 9(6), 1495 (1964).
45. A.G.Smagin, M.I.Yaroslavsky, *Piezoelectricity of Quartz and Crystal Oscillators* (Moscow: Energiya, 1970), 488 p.
46. A.S.Pavlovic, Some Dielectric Properties of Tantalum Pentoxide, *The J.Chemical Physics* **40**(4), 951 – 956 (1964).
47. R.K.Behera, C.S.Deo, Atomistic Models to Investigate Thorium Dioxide (ThO_2), *J. Physics: Condensed Matter* **24**(21), 215405-1 – 215405-15 (2012).
48. T.J.Isaacs, R.W.Weinert, Crystal Growth and Properties of TI_3BX_4 Crystals for Acoustic Surface-Wave and Bulk Acoustic Devices, *J. Electronic Materials* **5**(1), 13 – 22 (1976).
49. T.J.Isaacs, Tl_3VS_4 as an Acousto-Optic and Surface Wave Material, *J. Electronic Materials* **4**(1), 67 – 75 (1975).
50. G.Dolling, R.A.Cowley, and A.D.Woods, The Crystal Dynamics of Uranium Dioxide, *Canadian J. Physics* **43**(8), 1397 – 1413 (1965).
51. J.P.Hurrell, Optical Phonons of Yttrium Aluminum Garnet, *Physical Review* **173**(3), 851 – 856 (1968).
52. H.Jaffe, D.A.Berlincourt, Piezoelectric Transducer Materials, *Proceedings of the Institute of Electrical and Electronics Engineers* **53**(10), 1372 – 1386 (1965).
53. I.V.Kobyakov, V.S.Pado, Research on Electrical and Elastic Properties of Hexagonal Zinc Sulphide in the Temperature Range of 1.5-5 – 300 K, *Physics of the Solid State* **9**(8), 2173 – 2179 (1967).
54. G.A.Samara, Temperature and Pressure Dependences of the Dielectric Properties of PbF_2 and the Alkaline-Earth Fluorides, *Physical Review B: Condensed Matter and Materials Physics* **13**(10), 4529 – 4544 (1976).
55. A.S.Starkov, O.V.Pakhomov, and I.A.Starkov, Parametric Amplification of Electrocaloric Effect with a Periodic Change of Electrical Field, *Letters to J.Technical Physics* **37**(23), 125 – 131 (2011).

Submitted 16.06.2016.

P.V. Gorskiy

P.V. Gorskiy

Institute of Thermoelectricity of the NAS and MES of Ukraine,
1, Nauky Str., Chernivtsi, 58029, Ukraine

GIGANTIC THERMOEMF OF LAYERED THERMOELECTRIC MATERIALS IN A QUANTIZING MAGNETIC FIELD

In this paper, the thermoEMF of layered thermoelectric material in a strong quantizing magnetic field was calculated from unconventional standpoint, namely as a thermodynamic quantity that does not depend on the scattering mechanisms of free charge carriers in material. In this case it is defined by a linear combination of derivatives of the thermodynamic and chemical potentials with respect to temperature. Based on this representation for the case of a quantizing magnetic field perpendicular to layers, a general expression for the thermoEMF of layered material was obtained. Specific calculations show that in materials with very low effective masses of charge carriers in layer plane and very narrow conduction minibands which govern carrier motion in the perpendicular direction, the oscillation amplitude of thermoEMF even in the quasi-classical range of magnetic fields can reach 10 and more microvolts per kelvin, that can already be considered as a gigantic amplitude. Such amplitude is realized, for instance, in bismuth, though traditionally this material is not considered as layered. In the nearly-ultra-quantum fields the thermoEMF according to the results of calculations made in this paper, with a high degree of nonparabolicity can reach 30 and more millivolts per kelvin even at helium temperatures. Traditional concepts according to which the thermoEMF is a kinetic, i.e. dissipative characteristic of material, essentially regulated by the scattering mechanisms of free charge carriers, cannot explain such great values thereof, even with regard to phonon drag effect. Therefore, it must be assumed that the gigantic thermoEMF of layered thermoelectric materials in a quantizing magnetic field is their purely thermodynamic characteristic. Generation and wide application of such materials might have opened up fresh opportunities for creation of thermoelectric power converters controlled by magnetic field.

Key words: thermodynamic potential, superlattice, quantizing magnetic field, gigantic thermo-EMF, miniband.

Introduction

It is conventionally recognized that the thermoEMF of thermoelectric materials (TEM) both in the absence and presence of a magnetic field is essentially regulated by the scattering mechanisms of free charge carriers [1]. It would seem that this opinion is confirmed by many experimental data, in particular, given in [2]. It is proved by the discovery of phonon drag effect owing to which the thermoEMF can increase considerably [3]. Though [2] and [3], as well as many other earlier and more recent papers, deal with the thermoEMF in the absence of a magnetic field, it is considered that completely analogous situation takes place, at least in a quasi-classical area of quantizing magnetic fields. The theory of thermoEMF of layered thermoelectric materials with much open Fermi surfaces for this case, also with regard to phonon drag effect, was developed in [4], though this paper describes only general formulae which are "not brought to a number". At the same time, for instance, in the alloys of antimony with bismuth and arsenic [5], at helium temperatures in the quasi-classical range of

magnetic fields there were discovered gigantic oscillations of thermoEMF with the amplitude of the order of 10 μV/K that cannot be explained by phonon drag effect, but the authors of that paper attribute them to the specificity of the energy dependence of relaxation time of free carriers in a magnetic field, without specifying the details and physics of the influence of this specificity.

In contrast to traditional views, the authors of [6] propose to consider the thermoEMF in a strong quantizing magnetic field not as a kinetic coefficient, but as a purely thermodynamic, i.e. equilibrium dissipation-free quantity. They justify this proposal by the fact that the so-called "thermomagnetic current" which is determined traditionally and through which the thermoEMF in a quantizing magnetic field is expressed, does not satisfy mass-energy equation which relates coefficient of diffusion to electric conductivity [7]. Therefore, following the approach developed in [8] which takes into account the diamagnetism of free carrier gas disregarded by traditional approach they obtained the formula for the thermoEMF as a thermodynamic quantity:

$$\alpha = \frac{1}{n_0 e}\frac{\partial \Omega}{\partial T} + \frac{1}{e}\frac{\partial \zeta}{\partial T}. \qquad (1)$$

In this formula, n_0 is the concentration of free charge carriers, Ω is the thermodynamic potential of the unit volume of free carrier gas determined through large partition function, T is absolute temperature, ζ is the chemical potential of free carrier gas, the rest of notations are commonly accepted.

Then the authors of [6], probably not without reason, restricted themselves to some general manipulations of this formula from which it followed that, in fact, it is equivalent to the formula obtained in [8] which expresses the thermoEMF in a quantizing magnetic field through the entropy of the unit volume of free carrier gas, but in a more vivid form. However, the present author in monograph [9] set forth, in particular, the results of his in-depth treatment of free carrier diamagnetism in layered semiconductors. Therefore, it is not difficult for him to calculate the thermoEMF of layered thermoelectric materials in a quantizing magnetic field by formula (1) and to compare the results to those following from traditional approaches, as well as to some (rather limited!) experimental data. This is the purpose of the present paper.

General formula for the thermoEMF of layered thermoelectric material in a quantizing magnetic field

In this section, on the basis of relation (1), we shall derive a general formula for the thermoEMF of layered thermoelectric material with interlayer distance *a*, placed in a quantizing magnetic field perpendicular to layers. In so doing, we assume that motion of free carriers in plane layer is described by a parabolic dispersion law with the effective mass *m**, and in the perpendicular direction – by arbitrary dispersion law $W(ak_z)$, where k_z is corresponding component of quasi-pulse. Then charge carrier spectrum in a quantizing magnetic field with induction B perpendicular to layers is given by:

$$\varepsilon_{n,k_z} = \mu^* B(2n+1) + W(ak_z). \qquad (2)$$

In this formula, $\mu^* = \mu_B m_0 / m^*$, n is the Landau level number, the rest of notations are commonly accepted. For the layered material with such energy spectrum of free carriers from formula (1) we get the following formula for thermoEMF α:

$$\alpha = \frac{k}{e}\left(\frac{F_1}{F_2} + \frac{F_3}{F_4}\right). \tag{3}$$

The dimensionless functions F_1, F_2, F_3, F_4 which enter into formula (3) are given by:

$$F_1 = -\frac{\pi t \kappa_\gamma}{3} + \frac{b^2}{t}\sum_{l=1}^{\infty}(-1)^l\left[\frac{t}{b\,\mathrm{sh}\left(blt^{-1}\right)} + \frac{\mathrm{ch}\left(blt^{-1}\right)}{\mathrm{sh}^2\left(blt^{-1}\right)}\right]\left\{\int\limits_{w(x)\le\gamma}\exp\left[lt^{-1}\left(w(x)-\gamma\right)\right]dx - \int\limits_{w(x)\ge\gamma}\exp\left[lt^{-1}\left(\gamma-w(x)\right)\right]\right\} +$$
$$+\frac{b}{t}\sum_{l=1}^{\infty}\frac{(-1)^l}{\mathrm{sh}\left(blt^{-1}\right)}\left\{\int\limits_{w(x)\ge\gamma}\left(\gamma-w(x)\right)\exp\left[lt^{-1}\left(\gamma-w(x)\right)\right] - \int\limits_{w(x)\le\gamma}\left(w(x)-\gamma\right)\exp\left[lt^{-1}\left(w(x)-\gamma\right)\right]dx\right\} + \tag{4}$$
$$+2b\sum_{l=1}^{\infty}\frac{(-1)^l}{l}\left[\frac{1}{\mathrm{sh}\left(\pi^2 ltb^{-1}\right)} - \frac{\mathrm{ch}\left(\pi^2 ltb^{-1}\right)}{\mathrm{sh}^2\left(\pi^2 ltb^{-1}\right)}\right]\int\limits_{w(x)\le\gamma}\cos\left[\pi lb^{-1}\left(\gamma-w(x)\right)\right]dx,$$

$$F_2 = \int\limits_{w(x)\le\gamma_0}\left(\gamma_0 - w(x)\right)dx, \tag{5}$$

$$F_3 = 2\pi\sum_{l=1}^{\infty}\frac{(-1)^{l-1}}{\mathrm{sh}\left(\pi^2 ltb^{-1}\right)}\int\limits_{w(x)\le\gamma}\sin\left[\pi lb^{-1}\left(\gamma-w(x)\right)\right]dx + 2\pi^3 tb^{-1}\sum_{l=1}^{\infty}\frac{(-1)^l\,\mathrm{ch}\left(\pi^2 ltb^{-1}\right)}{\mathrm{sh}^2\left(\pi^2 ltb^{-1}\right)}\int\limits_{w(x)\le\gamma}\sin\left[\pi lb^{-1}\left(\gamma-w(x)\right)\right]dx +$$
$$-b^2t^{-2}\sum_{l=1}^{\infty}\frac{(-1)^l\,l\,\mathrm{ch}\left(blt^{-1}\right)}{\mathrm{sh}^2\left(blt^{-1}\right)}\left\{\int\limits_{w(x)\le\gamma}\exp\left[lt^{-1}\left(w(x)-\gamma\right)\right]dx + \int\limits_{w(x)\ge\gamma}\exp\left[lt^{-1}\left(\gamma-w(x)\right)\right]dx\right\} + bt^{-2}\sum_{l=1}^{\infty}\frac{(-1)^l\,l}{\mathrm{sh}\left(blt^{-1}\right)}\times \tag{6}$$
$$\times\left\{\int\limits_{w(x)\le\gamma}\left(w(x)-\gamma\right)\exp\left[lt^{-1}\left(w(x)-\gamma\right)\right]dx + \int\limits_{w(x)\ge\gamma}\left(\gamma-w(x)\right)\exp\left[lt^{-1}\left(\gamma-w(x)\right)\right]dx\right\}$$

$$F_4 = \kappa_\gamma + 2\pi^2 tb^{-1}\sum_{l=1}^{\infty}\frac{(-1)^l\,l}{\mathrm{sh}\left(\pi^2 ltb^{-1}\right)}\int\limits_{w(x)\le\gamma}\cos\left[\pi lb^{-1}\left(\gamma-w(x)\right)\right]dx + \sum_{l=1}^{\infty}\frac{(-1)^l\,blt^{-1}}{\mathrm{sh}\left(blt^{-1}\right)}\left\{\int\limits_{w(x)\ge\gamma}\exp\left[lt^{-1}\left(\gamma-w(x)\right)\right]dx - \right.$$
$$\left. - \int\limits_{w(x)\le\gamma}\exp\left[lt^{-1}\left(w(x)-\gamma\right)\right]dx\right\}. \tag{7}$$

The dimensionless parameters (complexes) and the dimensionless function for layered material described by the Fivaz model which enter into these functions have the following values:

$$t = kT/\Delta,\ b = \mu^* B/\Delta,\ \gamma = \zeta/\Delta,\ w(x) = 1-\cos x,\ \kappa_\gamma = \arccos(1-\gamma). \tag{8}$$

In such a case, Δ is the half-width of a narrow miniband which determines the motion of free carriers in the direction perpendicular to layers, ζ is the temperature- and magnetic field-dependent chemical potential of free carriers subsystem. The latter is determined from the following equation:

$$\int\limits_{w(x)\le\gamma_0}\left(\gamma_0 - w(x)\right)dx = \int\limits_{w(x)\le\gamma}\left(\gamma - w(x)\right)dx + 2\pi t\sum_{l=1}^{\infty}\frac{(-1)^l}{\mathrm{sh}\left(\pi^2 ltb^{-1}\right)}\int\limits_{w(x)\le\gamma}\sin\left[\pi lb^{-1}\left(\gamma-w(x)\right)\right]dx +$$
$$+b\sum_{l=1}^{\infty}\frac{(-1)^{l-1}}{\mathrm{sh}\left(blt^{-1}\right)}\left\{\int\limits_{w(x)\le\gamma}\exp\left[lt^{-1}\left(w(x)-\gamma\right)\right]dx + \int\limits_{w(x)\ge\gamma}\exp\left[lt^{-1}\left(\gamma-w(x)\right)\right]dx\right\}. \tag{9}$$

Here, in the case of nondegenerate gas $\kappa_\gamma = 0$, and at $\gamma = 2$ $\kappa_\gamma = \pi$.

In its turn, parameter γ_0 is related to free carrier concentration by the following relation:

$$n_0 a h^2 / 4\pi m^* \Delta = (\gamma_0 - 1)\arccos(1-\gamma_0) + \sqrt{2\gamma_0 - \gamma_0^2}\,. \tag{10}$$

Formulae (3) – (7) with regard to (8) – (10) completely determine the thermoEMF of layered thermoelectric material as a purely thermodynamic quantity. It should be noted that, on the one hand, the authors of [6] who proposed formula (1) did not indicate the exact values of magnetic field induction starting from which this formula, hence all the relations obtained on its basis in this paper, become valid. On the other hand, electron gas diamagnetism also exists in weak magnetic fields, including in the zero magnetic field limit. Therefore, it is worthwhile to consider and compare to known theoretical results and experiment the corollaries of formula (1), hence, of formulae (3) – (7) in the zero magnetic field limit. In this limit the relation (5) is not changed, and the relations (4), (6) and (7) acquire the form:

$$F_1(0) = -\frac{\pi t \kappa_\gamma}{3} + t\sum_{l=1}^{\infty}(-1)^l\left(\frac{1}{l}+\frac{1}{l^2}\right)\left\{\int\limits_{w(x)\le\gamma}\exp\left[lt^{-1}\left(w(x)-\gamma\right)\right]dx - \int\limits_{w(x)\ge\gamma}\exp\left[lt^{-1}\left(\gamma-w(x)\right)\right]\right\} + \\ +\sum_{l=1}^{\infty}\frac{(-1)^l}{l}\left\{\int\limits_{w(x)\ge\gamma}\left(\gamma-w(x)\right)\exp\left[lt^{-1}\left(\gamma-w(x)\right)\right] - \int\limits_{w(x)\le\gamma}\left(w(x)-\gamma\right)\exp\left[lt^{-1}\left(w(x)-\gamma\right)\right]dx\right\}, \tag{11}$$

$$F_3(0) = -\sum_{l=1}^{\infty}\frac{(-1)^l}{l}\left\{\int\limits_{w(x)\le\gamma}\exp\left[lt^{-1}\left(w(x)-\gamma\right)\right]dx + \int\limits_{w(x)\ge\gamma}\exp\left[lt^{-1}\left(\gamma-w(x)\right)\right]dx\right\} + t^{-1}\sum_{.l=1}^{\infty}(-1)^l \times \\ \times\left\{\int\limits_{w(x)\le\gamma}\left(w(x)-\gamma\right)\exp\left[lt^{-1}\left(w(x)-\gamma\right)\right]dx + \int\limits_{w(x)\ge\gamma}\left(\gamma-w(x)\right)\exp\left[lt^{-1}\left(\gamma-w(x)\right)\right]dx\right\}, \tag{12}$$

$$F_4(0) = \kappa_\gamma + \sum_{l=1}^{\infty}(-1)^l\left\{\int\limits_{w(x)\ge\gamma}\exp\left[lt^{-1}\left(\gamma-w(x)\right)\right]dx - \int\limits_{w(x)\le\gamma}\exp\left[lt^{-1}\left(w(x)-\gamma\right)\right]dx\right\}. \tag{13}$$

The equation which determines the chemical potential takes on the form:

$$\int\limits_{w(x)\le\gamma_0}\left(\gamma_0 - w(x)\right)dx = t\int_0^{\pi}\ln\left\{1+\exp\left[\frac{\gamma-w(x)}{t}\right]\right\}dx\,. \tag{13}$$

ThermoEMF of layered thermoelectric material in a weak magnetic field

The results of calculation of thermoEMF of layered thermoelectric material in a weak magnetic field are given in Fig. 1.

From the figure it is seen that, at least at relatively low values of γ_0, the thermoEMF of layered thermoelectric material first increases with a rise in temperature to sufficiently high values of several mV/K, then drastically changes its polarity, reaching 7 – 11 mV/K, following which it starts decaying. Such a situation is due to a purely thermodynamic nature of the thermoEMF in the case under study. From formula (1) it follows that the thermoEMF is governed by two competing processes.

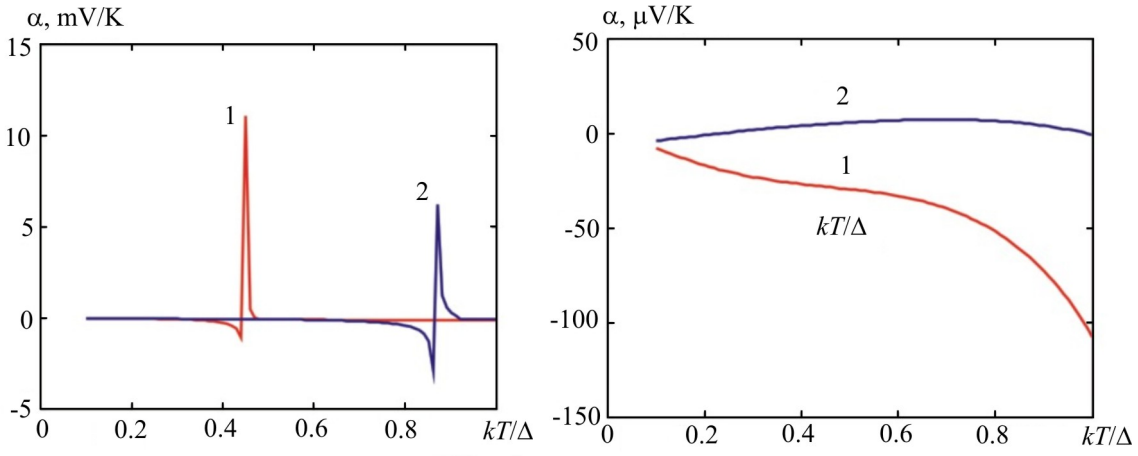

a) *b*)

Fig. 1. Temperature dependences of the thermoEMF of layered thermoelectric material in a weak magnetic field. In Fig. 1 a curves 1, 2 correspond to the values of γ_0 equal to 0.5 and 1, and in Fig. 1 b – 1.5 and 2.

On the one hand, with a rise in temperature, there is increase in the thermodynamic potential, which contributes to increase in the value of thermoEMF. On the other hand, with a rise in temperature, the chemical potential (at least in impurity material) decreases, which contributes to decrease in the value of thermoEMF. This is precisely why the temperature dependence of thermoEMF is such as above. For the foregoing reasons, a similar behaviour of thermoEMF must also take place at higher values of γ_0, i.e. free carrier concentrations. However, the higher these concentrations, the slower, all other factors being equal, the thermodynamic and chemical potentials vary with temperature. Consequently, the value of thermoEMF, all other factors being equal, with increase in free carrier concentration must decay, and its maximum must shift towards higher temperatures. Exactly for this reason in the analyzed temperature range at concentrations corresponding to values of γ_0 equal to 1.5 and 2 the maximum values of thermoEMF do not become apparent. Note that with traditional consideration, the thermoEMF of impurity material, with a rise in temperature, all the time while we are in the impurity region, is generally increased, because in terms of traditional assumptions a reduction in the chemical potential should contribute to thermoEMF increase.

Nevertheless, let us make a more detailed comparison between the obtained results and the experimental data. Let us consider, for instance, materials based on bismuth telluride. According to [1] and our estimates given, e.g. in [10], for these materials it can be assumed that $\Delta = 1.2$ eV, $m^* = m_0$, $n_0 = 3 \cdot 10^{19}\,\text{cm}^{-3}$, $a = 3$ nm. We obtain that at 300 K for *n*-type material the Seebeck coefficient must have been equal to – 1.95 μV/K. However, the true value of thermoEMF of this material under said conditions is two orders of magnitude higher. Therefore, we come to conclusion that in the zero magnetic field and at normal temperatures the above mechanism, at least for traditional thermoelectric materials, does not work. Although from the plot in Fig. 1 *a* it follows that in the zero magnetic field this mechanism might have been "activated" at higher temperatures, in traditional thermoelectric materials it will not be the case, since for them the respective "activation temperature" is higher than melting temperature.

Moreover, an essential fault of using this approach in the absence of a magnetic field is impossibility to explain the thermoEMF anisotropy which is found in many layered materials [11], as long as "purely thermodynamic" thermoEMF according to general formula (1) must be a scalar, rather than a tensor quantity.

However, a different situation can be realized in materials with narrow allowed energy bands. If, for instance, $\Delta = 0.06$ eV, the above effect might have become apparent already at temperature 278 K or at higher carrier concentration at temperature 556 K. Instead, this does not take place either because the dissipation-free thermoEMF in the weak field limit exists only formally, without being such in reality, or because carrier concentration in these materials is too high to achieve the temperature which is needed for "activation" of the effect.

Gigantic thermoEMF of layered thermoelectric material in a quantizing magnetic field

To determine the thermoEMF in a quantizing magnetic field at low temperatures, we leave in formulae (4), (6) and (7), as well as in equation (9) only the terms which do not explicitly depend on the magnetic field and oscillating functions of the magnetic field. The field dependences of thermoEMF for this case in quasi-classical magnetic fields are given in Fig. 2, and in a wider range of magnetic fields, including ultra-quantum ones, in Fig. 3.

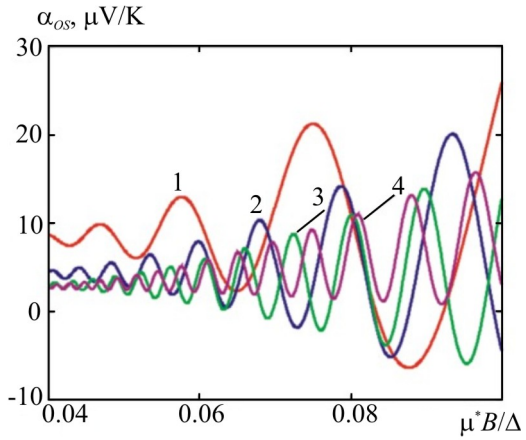

Fig. 2. Field dependences of the thermoEMF at $kT/\Delta = 0.03$ in a quasi-classical range of magnetic fields. Curves 1 – 4 are for the values of γ_0 from 0.5 to 2 with increment 0.5.

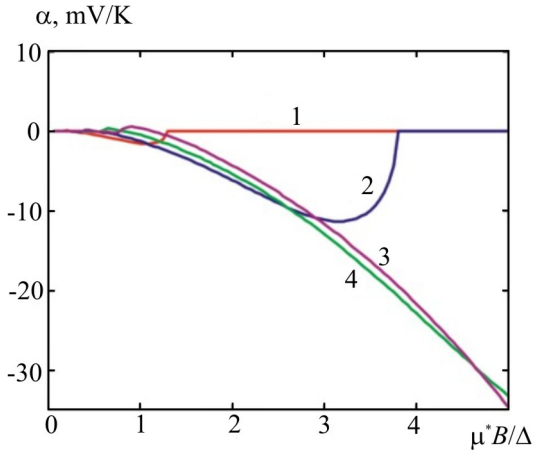

Fig. 3. Field dependences of the thermoEMF at $kT/\Delta = 0.03$ in a wide range of magnetic fields. Curves 1 – 4 are for the values of γ_0 from 0.5 to 2 with increment 0.5.

From the figures it is seen that even in the quasi-classical range of magnetic fields the oscillation amplitude of thermoEMF for the analyzed range of carrier concentrations reaches 6 – 15 μV/K. Such amplitude according to [5] can be considered as gigantic. With increasing carrier

concentration, the oscillation frequency of thermoEMF grows, and the amplitude drops. It is noteworthy that in [5], materials whose thermoEMF oscillations were studied experimentally are not considered as layered. However, our approach here is applicable to them, at least when a dominant role is played by the so-called "small groups" of free charge carriers. From the results presented in [5] it follows that thermoEMF oscillations in the investigated semi-metallic alloys of antimony with arsenic can also be of a purely thermodynamic nature.

In the nearly ultra-quantum fields the thermoEMF first reaches rather high maximum, and then decays due to compression of the Fermi surface in the direction of a magnetic field because of free carrier condensation in the lower Landau subband. However, the stronger the magnetic field, the more difficult it is to compress the Fermi surface, by virtue of which with increasing concentration of free carriers, the thermoEMF maximum is drastically increased and shifted towards the area of stronger magnetic fields. Therefore, at high concentrations in the considered range of magnetic fields this maximum does not become apparent, and thermoEMF even at low temperatures achieves rather high values, namely of the order of 35 mV/K.

Let us now analyze the possibility of reaching the effect of drastic thermoEMF increase in a quantizing magnetic field. In traditional materials based on superlattices of *Al-Ga-As* system for which $\Delta = 0.06\,\text{eV}$, $m^* = 0.5\,m_0$ reaching said effect requires magnetic fields with inductions of the order of 2600 *T* which are hardly achievable. However, for drastically anisotropic superlattices, for instance, based on graphene for which $\Delta = 0.01\,\text{eV}$, $m^* = 10^{-3} m_0$ it is sufficient to have fields with inductions of the order of 0.86 *T* which are quite common today. Therefore, such materials that are "controlled" by a quantizing magnetic field can be used as cooling materials for very low temperatures.

ThermoEMF of layered thermoelectric material in a quantizing magnetic field at high temperatures

To pass over to the case of high temperatures, we ignore the oscillating terms in formulae (4), (6) and (7) equation (9). Then, as a result of calculations we get the field dependences of thermoEMF shown in Fig. 4.

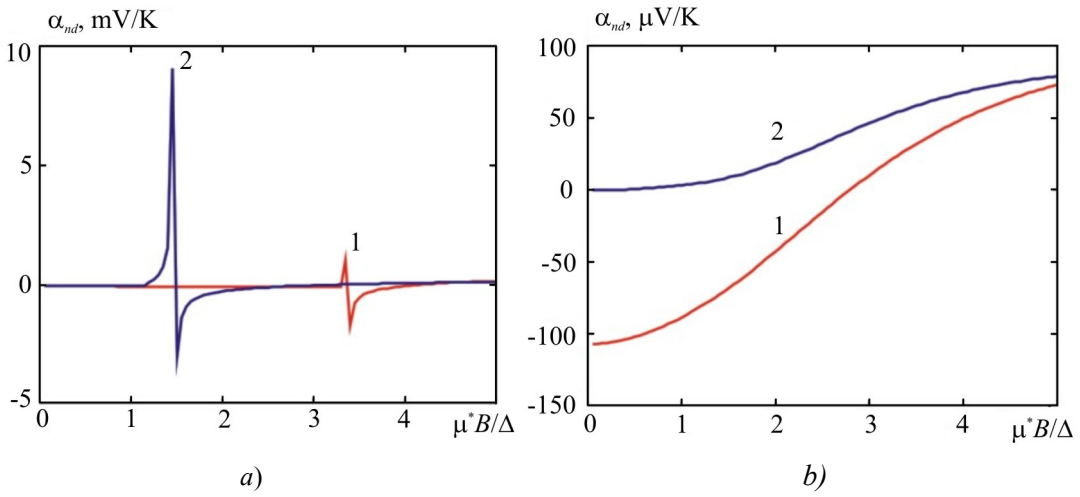

Fig. 4. Field dependences of the thermoEMF of layered thermoelectric material at high temperature ($kT/\Delta = 1$) in a wide range of magnetic fields. In Fig. 4 a curves 1, 2 correspond to the values of γ_0 equal to 0.5 and 1 a in Fig. 4 b to 1.5 and 2.

From Fig. 4 *a* it is seen that there is an optimal carrier concentration whereby the effect of drastic thermoEMF increase in a magnetic field manifests itself in the best way. It is explained by the following physical reasons. On the one hand, magnetic field increase from thermodynamic standpoint is equivalent to material cooling. An as long as the curves in Fig. 4 *a*, *b* are constructed with the highest value of parameter $kT/\Delta = 1$ from the considered range, it is clear that with magnetic field increase the thermoEMF peak must take place at least for those carrier concentrations whereby it occurs in the range of $0 \le kT/\Delta \le 1$ (within the approach used) in the absence of a magnetic field. At different carrier concentrations in the same temperature range this peak must not be observed. On the other hand, at high temperatures the chemical potential of carriers with a rise in temperature monotonously decreases, and with magnetic field increase, on the contrary, monotonously increases. So, both the possibility itself of thermoEMF peak origination in a quantizing magnetic field and its value are governed by the ratio between the velocities of these competing processes. With low carrier concentrations these processes proceed equally fast, and with high concentrations − equally slow. Therefore, at high temperature there is optimal carrier concentration, hence the degree of material nonparabolicity when the difference in velocities of these processes is the greatest, hence the thermoEMF peak is most pronounced. The same reasons account for the reversal of thermoEMF polarity in a quantizing magnetic field. Thus, control of the figure of merit of generator materials with the aid of a quantizing magnetic field is also possible, if the effective masses of carriers in layer plane are sufficiently small. At the same time, miniband widths must be optimal in the sense that the temperature whereby thermoEMF peak takes place must be sufficiently high so that the material could be considered to be "generator" and at the same time the approach used here would be valid. According to Fig. 4 *a*, in the considered range of carrier concentrations the peak thermoEMF values change approximately in the range of (1 ÷ 9) mV/K, hence, they can be also considered to be gigantic.

Conclusions

1. Based on the idea of thermoEMF in a quantizing magnetic field as a purely thermodynamic quantity, it was shown that both at low and high temperatures the value of thermoEMF of layered thermoelectric materials in the presence of this field can reach 1 – 35 mV/K.
2. At low temperatures the value of thermoEMF in a quantizing magnetic field close to ultra-quantum limit with growing concentration of free carriers is increased. Whereas at high concentrations there is optimal carrier concentration whereby the peak of thermoEMF is expressed in the best way.
3. The thermoEMF, hence the figure of merit of layered cooling and generator thermoelectric materials can be efficiently controlled with the aid of a quantizing magnetic field, provided that the effective masses of charge carriers in layer plane are sufficiently low, and carrier concentrations and miniband widths which determine carrier motion in the direction perpendicular to layers have optimal values.

The author would like to express his gratitude to academician L.I. Anatychuk for the approval of research subject, as well as to chief researcher L.N. Vikhor for the helpful and constructive discussion of the work results.

References

1. B.M.Goltsman, V.A.Kudinov, and I.A.Smirnov, *Semiconductor Thermoelectric Materials Based on Bi_2Te_3* (Moscow: Nauka, 1972), 320p.

2. L.D.Ivanova, Yu.V.Granatkina, A.Dausher, et al., Influence of Purity and Perfection of Czochralski-growth Single Crystals of Bismuth and Antimony Chalcogenides Solid Solution on Their Thermoelectric Properties, *Proc. of 5th European Workshop on Thermoelectrics* (Pardubice, Czech Republic, 1999), P.175 – 178.
3. I.G.Kuleyev, Electron-Phonon Drag, Thermoelectric Effects and Thermal Conductivity of Degenerate Semiconductors, *Physics of the Solid State* **41**(10), 1753 – 1762 (1999).
4. O.V.Kirichenko, D.Krstovska, and V.G.Peschanskiy, Thermoelectric Effects in Layered Conductors in a Strong Magnetic Field, *JETF* **126,** issue 1(7), 246 – 252 (2004).
5. F.M.Muntyanu, K.M.Pyrtsak, and A.Gulevskyi, Gigantic Quantum Oscillations of Magneto-
6. thermoEMF in Semimetallic Alloys of *Sb* with *Bi* and *As*, *Physics of the Solid State* **43**(2), 207 – 209 (2001).
7. B.M.Askerov, M.M.Makhmudov, and H.A.Gasanov, Equation of State and Theory of ThermoEMF in a Quantizing Magnetic Field, *Semiconductors* **32**(3), 290 – 291 (1998).
8. E.M.Lifshits, L.P.Pitayevskiy, *Physical Kinetics* (Moscow: Nauka, 1979), 528p.
9. Yu.N.Obraztsov, ThermoEMF of Semiconductors in a Quantizing Magnetic Field, *Physics of the Solid State* **7**(2), 573 – 581 (1965).
10. P.V. Gorskyi, *Layered Structure Effects as Realisation of Anisotropy in Magnetic, Galvanomagnetic and Thermoelectric Phenomena* (New York: Nova Publishers, 2014, xiv), 352p.
11. P.V.Gorskiy, On the Conditions of High Figure of Merit and Methods of Search Promising Superlattice Thermoelectric Materials, *J.Thermoelectricity* 3, 5 – 12 (2015).
12. M.K.Zhitinskaya, S.A.Nemov, L.E.Shelimova, et al., ThermoEMF Anisotropy of Layered Compound $PbSb_2Te_4$, *Semiconductors* **50**(1), 8 – 10 (2008).

Submitted 27.05.2016.

V.A. Romaka[1,2], P.-F. Rogl[3], L.P. Romaka[4], V.Ya. Krayovskyy[2], Yu.V. Stadnyk[4], D. Kaczorowski[5], A.M. Horyn[4]

[1]Ya. Pidstryhach Institute for Applied Problems of Mechanics and Mathematics, the National Academy of Sciences of Ukraine, 3-b, Naukova Str., Lviv, 79060, Ukraine;
[2]National University "Lvivska Politechnika", 12, S. Bandera Str., Lviv, 79013, Ukraine;
[3]Universität Wien, 42, Währinger Str., Wien, A-1090, Österreich;
[4]Ivan Franko National University of Lviv, 6, Kyryla and Mefodiya Str., Lviv, 79005, Ukraine;
[5]W. Trzebiatowski Institute of Low Temperature and Structure Research, Polish Academy of Sciences, 2, Okolna Str., Wroclaw, 50-422, Poland

FEATURES OF STRUCTURAL, ENERGY AND KINETIC CHARACTERISTICS OF $TiNiSn_{1-x}Ga_x$ THERMOELECTRIC MATERIAL

The crystal and electronic structures, the temperature and concentration dependences of resistivity and the Seebeck coefficient of $TiNiSn_{1-x}Ga_x$ were investigated in the range of T = 80 – 400 K, x = 0.02 – 0.15. It was shown that doping of n-TiNiSn with Ga impurity atoms led to the generation in the crystal of acceptor structural defects at occupation by Ga atoms of 4b sites of Sn atoms, and donor defects as vacancies in the Sn atomic sites. The mechanism of conductivity of $TiNiSn_{1-x}Ga_x$ thermoelectric material was established.

Key words: electronic structure, resistivity, thermo-power coefficient.

Introduction

One of the methods for producing thermoelectric materials with high efficiency of thermal into electric energy conversion is generation in the crystal of donor and or acceptor structural defects, which under certain conditions changes the Seebeck coefficient and electric resistivity values [1].

Research on *n-TiNiSn* based thermoelectric materials prepared by substitution of *Sn* atoms has shown a complicated mechanism of impurity introduction into semiconductor structure. Thus, in the case of substitution of *Sn* ($5s^25p^2$) atoms by *In* ($5s^25p^1$) in $TiNiSn_{1-x}In_x$ crystal there is simultaneous generation of both acceptor (*In* atom has less *p*-electrons than *Sn* atom) and donor structural defects through generation of vacancies in the crystallographic position 4*b* of *Sn* atoms [2]. In so doing, the Fermi level ε_F remained near the conduction band, as evidenced by the negative values of the Seebeck coefficient. The absence of change in the Seebeck coefficient sign from negative to positive also took place in the case of $TiNiSn_{1-x}Al_x$ [3], where the generation of acceptors was expected, since *Al* ($3s^23p^1$), just as In, possesses less *p*-electrons as compared to *Sn*.

The paper presents the results of research on the effect of *Ga* ($4s^24p^1$) doping impurity on the change in crystalline structure, distribution of the density of electronic states (DOS), electrokinetic and energy characteristics of $TiNiSn_{1-x}Ga_x$, which will make it possible to reveal the features of electric conductivity mechanism and develop ways for optimization of material parameters for getting maximum values of thermoelectric figure of merit [4].

Investigation procedures

The $TiNiSn_{1-x}Ga_x$ samples were synthesized in the laboratory of Institute for Physical Chemistry, Vienna University. The X-ray structural analysis (powder method) was used to obtain the data arrays (diffractometer Guinier-Huber image plate system, $CuK\alpha_1$), and Fullprof program [5] was employed for the calculation of structural characteristics. The chemical and phase compositions of the samples were controlled by microprobe analyzer (EPMA, energy-dispersive X-ray analyzer). The electronic structure calculations were performed by the Korringa-Kohn-Rostoker (KKR) method in coherent potential approximation (CPA) and local density approximation (LDA) [6] with the use of Moruzzi-Janak-Williams exchange-correlation potential [7]. The accuracy of calculating the position of the Fermi level ε_F is ± 8 meV. The temperature and concentration dependences of the electrical resistivity (ρ) and the Seebeck coefficient (α) were measured with respect to copper in the temperature range $T = 80 \div 400$ K, in the samples of $TiNiSn_{1-x}Ga_x$, $x = 0.01 \div 0.10$ ($N_A^{Ga} \approx 1.9 \cdot 10^{20}$ cm^{-3} ÷ $2.9 \cdot 10^{21}$ cm^{-3}).

Research on the crystalline structure of $TiNiSn_{1-x}Ga_x$

A microprobe analysis of the concentration of atoms on the surface of $TiNiSn_{1-x}Ga_x$ samples has shown their conformity to the initial charge compositions, and X-ray phase and structural analyses have revealed no traces of other phases on X-ray diffraction patterns. As long as the atomic radius of *Ga* ($r_{Ga} = 0.141$ nm) is smaller than that of *Sn* ($r_{Sn} = 0.162$ nm), the monotonous decrease in the values of unit cell period $a(x)$ of $TiNiSn_{1-x}Ga_x$ served one of the arguments in favour of substitution of *Sn* atoms by *Ga* atoms (Fig. 1, curve 1).

Refinement of $TiNiSn_{1-x}Ga_x$ crystalline structure by the powder method has confirmed the result of [8] as regards crystal structure disorder of *n-TiNiSn* ($x = 0$), the key point of which lies in a partial, up to ~ 1 %, occupancy by *Ni* atoms of the crystallographic position 4*a* of *Ti* atoms, and the semiconductor formula can be written as $(Ti_{1-z}Ni_z)NiSn$, $z \leq 0.01$. If it is remembered that *Ni* ($3d^8 4s^2$) atom possesses a larger number of *d*-electrons than *Ti* ($3d^2 4s^2$) atom, donor structural defects are created in the crystal ("a priori" doping with donors [8]), and electrons are the majority carriers.

Structural investigations have also shown that introduction of *Ga* atoms puts into order crystalline structure of $TiNiSn_{1-x}Ga_x$ ("heals" structural defects): *Ni* atoms leave the position of *Ti* (4 *a*) atoms. Moreover, structural changes contribute to the redistribution of the electronic density of states. Thus, if donor structural defects exist in *n-TiNiSn* as a result of displacement of up to ~ 1 % of *Ti* atoms by *Ni* atoms [8], then ordering of $TiNiSn_{1-x}Ga_x$ structure is accompanied, on the one hand, by the reduction in the number of donors – *Ni* leaves the position of *Ti*.

On the other hand, as long as *Ga* atom has one *p*-electron less than *Sn* atom, the acceptor structural defects are generated in the crystal. In this case, doping of *n-TiNiSn* semiconductor of electron with the lowest concentrations of the acceptor impurity will increase the compensation ratio (the ratio between donors and acceptors) [1, 9]. At concentrations when *Ni* atoms leave position 4 *a* of *Ti* atoms, the concentration of acceptors in the crystal will increase, the type of majority carriers must change and the compensation ratio will decrease. It is important to note that ordering of $TiNiSn_{1-x}Ga_x$ structure makes it stable, and the kinetic characteristics become reproducible during thermal cycling.

At the same time, contrary to expectations, simulation of change in the values of unit cell period $a(x)$ of $TiNiSn_{1-x}Ga_x$ in case of occupation by *Ga* atoms of crystallographic position 4 *b* of *Sn* atoms a decrease in the values of $a(x)$ takes place faster (Fig. 1, curve 2) than the experiment gives (Fig. 1, curve 1).

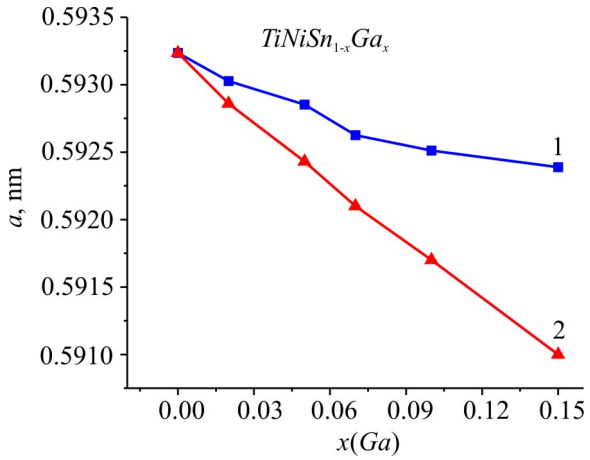

Fig. 1. Change in the values of unit cell period of $TiNiSn_{1-x}Ga_x$: 1 – experiment, 2 – calculation.

On the basis of the obtained it can be assumed that changes that took place in the structure of $TiNiSn_{1-x}Ga_x$ cannot be identified by X-ray investigation methods, however, they contribute to redistribution of the electronic density of states and, as a result, of crystal properties.

Research on the electronic structure of $TiNiSn_{1-x}Ga_x$

The density of electronic states (DOS) was calculated for simulation of electric conductivity mechanisms, the behaviour of the Fermi level ε_F, the energy gap ε_g of $TiNiSn_{1-x}Ga_x$. As long as doping of *n-TiNiSn* with *Ga* atoms puts into order crystalline structure, calculation of DOS was performed for the case of ordered structure version (Fig. 2). From Fig. 2 it is seen that on introduction into *n-TiNiSn* of *Ga* acceptor impurity, the Fermi level ε_F starts drifting from the bottom of the conduction band ε_C, spaced ~ 16.9 meV from it [8], toward the valence band ε_V, to cross it at $x \approx 0.04$.

The drift of the Fermi level ε_F from the conduction band edge ε_C to the valence band ε_V also means a change in the ratio of $TiNiSn_{1-x}Ga_x$ majority carriers. Thus, for the concentrations of $TiNiSn_{1-x}Ga_x$, $x < 0.02$, when the Fermi level ε_F is between the conduction band ε_C and the midgap ε_g, electrons are the majority carriers. In this case, doping of *n-TiNiSn* semiconductor of electron conductivity type with the lowest concentrations of acceptors will be accompanied by increase in the compensation ratio [1, 9]. In turn, at $x > 0.02$ and up to crossing of the valence band ε_V by the Fermi level ε_F holes are the majority carriers. In this case, doping of *p*-type semiconductor with acceptors must lead to a reduction of compensation ratio. Besides, crossing of the valence band by the Fermi level ε_F will also cause a change from the activation to metal conduction mechanism of $TiNiSn_{1-x}Ga_x$ (the dielectric-metal transition which is referred to as the Anderson transition [9]).

Calculation of the electronic density of states for $TiNiSn_{1-x}Ga_x$ allows predicting its kinetic characteristics, in particular, the behaviour of the Seebeck coefficient $\alpha(x,T)$ at different temperatures (Fig. 3). Below is given the working formula used for the calculation of $\alpha(x,T)$ [9]:

$$\alpha(x,T) = \frac{2\pi^2}{3}\frac{k_B^2 T}{e}\left(\frac{d}{d\varepsilon}\ln g(\varepsilon_F)\right),$$

where $g(\varepsilon_F)$ is the density of states at the Fermi level.

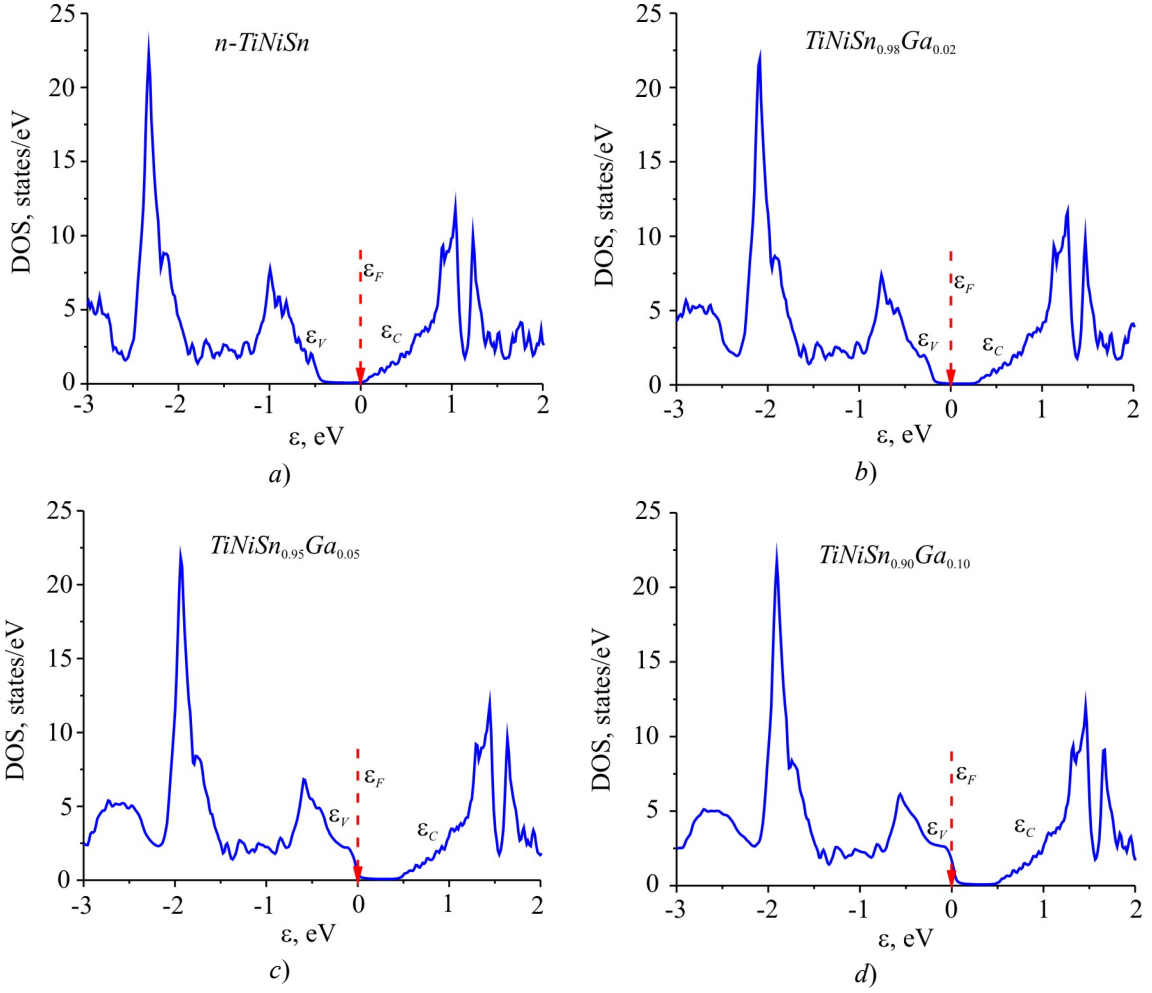

Fig. 2. Calculation of the electronic density of states for $TiNiSn_{1-x}Ga_x$.

From Fig. 3 it is seen that at different concentrations of *Ga* one can obtain in thermoelectric material high values of the Seebeck coefficient of both signs, assuring high values of thermoelectric figure of merit [4].

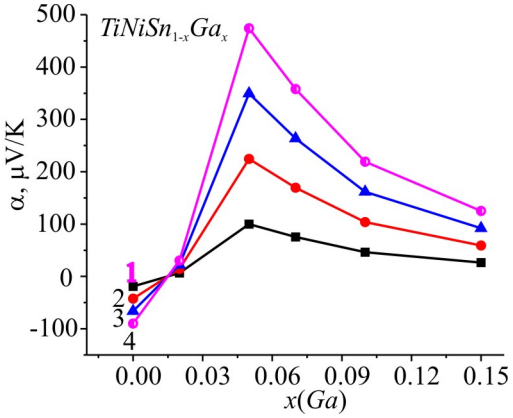

Fig. 3. Changes in the values of the Seebeck coefficient of $TiNiSn_{1-x}Ga_x$ at the temperatures: 1 – 80 K; 2 – 180 K; 3 – 280 K; 4 – 380 K.

Thus, the results of calculation of the electronic density of states for $TiNiSn_{1-x}Ga_x$, based on structural research data, prove the acceptor nature of generated defects. The results of research on the kinetic characteristics of $TiNiSn_{1-x}Ga_x$ will show the degree of conformity of such calculations to real processes occurring in material.

Research on the electrokinetic and energy characteristics of $TiNiSn_{1-x}Ga_x$

The temperature dependences of resistivity $\ln\rho(1/T)$ and the Seebeck coefficient $\alpha(1/T)$ for $TiNiSn_{1-x}Ga_x$ are presented in Fig. 4. From the high-temperature activation areas of $\ln\rho(1/T)$ dependences the activation energy from the Fermi level ε_F to the bands of continuous energies ε_1^{ρ} was calculated, and from the same $\alpha(1/T)$ dependences – the activation energies ε_1^{α} yielding the value of modulation amplitude of continuous energy bands for heavily doped compensated semiconductor [1, 9].

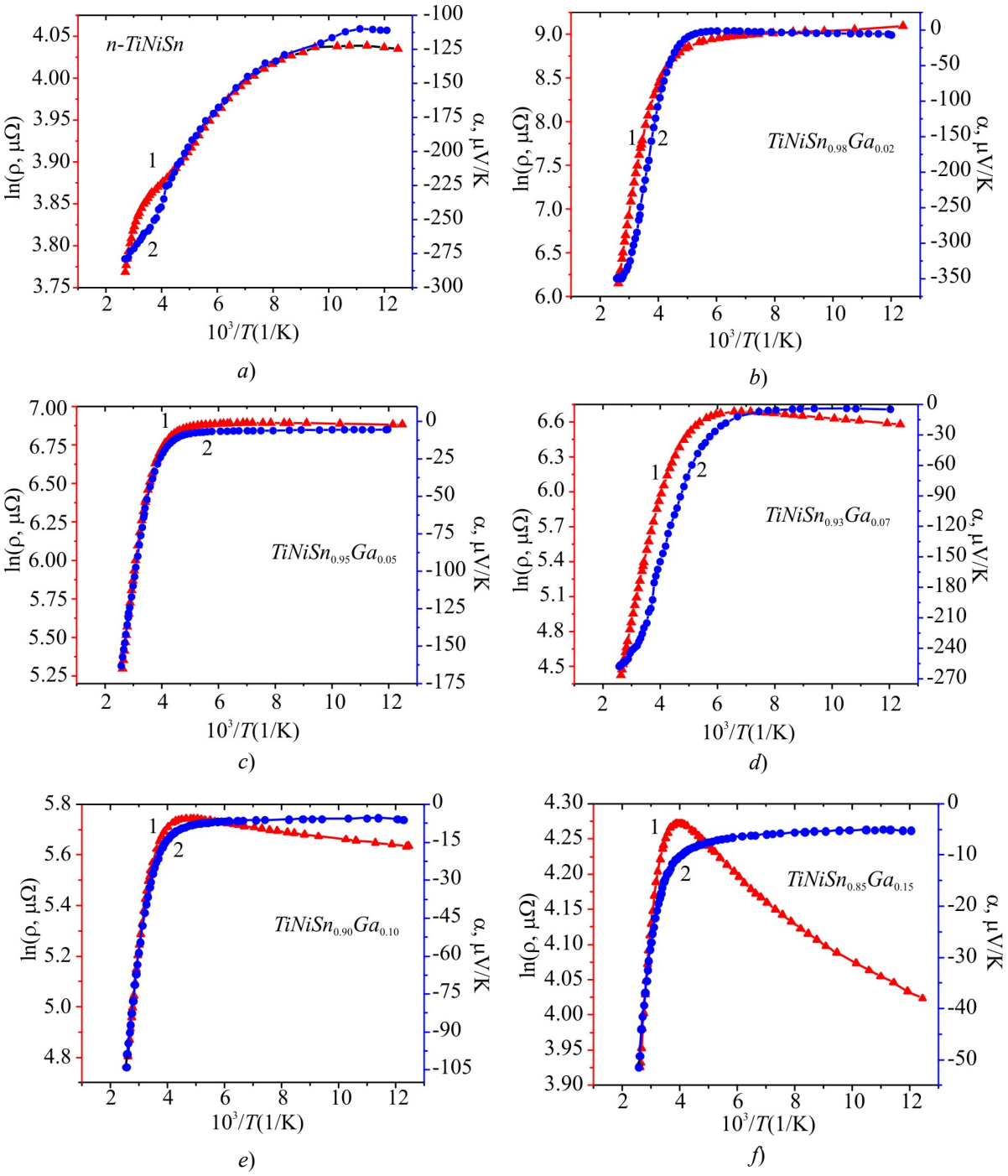

Fig. 4. Temperature dependences of the electric resistivity and the Seebeck coefficient of $TiNiSn_{1-x}Ga_x$.

As is seen from Fig. 4, for all compositions of $TiNiSn_{1-x}Ga_x$ samples on the dependences $\ln\rho(1/T)$ there are high-temperature activation areas, which points to the arrangement of the Fermi level ε_F in the energy gap, from where carriers are activated to continuous energy bands. The result obtained contradicts to the results of calculations of DOS (Fig. 2) which predicted crossing by the Fermi level ε_F of the valence band and conductivity metallization at concentration *Ga* $x \approx 0.04$.

Introduction to *n-TiNiSn* of the lowest in the experiment concentration of *Ga* atoms by substitution of *Sn* is accompanied with a drastic increase in the values of electric resistivity $\rho(x)$ (Fig. 5 *a*), for instance, at 80 K, from the values of $\rho(x = 0) = 56.5$ μΩ·m to $\rho(x = 0.02) = 8885.2$ μΩ·m. Such behaviour of $\rho(x)$ at different temperatures (Fig. 5 *a*) is a manifestation of the above described structural feature of semiconductor which accounts for a simultaneous reduction of free electrons by two mechanisms: (1) – decreasing the number of donors, when *Ni* atoms leave position 4*a* of *Ti* atoms ("healing" of donor-nature defects) and (2) – "freezing out" of free electrons to acceptor band generated at occupation by *Ga* atoms of the position of *Sn* atoms. Exactly the reduction in the concentration of free electrons *n* leads to increase in the values of electric resistivity, since $\rho \sim 1/n$.

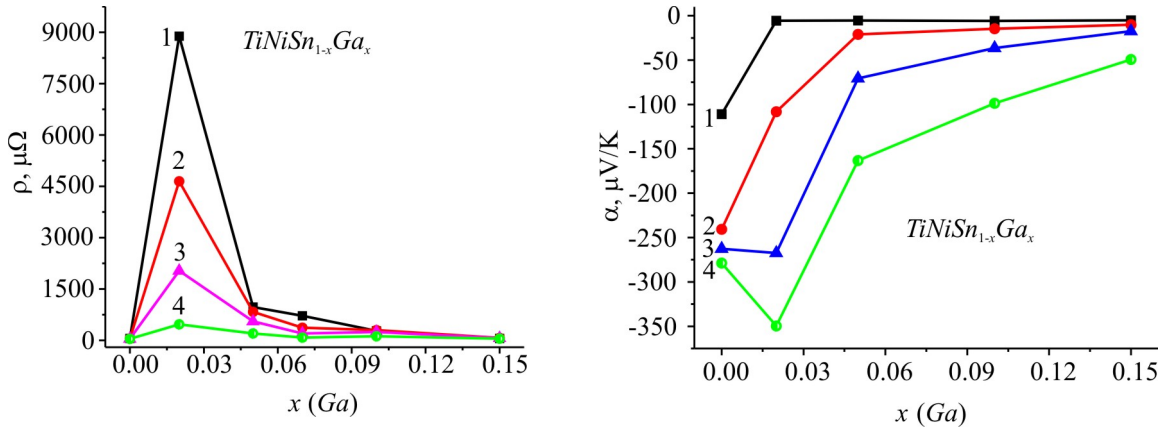

a) *b*)

Fig. 5.Change in the values of the electric resistivity ρ(x) (a) and the Seebeck coefficient α(x) (b) of $TiNiSn_{1-x}Ga_x$ at the temperatures: 1 – 80 K; 2 – 160 K; 3 – 250 K; 4 – 380 K.

The presence of an extreme point on the dependence $\rho(x, T)$ at $x = 0.02$ (Fig. 5*a*) and the reduction of electric resistivity values of $TiNiSn_{1-x}Ga_x$ at higher concentrations of *Ga* impurity atoms, for instance, at 80 K, from the values of $\rho(x = 0.05) = 975.3$ μΩ·m to $\rho(x = 0.10) = 280.1$ μΩ·m and $\rho(x = 0.15) = 55.9$ μΩ·m points to a drastic increase in the crystal of free carriers. *A priori*, based on the results of calculation of $TiNiSn_{1-x}Ga_x$ electronic structure, such free carriers must be holes which will determine the electric conductivity of thermoelectric material.

However, the behaviour of the Seebeck coefficient of $TiNiSn_{1-x}Ga_x$ $\alpha(x)$ (Fig. 4) and $\alpha(1/T)$ (Fig. 5 *b*) proved to be unexpected. Thus, the negative values of the Seebeck coefficient of *n-TiNiSn* (or, in the other form, $Ti_{1-z}Ni_z)NiSn$) are understandable and related to "a priori doping" of semiconductor with donors generated at occupation by *Ni* atoms of up to ~ 1 % ($z \approx 0.01$) of positions of *Ti* atoms [8].

In turn, in the sample of $TiNiSn_{1-x}Ga_x$, $x = 0.02$, the concentration of *Ga* acceptor impurity exceeds that of available donors ($y \approx 0.01$) in *n-TiNiSn* ("a priori" doping), and the state of strong compensation is realized when the Fermi level ε_F must be arranged a little lower than the midgap ε_g. At the same time, the negative values of the Seebeck coefficient at $x = 0.02$ testify (Fig. 4, 5 *b*) that the concentration of generated acceptors at the substitution of *Sn* atoms by *Ga* atoms is lower than the

concentration of donors, hence the Fermi level ε_F is fixed by the impurity donor band (above the midgap). It turns out that the concentration of donors ($z \approx 0.01$) in $TiNiSn_{1-x}Ga_x$, $x = 0.02$, exceeds the concentration of acceptors, though it should be the other way round. Moreover, in all the samples of $TiNiSn_{1-x}Ga_x$, $x \geq 0.02$, the values of the Seebeck coefficient remained negative and, for instance, at temperature 80 K they changed from the values of $\alpha(x = 0) = -110.9$ μV/K to $\alpha(x = 0.02) = -5.7$ μV/K anda $\alpha(x = 0.15) = -5.2$ μV/K and temperature 380 K from the values of $\alpha(x = 0.02) = -349.7$ μV/K to $\alpha(x = 0.15) = -49.3$ μV/K. The negative values of the Seebeck coefficient of $TiNiSn_{1-x}Ga_x$ for all compositions and temperatures under study indicate that electrons continue to remain the majority carriers in the crystal. Such behaviour of the Seebeck coefficient of $TiNiSn_{1-x}Ga_x$ reminds the behaviour of kinetic characteristics in the case of introduction into *n-TiNiSn* of other *p*-elements *In* and *Al* [2, 3].

This result does not correspond to the results of calculations of DOS in $TiNiSn_{1-x}Ga_x$ performed for the ordered structure version. In such a case, only acceptor defects had to be generated in the crystal. The behaviour of the Seebeck coefficient (Fig. 4, 5 *b*) shows that donor defects are also generated in $TiNiSn_{1-x}Ga_x$ by the unknown mechanism and the concentration of donors exceeds the concentration of generated acceptors.

In this context it is interesting to trace the character of change in the energy characteristics of $TiNiSn_{1-x}Ga_x$ obtained from the experimental investigations of the temperature dependences of resistivity $\ln\rho(1/T)$ and the Seebeck coefficient $\alpha(1/T)$ (Fig. 6). Taking into account that the value of the Seebeck coefficient points to electrons as the majority carriers in $TiNiSn_{1-x}Ga_x$, the high-temperature activation areas on the dependences $\ln\rho(1/T)$ and $\alpha(1/T)$ reflect a complicated process of simultaneous thermal throw of electrons from the impurity donor area to the conduction band and of holes to the valence band. In so doing, the concentration component of free electrons exceeds that for holes.

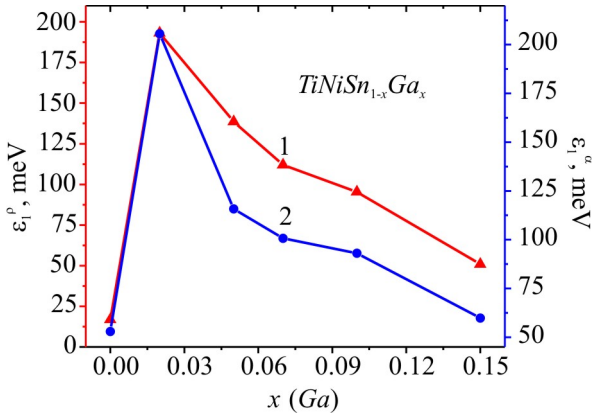

Fig. 6. Change in the values of activation energy $\varepsilon_1^{\rho}(x)$ (1) and $\varepsilon_1^{\alpha}(x)$ (2) of $TiNiSn_{1-x}Ga_x$.

A drastic increase in the values of activation energy ε_1^{ρ} from 16.9 meV for $x = 0$ to $\varepsilon_1^{\rho}(x = 0.02) = 193.2$ meV clearly shows that the Fermi level ε_F moves toward the midgap and became essentially distant from the bottom of the conduction band. Such behaviour of the Fermi level ε_F can be only caused by the appearance in $TiNiSn_{1-x}Ga_x$ crystal of acceptors that trap free electrons, reducing their concentration, which increases the compensation ratio of semiconductor (the ratio between acceptors and donors). From the linear behaviour of $\varepsilon_1^{\rho}(x)$ in the concentration area $x = 0 – 0.02$ it can be argued that the Fermi level ε_F moves from the edge of conduction band at a rate of $\Delta\varepsilon_F/\Delta x = 88.2$ meV/% *Ga*. The obtained result is logical, since the concentration of *Ga* impurity grows by the linear law, and the acceptor defects are generated in $TiNiSn_{1-x}Ga_x$ by the same law.

However, further increase in the concentration of *Ga* atoms in $TiNiSn_{1-x}Ga_x$, $x > 0.02$ leads to a decrease in the values of activation energy ε_1^{ρ} (Fig. 6), which points to a reverse motion of the

Fermi level ε_F now toward the conduction band, as long as the values of the Seebeck coefficient remain negative (Fig. 4, 5 *b*). Thus, the values of activation energy ε_1^{ρ} decrease from $\varepsilon_1^{\rho}(x = 0.05) = 138.6$ meV to $\varepsilon_1^{\rho}(x = 0.10) = 95.4$ meV and $\varepsilon_1^{\rho}(x = 0.15) = 50.9$ meV, and the rate of motion of the Fermi level ε_F in the concentration area $x = 0.10 – 0.15$ is $\Delta\varepsilon_F/\Delta x = 8.5$ meV/% *Ga*. From the obtained result it follows that despite generation of a large number of acceptors in the crystal ($p = 2.9 \cdot 10^{21}$ cm^{-3} for $x = 0.15$), the concentration of electrons is larger. This raises the question as to the mechanism of generation in the crystal of donors that are the source of free electrons.

The simultaneous generation in the crystal of the donor and acceptor structural defects is accompanied by a change in the compensation ratio, as well a change in the modulation amplitude of continuous energy bands of heavily doped compensated semiconductors [1,9] according to the law reflecting the ratio between ionized acceptors and donors. A change in the values of activation energy $\varepsilon_1^{\alpha}(x)$ which is proportional to the modulation amplitude of continuous energy bands of $TiNiSn_{1-x}Ga_x$ and reflects the compensation ratio of semiconductor [1, 9] seems to be interesting. From Fig. 6 it is seen that for *n-TiNiSn* the modulation amplitude is $\varepsilon_1^{\alpha}(x = 0) = 52.9$ meV, and introduction into *n*-type semiconductor of the lowest in the experiment concentration of *Ga* impurity drastically increases the compensation ratio, pointing to the appearance of defects of the opposite sign – acceptors, as evidenced by increase in the values of the modulation amplitude $\varepsilon_1^{\alpha}(x = 0.02) = 205.6$ meV. In so doing, electrons remain the majority carriers, which corresponds to the behaviour of the activation energy of $\varepsilon_1^{\rho}(x)$ $TiNiSn_{1-x}Ga_x$.

Further increase in the concentration of *Ga* atoms in $TiNiSn_{1-x}Ga_x$, $x > 0.02$ is accompanied by the decrease in the values of activation energy $\varepsilon_1^{\alpha}(x)$ from $\varepsilon_1^{\alpha}(x = 0.05) = 115.8$ meV to $\varepsilon_1^{\alpha}(x = 0.10) = 93.03$ meV and $\varepsilon_1^{\alpha}(x = 0.15) = 59.8$ meV, pointing to the reduction of compensation ratio, which can be only possible on condition of electrons appearing in a crystal by the hitherto unknown mechanism whose total concentration exceeds the concentration of generated holes.

Thus, the results of structural investigations (the behaviour of unit cell period $a(x)$) and kinetic investigations (the negative values of the Seebeck coefficient) of $TiNiSn_{1-x}Ga_x$ semiconductor material enable us to speak of a complicated mechanism for the simultaneous generation in the crystal of the acceptor and donor structural defects on introduction of *Ga* atoms into the structure of *TiNiSn* compound by the substitution of *Sn* atoms. Note that no such defects have been revealed by structural investigations of $TiNiSn_{1-x}Ga_x$, as long as their concentration is beyond the accuracy of X-ray investigation methods.

Refinement of crystalline and electronic structures of $TiNiSn_{1-x}Ga_x$

For the identification of structural defects in $TiNiSn_{1-x}Ga_x$ the method proposed in [1] was employed. The electronic structure of $TiNiSn_{1-x}Ga_x$ was calculated for different variants of atoms arrangement in the unit cell sites and for a different degree of occupancy of crystallographic positions of all atoms by proper or foreign atoms (Fig. 7).

We sought for such spatial arrangement of atoms in the unit cell (or their vacancies) of $TiNiSn_{1-x}Ga_x$ (the ratio between the donor and acceptor defects – compensation ratio), when the calculated rate and character of motion of the Fermi level ε_F will agree with the experimentally obtained numerical values of activation energy $\varepsilon_1^{\rho}(x)$ from the Fermi level ε_F to the edge of the conduction band. It turned out that the most acceptable version of atoms arrangement in $TiNiSn_{1-x}Ga_x$ provides for the emergence of vacancies in position (4 *b*) of *Sn* atoms whose concentration grows with increase in the number of *Ga* atoms.

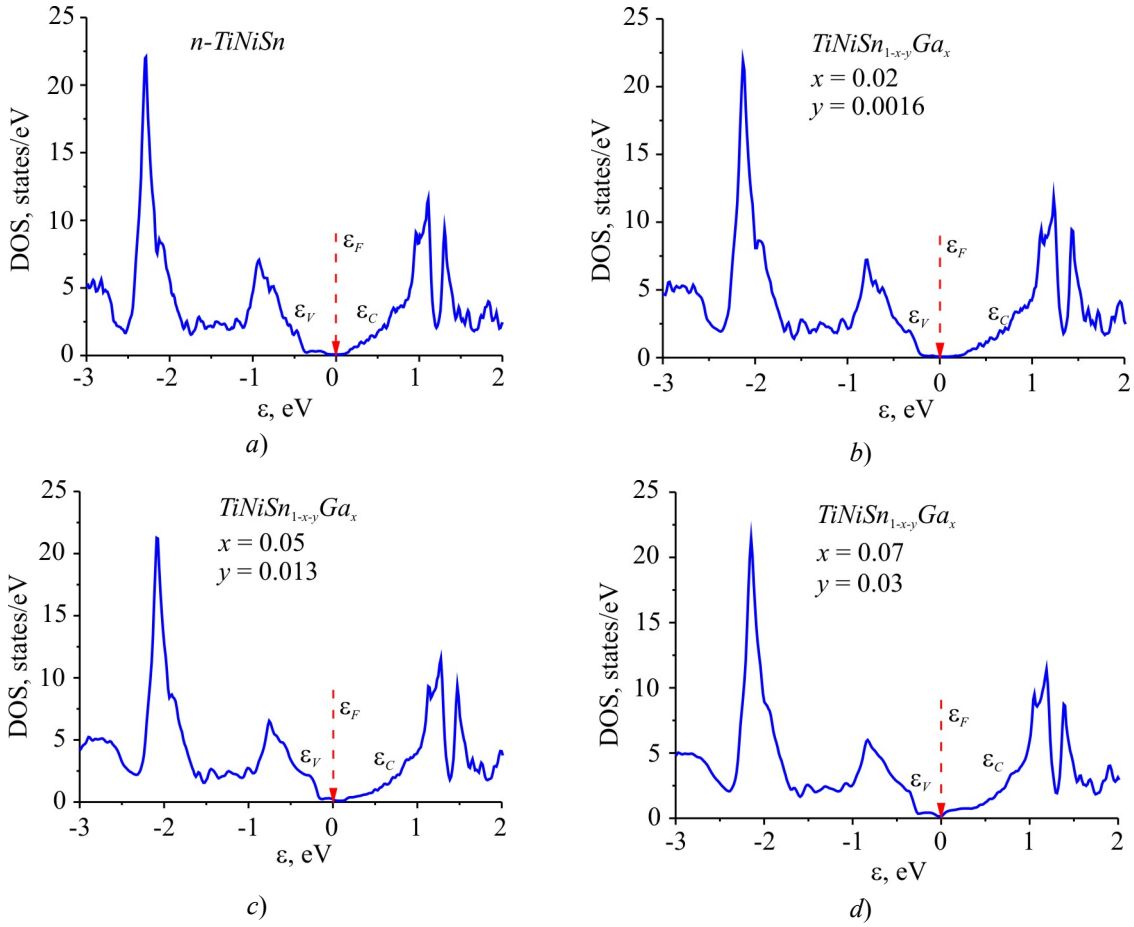

Fig. 7. Refined calculation of the electronic density of states of $TiNiSn_{1-x}Ga_x$.

In this case the formula of thermoelectric material can be written as $TiNiSn_{1-x-y}$, where y is concentration of vacancies in position (4 *b*) of *Sn* atoms. Based on the new results of the spatial arrangement of atoms in $TiNiSn_{1-x}Ga_x$ crystalline structure, more refined calculations were made of the electronic density of states distribution (Fig. 7) and, specifically, the density of states at the Fermi level $g(\varepsilon_F)$ that are consistent with the experimental results.

Conclusions

Thus, as a result of integrated research on the structural, energy and kinetic characteristics of *n-TiNiSn* intermetallic semiconductor heavily doped with *Ga* atoms, the mechanisms for the simultaneous generation in the crystal of the acceptor and donor structural defects have been identified that change the compensation ratio of thermoelectric material. The obtained results made it possible to reveal the features of electric conductivity mechanism at different concentrations and to develop ways for optimization of material parameters for getting maximum values of thermoelectric figure of merit [4].

The work was performed in the framework of grants of the National Academy of Sciences and Ministry of Education and Science of Ukraine, № 0113U007687 and № 0114U005464.

References

1. V.A.Romaka, V.V.Romaka, and Yu.V.Stadnyk, *Intermetallic Semiconductors: Properties and Application* (Lviv:Lvivska Polytechnika, 2011), 488 p.

2. Yu.V.Stadnyk, V.A.Romaka, Peculiarities of Electric Conductivity Mechanisms of Semiconductor Solid Solution $TiNiSn_{1-x}In_x$, *J.Thermoelectricity* 1, 43 – 51 (2007).
3. L.P.Romaka, Yu.V.Stadnyk, A.M.Goryn, Yu.K.Gorelenko, and Skolozdra, *MgAgAs* Structure Type Solid Solutions as a New Thermoelectric Material, *Proc.16th Intern. Conf. Thermoelectrics* (Dresden, Germany, 1997, 516 – 519).
4. L.I.Anatychuk, *Thermoelements and Thermoelectric Devices* (Kyiv: Naukova Dumka, 1979), 768 p.
5. T.Roisnel, J.Rodriguez-Carvajal, WinPLOTR: a Windows Tool for Powder Diffraction Patterns Analysis, *Mater. Sci. Forum, Proc. EPDIC7*, **378 – 381**, 118 – 123 (2001).
6. M.Schruter, H.Ebert, H.Akai, P.Entel, E.Hoffmann, and G.G.Reddy, First-Principles Investigations of Atomic Disorder Effects on Magnetic and Structural Instabilities in Transition-Metal Alloys, *Phys. Rev. B* **52**, 188 – 209 (1995).
7. V.L.Moruzzi, J.F.Janak, and A.R.Williams, *Calculated Electronic Properties of Metals* (NY: Pergamon Press, 1978), 348 p.
8. V.A.Romaka, P.Rogl, V.V.Romaka, E.K.Hlil, Yu.V.Stadnyk, and S.M.Budgerak, Features of «a priori» Heavy Doping of the *n-TiNiSn* Intermetallic Semiconductor, *Semiconductors* 45, 850 – 856 (2011).
9. B.I.Shklovsky, *Electron Properties of Doped Semiconductors* (Moscow: Nauka, 1979), 416 p.

Submitted 24.06.2016.

M.O. Haluschak[1], S.I. Mudryi[2], M.A. Lopyanko[3], S.V. Optasyuk[4], T.O. Semko[3], L.I. Nikiruy[3], I.V. Horichok[3]

[1]Ivano-Frankivsk National Technical University of Oil and Gas,
15, Karpatska St., Ivano-Frankivsk, 76018, Ukraine;
[2]I.Franko National University of Lviv,
6, Kyrylo and Mefodiy St., Lviv, 79005, Ukraine;
[3]V.Stefanyk Precarpathian National University,
57, Shevchenko St., Ivano-Frankivsk, 76018, Ukraine;
[4] Kamyanets-Podilsky State University,
61, I.Ohienko St., Kamyanets-Podilsky, 32300, Ukraine

PHASE COMPOSITION AND THERMOELECTRIC PROPERTIES OF MATERIALS IN *Pb-Ag-Te* SYSTEM

The phase composition and thermoelectric properties of silver doped lead telluride with impurity concentration 0.3, 0.5, 1.0 at. % and of $Pb_{18-x}Ag_2Te_{20}$ (x = 0, 0.5, 1.0) and $Pb_{17}Ag_3Te_{20}$. solid solutions were investigated. It was established that Pb phase exists in the samples on doping, and Te and $Ag_{10.6}Te_7$ exist in solid solutions. All materials under study are characterized by high values of the Seebeck coefficient (> 300 μV/K), and the samples of solid solutions, in addition, exhibit low thermal conductivity (≈ 0.003 W/(cm·K)).

Key words: lead telluride, doping, solid solutions, thermoelectric properties.

Introduction

In recent years, considerable gain in thermoelectric figure of merit of materials based on lead telluride has been achieved due to creation of a new class of $Ag_xPb_mSb_{2-x}Te_{m+2}$ (LAST) compounds [1 – 5]. The atoms of silver and antimony in these materials occupy positions in the cation sublattice, and, since the former is acceptor and the latter – donor, they compensate the electric action of each other, without having a significant impact on carrier concentration. However, nanosize violations of crystal lattice periodicity created in the regions rich in *Ag* and *Sb* effectively scatter phonons which results in considerable reduction of thermal conductivity. Despite the large number of papers dedicated to four-component systems, the properties of materials in *Pb-Ag-Te* system are much less studied. However, such studies can serve the basis for further modification of thermoelectric characteristics of LAST four-component systems.

Silver impurity in lead telluride can exhibit both acceptor properties, substituting for lead atoms, and donor properties, being arranged in the interstitial voids [6]. This fact complicates obtaining of *PbTe*: *Ag* material with the assigned conductivity, and therefore in practice for obtaining of *p*-type conductivity material silver is not often used. Instead, such acceptor impurities as sodium and thallium are much more actively studied and used in practice. However, the use of *Na* or *Tl* is involved with a number of problems, since thallium is rather toxic, and sodium is exceptionally sensitive to the conditions of storage and use. Thus, silver can be an alternative to the aforementioned materials that are used for obtaining of *p-PbTe*.

Structural and thermodynamic properties of *Pb-Te-Ag* system were studied in [7 – 9]. Silver with tellurium forms a number of refractory compounds which must be taken into account in the synthesis. In [10], based on ab initio calculations, it was established that silver substituted for lead in cation site increases considerably the density of states at the edge of the valence band, which contributes to growth of the Seebeck coefficient. The electrophysical properties of *PbTe-Ag* were studied in [12 – 14]. Based on their analysis we can conclude that the electric activity of impurity is largely determined by the conditions for obtaining a prototype. Thus, at impurity concentration 0.5 at. % carrier concentration achieved in [12] was $\approx 2 \cdot 10^{18}$ cm^{-3}, and in [13] – $\approx 10^{19}$ cm^{-3}. So, to establish factors affecting the behaviour of *Ag* impurity is the task of vital importance.

In this paper, when choosing chemical compositions of doped samples, the goal was to study both homogeneous samples and at the interface of and beyond the impurity solubility region. In the case of solid solutions compositions were selected in the vicinity of LAST-18 ($Pb_{18}Ag_1Sb_1Te_{20}$) system as one of the most promising thermoelectric materials, and lead content was varied in addition with a view to control metal vacancies concentration in order to increase the electric conductivity of samples.

Experimental procedure

Synthesis of materials was performed in quartz ampoules evacuated to residual pressure 10^{-4} Pa. Use was made of substances with the content of basic component 99.99 % (metals and chalcogens) which were subject to additional purification. Weighing was performed on the analytical balance VLR-200M to an accuracy of 0.05 mg. To increase the homogeneity of compounds in the process of synthesis, they were subject to forced mixing. Cooling was done at a rate of 5 K/h to temperature 600 °C, and subsequently – at a rate of 10 °C/h.

The obtained ingots were ground in agate mortar and, on separation of fractions (0.05 – 0.5) mm, were pressed under 1.5 GPa. The resulting cylinder-shaped samples with $d = (5 – 8)$ mm and $h \approx (8 – 12)$ mm were annealed in the air at temperature $T = 500$ K for 5 hours.

Phase composition and structure of synthesized ingots and samples were studied by X-ray diffraction methods on automatic diffractometer STOE STADI P (manufactured by "STOE & Cie GmbH", Germany). Processing of the experimental diffraction arrays was performed by means of software packages STOE WinXPOW (version 3.03) and PowderCell (version 2.4). Refinement of crystalline structure of phases for selected samples in the isotropic approximation for atomic displacement parameters was performed by the Rietveld method using FullProf. 2 k program (version 5.30).

The Hall measurements were performed in constant magnetic and electric fields by the four-probe method. Current through the samples was ≈ 100 – 500 mA. The magnetic field was directed perpendicular to the longitudinal axis of cylinder sample at induction 1.5 T.

The Seebeck coefficient α, electric conductivity σ and thermal conductivity *k* were determined by the methods described in [15, 16].

Discussion of the results

The results of X-ray diffraction studies are represented in Table and in Fig. 1. Samples of undoped material are single-phase and characterized by *n*-type conductivity. On introduction of impurity, traces of pure lead phase become apparent (Fig. 1 *b*).

Table

Results of X-ray diffraction analysis and measurement of the Hall effect (at room temperatures) of pressed and annealed samples of PbTe: Ag and $Pb_{18-x-y}Ag_xTe_{20}$

Sample	Chemical composition	Phase composition	Unit cell parameter a, Å[1]	Carrier concentration $n(p)$, cm^{-3}
15 – 18 2*S*	$Pb_{0.5}Te_{0.5}$	*PbTe*	6.4565	$4.9\ 10^{18}$
15 – 22 1*S*	$Pb_{0.5}Te_{0.5}$+0.3 at.% *Ag*	*PbTe*, traces of *Pb*	6.4561	$8.46\ 10^{17}$
15 – 23 1*S*	$Pb_{0.5}Te_{0.5}$+0.5 at.% *Ag*	*PbTe*, traces of *Pb*	6.4571	$1.2\ 10^{18}$
15 – 21 1*S*	$Pb_{0.5}Te_{0.5}$+1.0 at.% *Ag*	*PbTe*, traces of *Pb*	6.4552	$6.4\ 10^{17}$
16 – 13 2*S*	$Pb_{18}Ag_2Te_{20}$	*PbTe*, traces of $Ag_{10.6}Te_7$	6.4571	$1.4\ 10^{18}$
16 – 14 2*S*	$Pb_{17.5}Ag_2Te_{20}$	*PbTe*, traces of *Te* and $Ag_{10.6}Te_7$	6.4582	$1.2\ 10^{18}$
16 – 15 1*S*	$Pb_{17.0}Ag_2Te_{20}$	*PbTe*, traces of *Te* and $Ag_{10.6}Te_7$	6.4576	$1.3\ 10^{18}$
XIX	$Pb_{17}Ag_3Te_{20}$	*PbTe*, traces of *Te* and $Ag_{10.6}Te_7$	6.4592	$1.1\ 10^{18}$

[1]Note. Absolute error is ± 0.0005

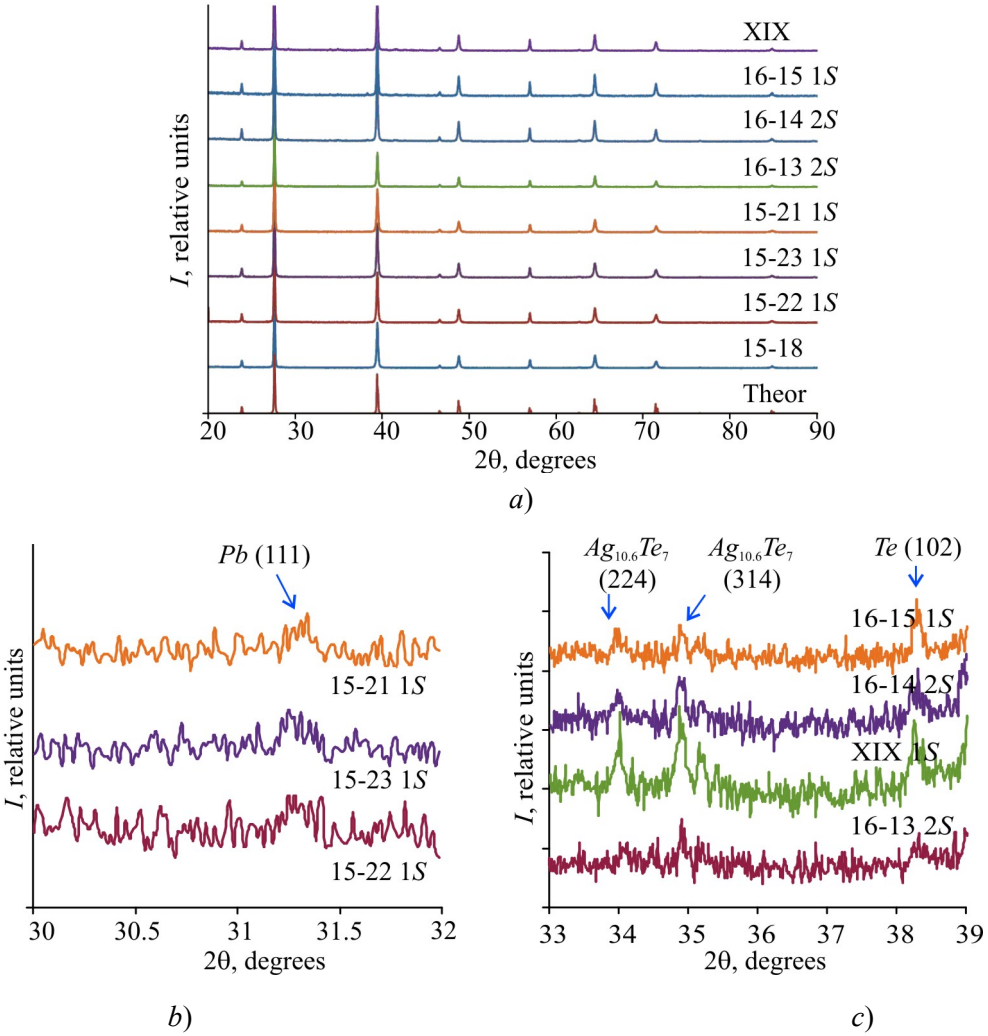

Fig. 1. X-ray patterns of Pb-Ag-Te samples under investigation (see Table 1) (a) and X-ray pattern fragments in the area of detected Pb phase reflexes for doped PbTe: Ag (b) and Te and $Ag_{10.6}Te_7$ phases for PbAgTe solid solutions (c).

For $Pb_{18}Ag_2Te_{20}$, $Pb_{17.5}Ag_2Te_{20}$, $Pb_{17.0}Ag_2Te_{20}$ solid solutions the lattice constant and carrier concentration are practically equal, and for a sample of $Pb_{17}Ag_3Te_{20}$ composition the lattice constant is greater. For all samples of *Pb-Ag-Te* solid solutions on X-ray diffraction patterns there is an additional phase of *Te* and $Ag_{10.6}Te_7$ (Fig. 1 *b*) [17]. The latter is due to over limits of impurity solubility region, and the former – due to considerable excess of chalcogen in the charge as compared to stoichiometric composition.

Silver doping results in considerable reduction of electric conductivity (Fig. 2 *a*), but no *p*-type transition takes place. The Seebeck coefficient of samples with impurity content 0.3 and 0.5 at. % *Ag* is almost the same and monotonically decreases from the values 500 μV/K at 100 °C to the values 350 μV/K at 350 °C. The temperature dependence of the Seebeck coefficient of samples with impurity content 1 at. % *Ag* is characterized by nonmonotonic behaviour with the maximum 400 μV/K at 200 °C. The thermal conductivity coefficient weakly grows with increase in impurity amount.

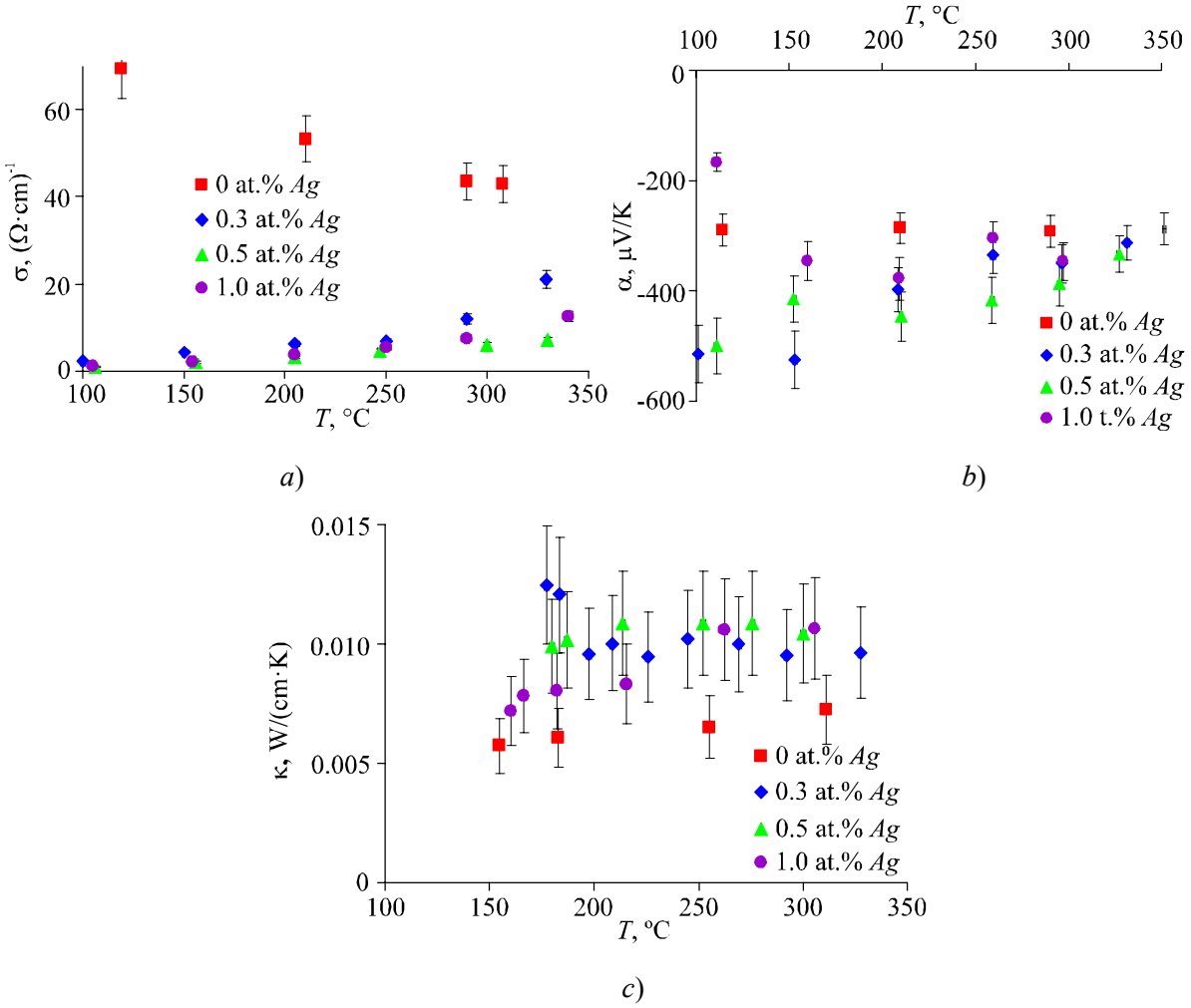

Fig. 2. Temperature dependences of electric conductivity σ (a), the Seebeck coefficient α (b) and thermal conductivity coefficient k (c) of PbTe (■), PbTe: Ag (0.3 at. %) (●), PbTe: Ag (0.5 at. %) (▲), PbTe: Ag (1.0 at. %) (♦) samples.

Unlike doped material, a stable *p*-type conductivity was obtained for all $Pb_{18-x}Ag_{2(3)}Te_{20}$ ($x = 0$; 0.5; 1.0) compositions under study. From Fig. 3 *a* it is seen that material has higher electric conductivity as compared to doped material. There is a marked increase in σ value with a decrease of

lead content in solution, though according to the Hall measurements, carrier concentration is practically unchanged (Table). The Seebeck coefficient for all $Pb_{18-x}Ag_2Te_{20}$ compositions is almost the same and makes ≈ 300 μV/°C at 300 °C. The thermal conductivity coefficient is reduced with decreasing content of lead in solution, which is attributable to increased number of lead vacancies on which phonons are scattered. The lowest k value is typical of samples with $Pb_{17}Ag_3Te_{20}$ composition. It is important that the peaks of additional $Ag_{10.6}Te_7$ phase are most intensive for the sample.

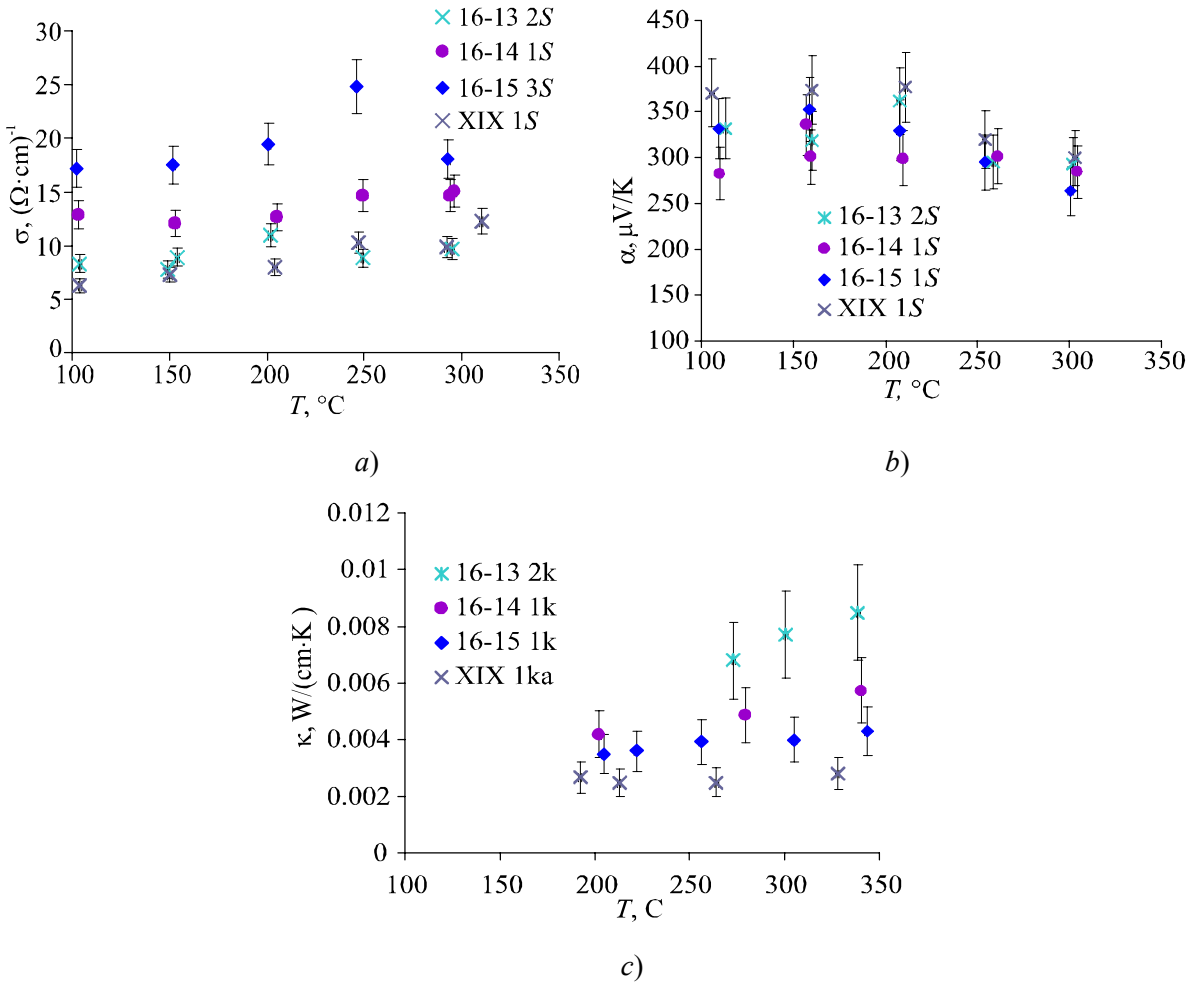

Fig. 3. Temperature dependences of electric conductivity σ (a), the Seebeck coefficient α (b) and thermal conductivity coefficient k (c) of $Pb_{18}Ag_2Te_{20}$ (×), $Pb_{17.5}Ag_2Te_{20}$(●), $Pb_{17.0}Ag_2Te_{20}$(♦) samples.

Thus, one can state a weak acceptor effect of silver in *PbTe*, to investigate into the reasons of which it is necessary to perform crystallochemical or thermodynamic analysis of defective subsystem. However, for doped *PbTe*: *Ag* material on the basis of established growth of lattice constant with increase in *Ag* content and appearance of traces of pure lead phase, an assumption can be made on silver substitution for lead atoms, by their displacement into interstices with subsequent precipitation. As long as interstitial lead atom is a double donor, and silver atom in the cation site – a single acceptor, it can account for a weak acceptor effect of silver and impossibility of material converting into *p*-type conductivity. In the case of solid solutions the electrophysical effect of silver is more pronounced as compared to doped material. Moreover, inclusions of additional phases reduce the thermal conductivity considerably, which is important from practical standpoint.

Conclusions

1. Silver impurity in lead telluride shows a weak acceptor effect, the concentration of acceptor defects is considerably lower than the concentration of introduced *Ag* atoms, and the most probable doping mechanism is substitution of silver atoms in crystal lattice for lead atoms. Doped material is characterized by high values of the Seebeck coefficient (≈ 500 μV/K at. 0.3 – 0.5 at. % *Ag*), which can be used for creation of bolometers on its basis.
2. $Pb_{18}Ag_2Te_{20}$, $Pb_{17.5}Ag_2Te_{20}$, $Pb_{17.0}Ag_2Te_{20}$ and $Pb_{17}Ag_3Te_{20}$ solid solutions are characterized by the presence of inclusions of additional *Te* and $Ag_{10.6}Te_7$ phases which determine low values of thermal conductivity (0.003 W/(cm · K)) and high in a wide range values of the Sebeck coefficient (≈ 300 μV/K), which is necessary for practical use of material in thermoelectric converters.

References

1. K-F. Hsu, S.Loo, F.Guo, W.Chen, J.S.Dyck, C.Uher, T.Hogan, E.K.Polychroniadis, and M.G.Kanatzidis, *Science* **303** (5659), 818 (2004).
2. H.Hazama, U.Mizutani, *Phys. Rev. B* 73, 115108 (2006).
3. E.Quarez, K.-F.Hsu, R.Pcionek, N.Frangis, E.K.Polychroniadis, and M.G.Kanatzidis, *J. Am.Chem. Soc*. 127, 9177 (2005).
4. J.Sootsman, R.Pcionek, H.Kong, C.Uher and M.G.Kanatzidis, *Mater. Res. Soc. Symp. Proc*. 886, 0886-F08-05 (2006).
5. D.Bilc, S.D.Mahanti, E.Quarez, K.-F.Hsu, R.Pcionek, and M.G.Kanatzidis, *Phys. Rev. Lett.* 93, 146403 (2004).
6. B.A.Volkov, L.I.Ryabova, and D.R.Khokhlov, *Advances in Physical Sciences* **178** (8), 875 (2002).
7. W.Gierlotka, J.Lapsa, and K.Fitzner, *J. Phase Equilibria and Diffusion* **31** (6), 509 (2010).
8. M.K.Sharov, *Inorganic Materials* **44** (6), 569 (2008).
9. M.K.Sharov, *Russian Journal of Inorganic Chemistry* **54** (1), 33 (2009).
10. K.Hoang, D.Mahanti, and P.Jena, *Phys Rev B* 76, 115432 (2007).
11. A.V.Dmitriev, I.P.Zviagin, *Advances in Physical Sciences* **180** (8), 821 (2010).
12. M.K.Sharov, *Semiconductors* **46** (5), 613 (2012).
13. L.D.Borisova, *Phys. Stat. Sol. A* 53, K19 (1979).
14. H.S.Dow, M.W.Oh, B.S.Kim, S.D.Park, B.K.Min, H.W.Lee, and D.M.Wee, *J.Applied Physics* 108, 1137709 (2010).
15. D.M.Freik, C.A.Kryskov, I.V.Horichok, T.S.Lyuba, O.S.Krynytsky, and O.M.Rachkovsky, *J.Thermoelectricity* 2, 42 (2013).
16. D.M.Freik, R.Ya.Mykhailyonka, and V.M.Klanichka, *Physics and Chemistry of Solid State* **5** (1), 173 (2004).
17. J.Peters, O.Conrad, B.Bremer, and B.Z.Krebs, *Z. Anorg. Allg. Chem*. 622, 1823 (1996).

Submitted 27.06.2016.

L.I. Anatychuk

L.I. Anatychuk[1,2], R.V. Kuz[1]

[1]Institute of Thermoelectricity, 1, Nauky Str.,
Chernivtsi, 58029, Ukraine;
[2]Yu.Fedkovych Chernivtsi National University
2, Kotsyubinsky str., Chernivtsi, 58012 Ukraine

R.V. Kuz

THERMOELECTRIC GENERATOR FOR TRUCKS

The results of computer simulation of thermoelectric generators (TEG) using the exhaust heat of internal combustion engines were presented. The simulation was done with regard to dynamic modes of engine operation on the basis of real records of monitoring system with the use of real parameters of thermoelectric modules.

Key words: thermoelectric generator, internal combustion engines.

Introduction

The use of waste heat from the internal combustion engines is one of the critical tasks of thermoelectricity. World producers of vehicles, as well as companies of thermoelectric profile, give much prominence to the development of efficient automotive thermoelectric generators [1 – 8]. The purpose is to increase fuel saving up to 10 % due to the use of engine exhaust heat for electric energy generation.

The largest companies making it their mission to create industrial prototypes of generators and their large-scale production are Hi-Z, BSST and General Motors in the USA. In Japan, the problems of creating automotive generators are most widely addressed by companies Komatsu, Nissan and Shiroki. In Germany, company Volkswagen and company BMW together with DLR (German Airspace Centre) represented their developments of thermoelectric automotive generators.

The lack of broad application of automotive TEG is attributable to insufficiently high generator efficiency. The generator efficiency essentially depends on the engine operating mode. The dynamic modes of engine operation during an actual drive impose fairly complicated requirements to design and optimization of automotive generators that cannot be fully met so far. One of optimization components is TEG design for a specific engine type and its priority operating mode. Particular attention is claimed by trucks with heavy engines and, accordingly, large amount of exhaust heat.

The purpose of this work is to design a thermoelectric generator which utilizes the exhaust heat of truck engine.

Optimization of a thermoelectric generator is done by computer design [10] which is as follows.

Computer design procedure

Let us consider a physical model of thermoelectric generator (TEG) shown in Fig. 1. In the general case a TEG is composed of N sections connected in series with respect to hot gas flow and cold heat carrier.

Each TEG section comprises the following components (Fig. 1): hot heat exchanger (1), thermopile (3) with thermal resistance $R_t^{(i)}$ and efficiency $\eta(T_H, T_0)$; cold heat exchanger (4) with

temperature T_0; thermal resistance between the hot heat exchanger and thermopile $R_t^{(i)}$ (2), which restricts the hot side temperature of modules. The thermopiles of each section are closed to the matched electric load R_i (5).

The inlet hot gas flow is characterized by temperature T_H^{in} and thermal power Q_H^{in}. The hot gas gives part of heat $Q_H^i(x)$ at temperature $T_{hot}^{(i)}(x)$ to the hot heat exchanger. At the outlet of TEG, gas temperature is T_H^{out} and thermal power is Q_H^{out}. The heat from the hot heat exchanger is transferred through thermal resistance $R_t^{(i)}$ to thermopile, heating its hot side to temperature $T_H^{(i)}(x)$.

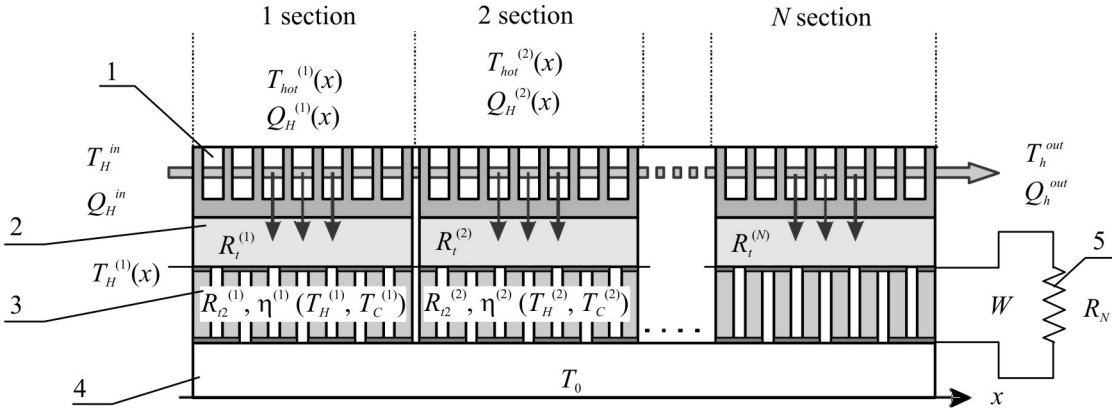

Fig. 1. Physical model of thermoelectric generator:
1 – hot heat exchanger; 2 – thermal resistance between the hot heat exchanger and thermopile; 3 – thermopile; 4 – cold heat exchanger; 5 – matched electric load.

To avoid overheating of thermoelectric modules, the physical model will be supplemented with a bypass through which the excess exhaust gas will be rejected so as to maintain the temperature of modules on maximum permissible level.

For the optimization of TEG it is necessary to find the distribution of temperatures and heat fluxes in each section. Such calculation for this model was done by using numerical computer methods.

For the calculations of TEG electric power we use energy balance equation in the form

$$W = \sum_{i=1}^{N}\left[\int\left(Q_H^{(i)}(x) - Q_C^{(i)}(x)\right)dx\right]. \tag{1}$$

The necessary temperatures and heat flows are found from thermal conductivity equation

$$-\nabla\left(\kappa_{TE}(T)\nabla T\right) = Q_J, \tag{2}$$

where κ_{TE} is effective thermal conductivity of thermopile, Q_J is the Joule heat which is released in the bulk of the thermopile.

The boundary conditions for (2) will be given by

$$Q_H^{in(1)} = Q_H^{in},\ Q_H^{in(i+1)} = Q_H^{out(i)},\ Q_H^{out(N)} = Q_H^{out}, \tag{3}$$

$$Q_H^{(i)}(x) = \left(T_H^{(i)}(x) - T^{(i)}(x)\right) / R_t^{(i)}, \tag{4}$$

$$Q_C^{(i)}(x) = \left(T_0(x) - T^{(i)}(x)\right) / R_{t2}^{(i)}, \tag{5}$$

A set of relations (1) – (5) allows determining the distribution of temperatures $T_H^{(i)}(x)$ and

thermal flows $Q_H^{(i)}(x)$ in each section.

To restrict the hot temperature of module, thermal resistance $R_t^{(i)}$ between the hot heat exchanger and thermoelectric module is found from equation (4).

The power of each section and general efficiency of TEG can be found from equations

$$W^{(i)} = \int Q_H^{(i)}(x)\eta(T_H^{(i)}(x), T_0)dx\,, \tag{6}$$

$$\eta_{TEG} = \frac{1}{Q_H^{in}}\sum_{i=1}^{N} W^{(i)}\,. \tag{7}$$

The system of equations (1) – (5) is solved by numerical methods on a two-dimensional finite element mesh [10].

Computer design results

Design of a thermoelectric generator in a dynamic mode was performed with the use of exhaust gas input parameters (temperature and flow rate) obtained on the exhaust system of truck CAT 775F for engine Navistar 13 L [11] of power 330 kW for different engine modes:

1 – performing standard tasks by truck.

2 – operation of truck engine at close to nominal load (speed – 1500 RPM, turning torque – 1100 N·m).

Fig. 2 shows the exhaust gas temperature, Fig. 3 – the exhaust gas flow rate for the case of engine operation at nominal load.

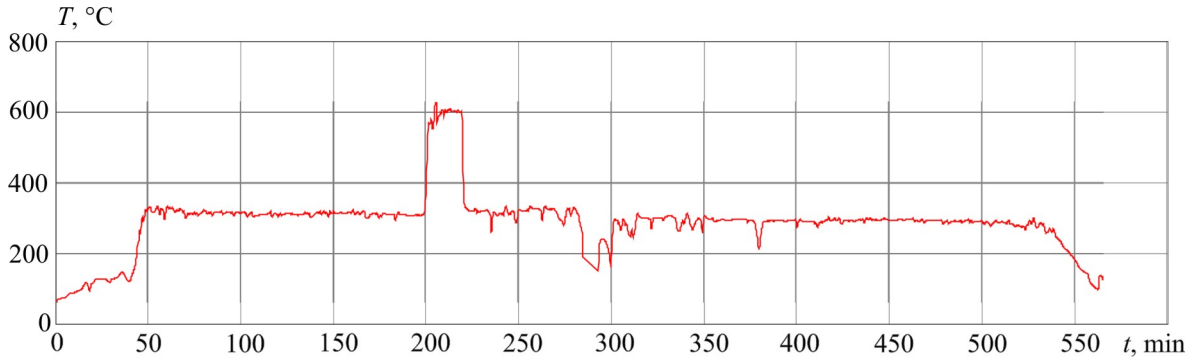

Fig. 2. Exhaust gas temperature for engine nominal operation.

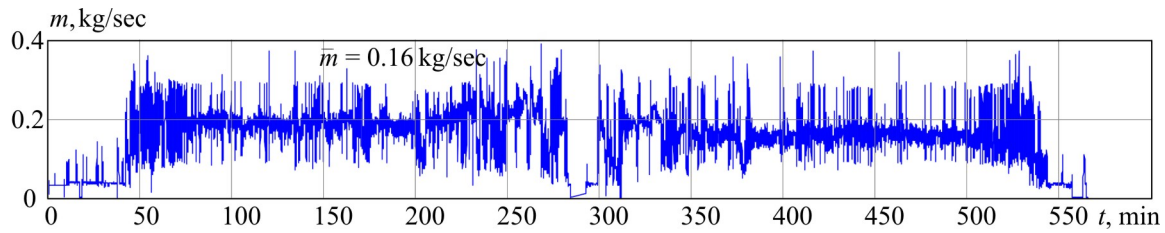

Fig. 3. Exhaust gas flow rate for engine nominal operation.

To design a generator, the thermoelectric modules ALTEC-1061 [17] based on *Bi-Te* were selected that outperform known world analogs.

The generator design optimization consisted in determining the minimum number of modules necessary for achievement by the generator of maximum average electric power within the operating cycle represented in Fig. 2 – 3. Fig. 4 shows the results of this optimization.

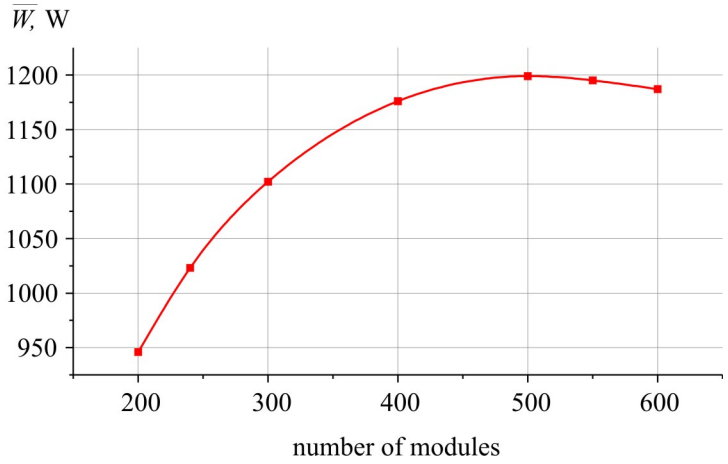

Fig. 4. Dependence of the average electric power of TEG on the number of modules.

It can be observed that for the task in hand the optimal number of modules is ~ 500. With a downward deviation from the optimal value the hot side temperature of modules can be raised to higher values, however, the total electric power of TEG drops due to small number of modules. A drop in the electric power of TEG is also observed with an upward deviation from the optimal number of modules. This is due to a decrease in total thermal resistance of thermopile, and, as a consequence, a decrease in temperature difference on the modules.

Fig. 5 shows time dependences of the hot side temperature of modules. The cold side temperature is assumed to be T_0 = 60 ºC.

Fig. 6 shows time dependence of the electric power of TEG. The average electric power throughout the cycle was ~ 1200 W.

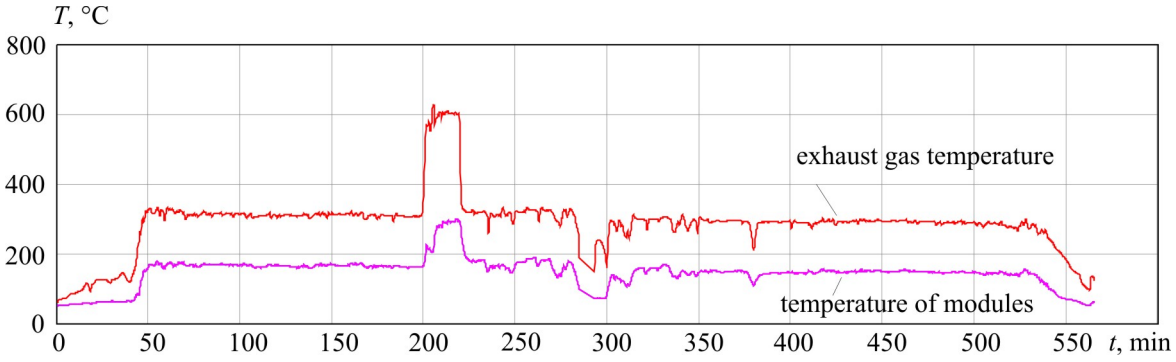

Fig. 5. Time dependence of the hot temperature of modules for engine nominal operation.

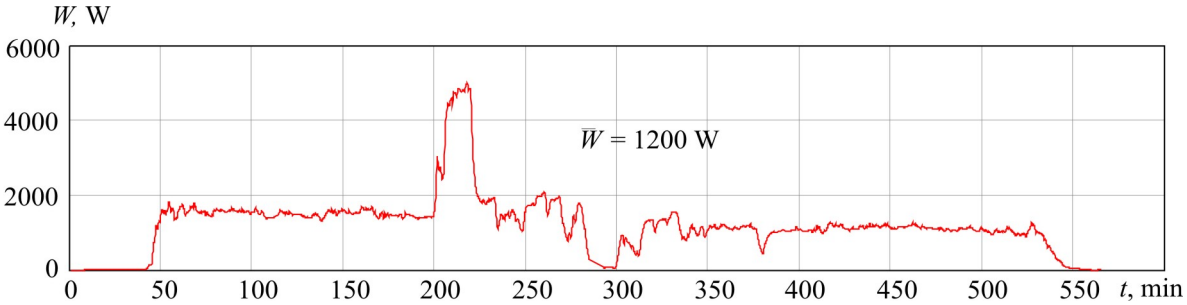

Fig.6. Electric power of TEG for engine nominal operation.

In so doing, the average efficiency of thermoelectric generator in one cycle is 2.2 %.

Generator optimization for alternative mode of operation – performing standard tasks by truck – yielded the following results.

Fig. 7 shows the result of optimization of the average electric power of TEG in one complete operating cycle.

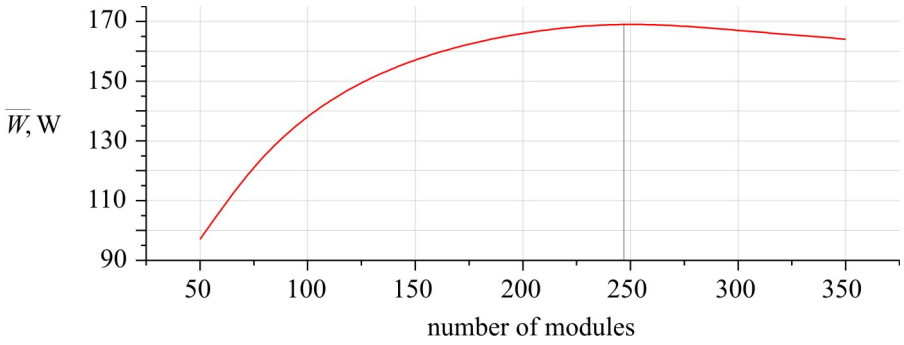

Fig. 7. Dependence of the average electric power of TEG on the number of modules.

Fig. 8 shows time dependences of the hot side of modules when performing standard tasks by truck. The cold side temperature is assumed to be T_0 = 60 ºC. Fig. 9 shows the electric power of TEG in this operating mode.

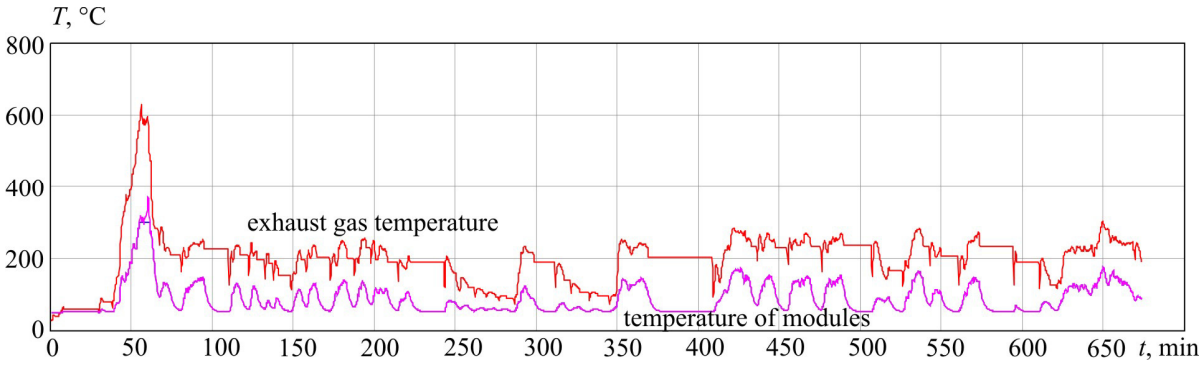

Fig. 8. Time dependence of gas temperature and the hot temperature of modules.

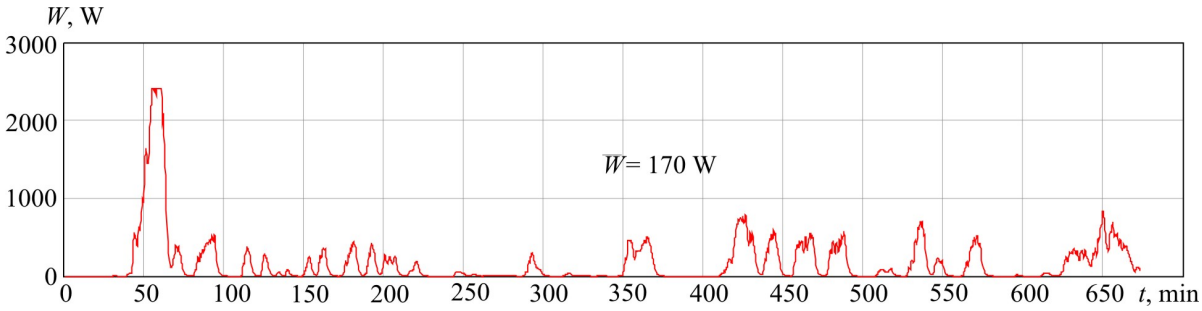

Fig. 9. Electric power of TEG.

A TEG optimized for this operating mode comprises ~ 250 thermoelectric modules and develops average electric power 170 W. The efficiency of TEG in this case is 1.7 %. Such a low value is caused by low exhaust gas temperatures.

Conclusions

1. A thermoelectric generator for truck diesel engine of power 330 kW was designed for nominal

load operation of engine and for the mode of performing standard tasks by truck.

2. It was shown that at nominal load operation of engine the TEG can produce on the average ~ 1200 W of electric energy at efficiency 2.2 %.
3. When performing standard tasks by trucks, the average electric power developed by TEG is 170 W and efficiency 1.7 %. The low values of power and efficiency are caused by low temperature of truck exhaust gases.

References

1. T.Kajikawa and T. Onishi, Development for Advanced Thermoelectric Conversion Systems, *Proc. of 26th International Conference on Thermoelectrics (Jeju, Korea,2007),* p. 353 – 361
2. G.Min, D.M.Rowe, Conversion Efficiency of Thermoelectric Combustion Systems, *IEEE Transactions on Energy Conversion* 22, 528 – 534 (2007).
3. K.M.Sacr, M.K.Mansour, and M.N.Mussa, Thermal Design of Automobile Exhaust Based on Thermoelectric Generators: Objectives and Challenges, *J.Thermoelectricity* 1, 64 – 73 (2008).
4. X.Zhang, K.T.Chau, and C.C.Chan, Overview of Thermoelectric Generation for Hybrid Vehicles, *Journal of Asian Electric Vehicles* **6**(2), 1119 – 1124 (2008).
5. D.Crane, L.Bell, Progress Towards Maximizing the Performance of a Thermoelectric Power Generator, *Proc. 25th International Conference on Thermoelectrics (Vienna, Austria, 2006),* p. 11 – 16.
6. L.I.Anatychuk and R.V.Kuz, Computer Designing and Test Results of Automotive Thermoelectric Generator, *Proc. of "Thermoelectrics Goes Automotive"* (Berlin: Expert Verlag, 2011).
7. L.I.Anatychuk, O.J.Luste, and R.V.Kuz, Theoretical and Experimental Studies of Thermoelectric Generator for Vehicles, *J. Electronic Materials* **40**(5), 1326 – 1331(2011).
8. L.I.Anatychuk and R.V.Kuz, Computer Designing and Test Results of Automotive Thermoelectric Generator, *Proc. of "Thermoelectrics Goes Automotive"* (Berlin, 2010).
9. Comsol multiphysics. http://www.comsol.com.
10. L.I.Anatychuk, R.V.Kuz, Materials for Vehicular Thermoelectric Generators, *J.Electronic Materials* **41**(6) (2012).
11. http://www.navistar.com.

Submitted 20.06.2016.

I.A. Konstantynovych

I.A. Konstantynovych[1,2]

[1]Institute of Thermoelectricity of the NAS and MES of Ukraine,
1, Nauky str., Chernivtsi, 58029, Ukraine;
[2]Yu.Fedkovych Chernivtsi National University
2, Kotsyubinsky str., Chernivtsi, 58012 Ukraine

ON THE EFFICIENCY OF GYROTROPIC THERMOELEMENTS IN COOLING MODE

Computer simulation of temperature fields for gyrotropic thermoelements of the rectangular, spiral and optimal shapes was performed. BiSb, Ag_2Te and InSb thermoelectric materials for gyrotropic thermoelements were considered. The temperature dependences for gyrotropic thermoelements of various shapes were obtained. It was shown that in the temperature range of 150 – 300 K it is reasonable to use Ag_2Te, whereas BiSb can be efficiently used in the range of 80 – 120 K.

Key words: gyrotropic thermoelement, magnetic field, thermoelectric material, figure of merit.

Introduction

The generalized theory of thermoelectricity allowed developing methods for the discovery of new thermoelement types, and their application in anisotropic media made it possible to devise, investigate and create a number of fundamentally new thermoelement types with unique properties that expanded essentially the opportunities of thermoelectricity.

A promising direction in the development of thermoelectric applications is devising new thermoelement types based on gyrotropic media [1 – 19]. These opportunities of thermoelectricity are little studied, and their implementation will make it possible to expand the element basis of thermoelectricity, to improve the competitiveness of thermoelectric power converters, as well as to create on their basis the thermoelectric products of enhanced performance.

The relevance of this work lies in the need to improve the efficiency and reliability of thermoelectric power converters based on gyrotropic media to be used in instrument engineering.

The purpose of this work is to estimate the efficiency of gyrotropic thermoelements in cooling mode.

Mathematical model

Thermal conductivity equation for a homogeneous gyrotropic medium is given by

$$\kappa\Delta T + \rho_0 j^2 + 2\alpha_B\left(j_y\frac{\partial T}{\partial x} - j_x\frac{\partial T}{\partial y}\right) = 0, \qquad (1)$$

where κ is thermal conductivity coefficient of a gyrotropic medium; ρ_0 is electrical resistivity; j is electrical current density vector; j_x, j_y are projections of vector $\mathbf{j}$ in the Cartesian coordinate system; $\alpha_B = Q_\perp B$ is the asymmetric part of thermoEMF tensor which in a gyrotropic medium is of the form

$$\alpha = \begin{pmatrix} \alpha_0 & \alpha_B & 0 \\ -\alpha_B & \alpha_0 & 0 \\ 0 & 0 & \alpha_\perp \end{pmatrix}, \tag{2}$$

where $Q_\perp$ is the Nernst-Ettingshausen coefficient.

With regard to the axial symmetry of the system, we write Eq.(1) in the polar coordinate system

$$\kappa \Delta T + \rho_0 j^2 + 2Q_\perp B\left(j_\varphi \frac{\partial T}{\partial r} - \frac{j_r}{r}\frac{\partial T}{\partial \varphi} \right) = 0, \tag{3}$$

where j_r, j_φ are the radial and azimuthal components of current density vector $\mathbf{j}$, $r_1 \le r \le r_2$ is thermoelement radius.

Assuming that the hot side (T_1) is adiabatically isolated and ignoring the losses through the lateral surfaces, one can use the known formula for the calculation of maximum temperature difference between thermoelement sides ΔT_{max} [5]

$$(\Delta T)_{max} = \frac{1}{2} T_1^2 \frac{\alpha_B^2}{\rho_0 \kappa}. \tag{4}$$

Computer simulation results

There is a variety of literary sources describing the properties of gyrotropic materials for low-temperature region [1, 2]. Fig. 1 presents the temperature dependences of figure of merit of *BiSb, Ag_2Te* and *InSb* materials [1, 3, 4].

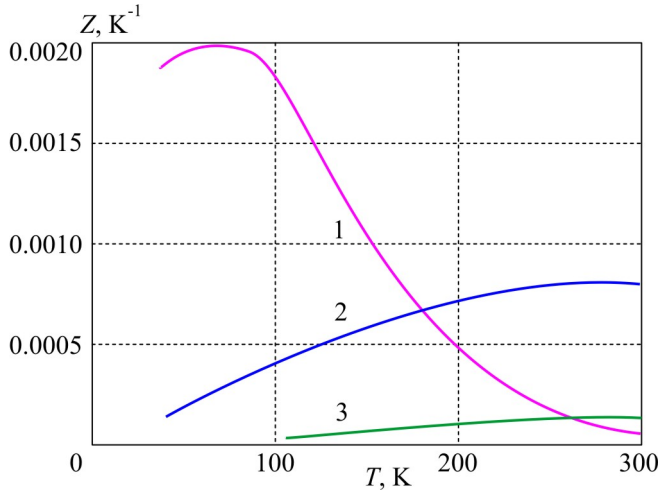

Fig. 1. Figure of merit Z shown as a function of temperature T (1 – BiSb, 2 – Ag_2Te, 3 – InSb) [1, 3, 4].

For the construction of computer model of gyrotropic thermoelements of rectangular, spiral and optimal shapes the Comsol Multiphysics application software package was used [20]. The calculation of temperature distributions in gyrotropic thermoelements was done by finite element method. Computer simulation was used to determine temperature distributions in gyrotropic thermoelements of various shapes for Ag_2Te material in a magnetic field with induction $B = 1$ T. Fig. 1 shows three-dimensional models of finite element method mesh (*a*) and temperature distribution (*b*) in a rectangular-shaped gyrotropic thermoelement (the Ettingshausen thermoelement).

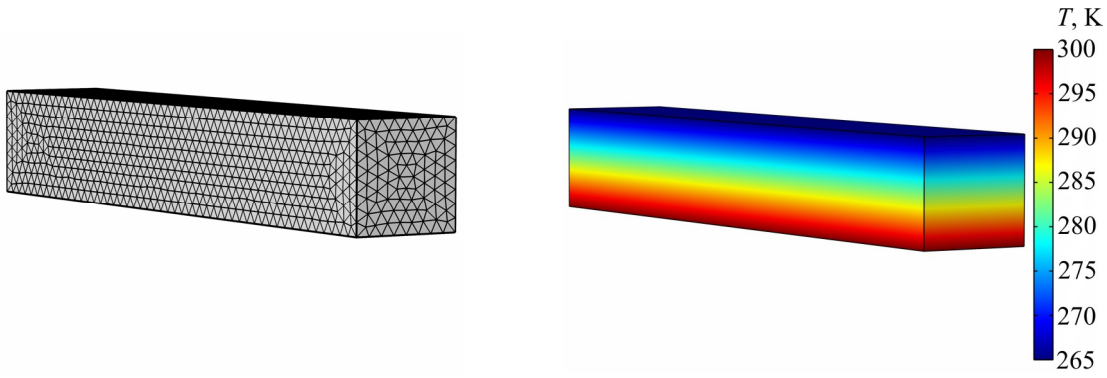

a) *b)*

Fig. 2. Three-dimensional models of finite element method mesh (a) and temperature distribution (b) in a rectangular-shaped gyrotropic thermoelement.

Fig. 3 presents three-dimensional models of finite element method mesh (*a*) and temperature distribution (*b*) in a spiral-shaped gyrotropic thermoelement. These thermoelements can be efficiently used for cooling cylinder-shaped objects.

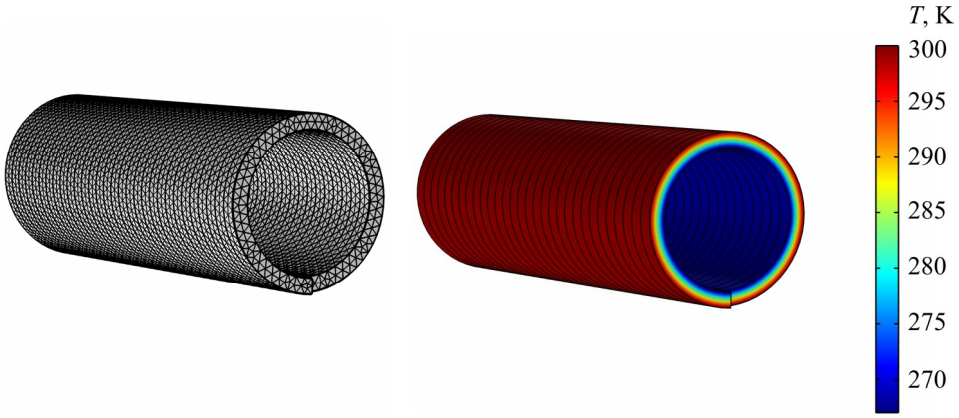

a) *b)*

Fig. 3. Three-dimensional models of finite element method mesh (a) and temperature distribution (b) in a spiral-shaped gyrotropic thermoelement.

Fig. 4 presents three-dimensional models of finite element method mesh (*a*) and temperature distribution (*b*) in optimal-shaped gyrotropic thermoelement.

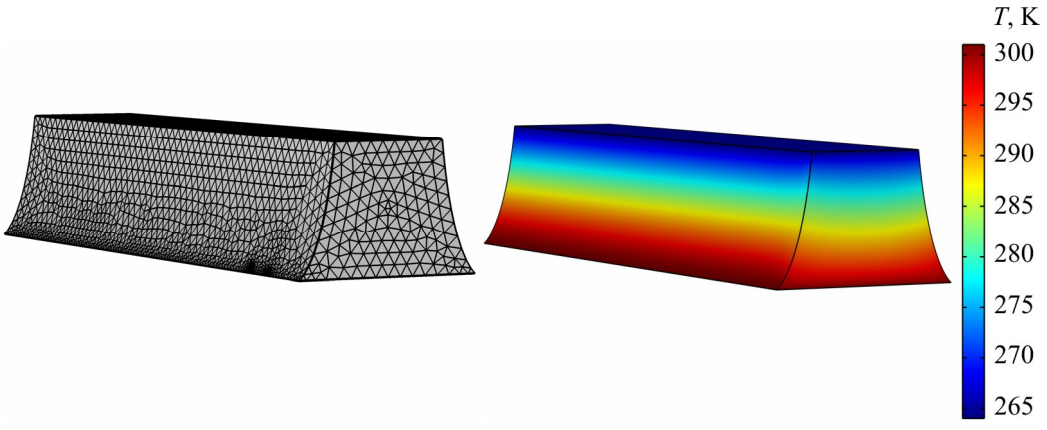

a) *b)*

Fig. 4. Three-dimensional models of finite element method mesh (a) and temperature distribution (b) in optimal-shaped gyrotropic thermoelement .

Using the data given in Fig. 1 the dependences of maximum temperature difference on the hot side temperature of thermoelement were obtained for *BiSb, Ag_2Te* and *InSb* (Fig. 5).

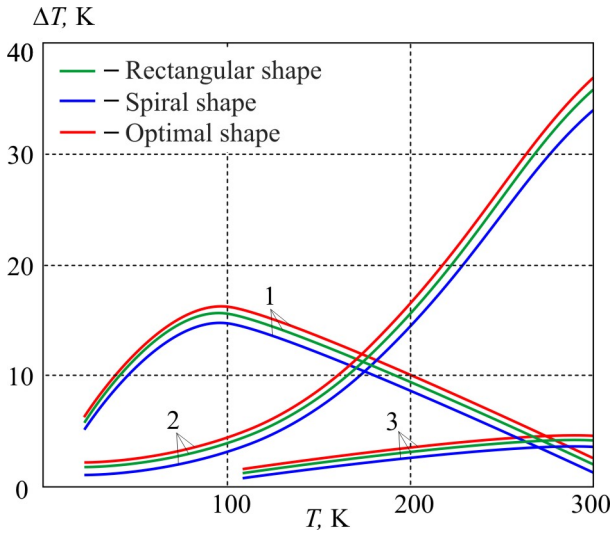

Fig. 5. ΔT_{max} shown as a function of T_1 (1 – BiSb, 2 – Ag_2Te, 3 – InSb).

It is seen that the use of Ag_2Te material in the temperature range of 200 – 300 K yields the highest values of ΔT_{max}, at $T_2 = 300$ K the value of $\Delta T_{max} \approx 36$ K. Hence, the use of Ag_2Te is more reasonable in this temperature range, and in the temperature range of 80 – 120 K it is better to use *BiSb* – $(\Delta T)_{max} \approx 17$ K. These materials can be used in the manufacture of gyrotropic thermoelements for medical instruments operated in cryogenic area.

Conclusions

1. The analytical and numerical methods were used to study the basic relations for the calculation of optimal characteristics of gyrotropic thermoelements in cooling mode. For the case of Ag_2Te material computer simulation was performed and temperature distributions in gyrotropic thermoelements of various shapes were obtained.
2. The temperature dependences of ΔT_{max} for gyrotropic thermoelements of various shapes were obtained. It was shown that the use of Ag_2Te is more reasonable in the temperature range of 150 – 300 K, when $(\Delta T)_{max} \approx 36$ K, and in the range of 80 – 120 K it is better to use *BiSb* – $(\Delta T)_{max} \approx 17$ K.

References

1. L.I.Anatychuk, *Thermoelements and Thermoelectric Devices. Reference Book* (Kyiv, Naukova Dumka, 1979), 766 p.
2. E.V.Osipov, N.I.Varich, and P.P.Mikitey, Study of the Ettingshausen effect in $Bi_{1-x}Sb_x$ Single Crystals, *Semiconductors* **5**(11), 2202 – 2204 (1971).
3. S.A.Aliev, M.I.Aliev, Z.F.Agaev, and D.G.Arasli, Material for Ettingshausen's Cooler, *Certificate of Authorship №828269*, 1981.
4. S.A.Aliev, E.I.Zulfigarov, *Thermomagnetic and Thermoelectric Effects in Science and Technology* (Baku, Elm Publ., 2009), 325 p.

5. A.G.Samoilovich, *Thermoelectric and Thermomagnetic Energy Conversion Methods* (Chernivtsi, Ruta, 2006), 226 p.
6. L.I.Anatychuk, *Thermoelectricity, Vol.2, Thermoelectric Power Converters* (Kyiv, Chernivtsi: Naukova Dumka, 2003), 386 p.
7. A.G.Samoilovich, L.L.Korenblit, Current Status of Theory of Thermoelectric and Thermomagnetic Effects in Semiconductors, *Advances in Physical Sciences* **49**(2), 243 – 272 (1953).
8. H.Nakamura, K.Ikeda, and S.Yamaguchi, Transport Coefficients of *InSb* in a Strong Magnetic Field, *Proc. of XVI-th International Conference on Thermoelectrics* (Dresden, Germany, 1997), P. 142 – 146.
9. L.I.Anatychuk, O.J.Luste, Ya.G.Fedoruk, and S.M.Shinkaruk, Eddy Thermoelectric Currents in Gyrotropic Medium with a Radial Temperature Distribution, *J.Thermoelectricity* 1, 19 – 24(2004).
10. O.J.Luste, Ya.G.Fedoruk, Gyrotropic Thermoelement in the Inhomogeneous Magnetic Field, *J.Thermoelectricity* 1, 16 – 22(2006).
11. O.J.Luste, Ya.G.Fedoruk, Optimization of Materials for Gyrotropic Thermoelements, *J.Thermoelectricity* 4, 21 – 26 (2008).
12. Z.F.Agaev, D.G.Arasli, and S.A.Aliev, Thermomagnetic Converter of Infra-Red Radiation, *Problemy Energetiki* 3, 12 – 21(2003).
13. S.A.Nemov, V.I.Proshin, G.L.Tarantasov, R.V.Parfenyev, D.V.Shamshur, and A.V.Chernyaev, Transverse Nernst-Ettingshausen Effect, Resonance Scattering and Superconductivity in *SnTe*: In, *Physics of the Solid State* **51**(1), 461 – 464 (2009).
14. T.G.Harman, J.M.Honig, *Thermoelectric and Thermomagnetic Effects and Applications* (New York, Mc. Graw – Hill, 1967), 377 p.
15. H.Nakamura, K.Ikeda, and S.Yamaguchi, Transport Coefficients of *InSb* in a Strong Magnetic Field, *Research Report. NIFS series, Nagoya, Japan (1998),* 23 p.
16. Hiroaki Nakamura, Kazuaki Ikeda, and Satarou Yamaguchi, Transport Coefficients of *InSb* in a Strong Magnetic Field, *Proc of XVI-th International Conference on Thermoelectrics* (Dresden. Germany, August 26 – 29, 1997), P. 142 – 146.
17. P.I.Baranskii, G.P.Haidar, Anisotropy of Thermoelectric Properties of Multi-Valley Semiconductors of Cubic Symmetry under the Influence of External Directional Effects, *J.Thermoelectricity* 1, 12 (2014).
18. H.J.Goldsmid, E.H.Volckmann, Galvanomagnetic and Thermoelectric Measurements on Polycrystalline $Bi_{88}Sb_{12}$, *Proc. of XVI-th International Conference on Thermoelectrics (Dresden, Germany, August 26 – 29, 1997),* P. 142 – 146.
19. L.I.Anatychuk, L.N.Vikhor, Low-Temperature Thermoelectric Cooling under Optimal Legs Inhomogeneity in the Optimal Nonuniform Magnetic Field, *Proc. of XVI-th International Conference on Thermoelectrics (Dresden, Germany, August 26 – 29, 1997),* P. 397 – 400.
20. COMSOL Multiphysics User's Guide (*COMSOLAB, 2010)*, 804 p.

Submitted 31.05.2016.

M.V. Maksimuk

M.V. Maksimuk

Institute of Thermoelectricity of the NAS and MES of Ukraine,
1, Nauky Str., Chernivtsi, 58029, Ukraine

COMPUTER DESIGN OF THERMOELECTRIC STARTING PRE-HEATER ON GAS FUEL

This paper presents the results of computer design of thermoelectric heater on gas fuel with electric power output 230 – 250 W for start heating of vehicle engines under low ambient temperatures.

Key words: internal combustion engine, starting pre-heater, thermoelectric generator, physical model, computer design.

Introduction

According to International Energy Agency, the number of automobiles in the world by 2015 had exceeded 1 milliard. 22.5 million of them use liquefied propane-butane as fuel. In Ukraine ~ 10 % of the automobile park, i.e. 800 thousand vehicles, are equipped with compressed natural gas equipment (GBO) of 3 and 4 generations. It is expected that within 2 – 3 years not less than 20 % of the park will be models that run on gas fuel [1].

Keen demand for such automobiles is caused by a number of advantages in the use of propane-butane as compared to petrol:

– higher octane number (112 for propane-butane, 80 – 98 for petrol) assuring reliable engine operation for all modes almost without detonation;

– reduced load on engine pistons;

– increased engine turnaround time by a factor of 1.5;

– increased engine oil service life by a factor of 1.5 – 2;

– reduced noise level with the engine running by 3 – 8 dB (at least twice);

– increased service life of spark plugs by 40 %;

– reduced level of toxic exhaust gases: *CO* – by a factor of 2 – 3, *NO* – by a factor of 1.2, *CH* – by a factor of 1.3 – 1.9.

One of the main disadvantages of using liquefied propane-butane as automobile fuel is a negative influence of low temperatures which results in formation and freezing of condensate in the reducer and pipes of GBO. As a result, the engine stalls, and to start it again is practically impossible. Moreover, icing of reducer decreases considerably the service life of its membranes.

To prevent from premature failure of reducer membranes and valves and in general to assure a reliable automobile start at low temperatures, the engine must be pre-heated.

Today the most efficient pre-heating method is autonomous start heating [2].

However, the main factor restricting the use of gas starting pre-heaters for automobiles equipped with GBO-3 and GBO-4 is operating instability and low reliability of gas system. In this case it is necessary to start and heat the engine on liquid fuel with a gradual transition to gas fuel, which, although saving fuel, neutralizes all advantages of start heating.

At the present time, new vistas in the use of gas starting pre-heaters are related to the use of automobiles of compressed natural gas equipment of "new generation" – GBO-5 and GBO-6. The distinctive feature of these developments lies in the fact that gas delivery to inlet manifold is done in the liquid, rather than the gas state, namely through special nozzles. So, these systems are of a completely new design. Thus, a reducer is substituted by pressure controller and gas fuel pump which pumps liquid gas directly to nozzles. As long as this design eliminates the need for evaporation of gas in the reducer, this enables one to start the engine at any low ambient temperatures.

With the advent of GBO-5 and GBO-6, models appeared in the market (Webasto LGW 300, Trumatic E2400-E4400) that run on propane-butane and provide start heating of gas-fuelled vehicles.

To avoid automobile battery discharge during start heating, it is reasonable to use thermoelectric generator as a power supply source [3 – 5].

In [6] it is shown that total electric power of thermal generator for starting pre-heaters of vehicles with engine displacement up to 4 l must be 70 – 90 W; for vehicles with engine displacement 4 – 10 l and more than 10 l – 130 – 150 W, 230 – 250 W, respectively. Such electric powers of thermal generators assure autonomous power supply to heater components and will allow additional battery charging and power supply to other automobile equipment.

In [7, 8], the construction, operating principle and results of computer design of thermoelectric automobile starting pre-heater on liquid fuel of electric power 70 – 90 W and 130 – 150 W are presented.

The purpose of this work is to design thermoelectric automobile starting pre-heater on liquefied gas fuel of electric power 230 – 250 W for start heating of engine under low ambient temperatures.

Design selection of thermoelectric starting pre-heater

As a source of heat, use was made of a gas burner (Fig. 1) of liquid starting pre-heater "Webasto LGW 300". With regard to burner design, the most rational shape of the hot heat exchanger in terms of efficient heat exchange with the source of heat is a cylinder pipe accommodating a burner in its internal space, and its external surface having the form of planes where thermoelectric modules are arranged.

The thermoelectric converter is composed of thermoelectric generator modules "ALTEC-1061" based on bismuth telluride which on arrival of the necessary amount of heat to the hot side and on achievement of optimal operating temperatures assure generation of the assigned electric power.

Fig. 1. Appearance of gas burner of liquid starting pre-heater "LGW 300" (Webasto) [9].

Fig. 2. Appearance of circulating pump of liquid starting pre-heater "LGW 300" (Webasto) [9].

Fig. 3 shows a three-dimensional graphical image of the dependence of electric power P' and efficiency η' on the hot side T_h and cold side T_c temperature of thermoelectric module "ALTEC-1061".

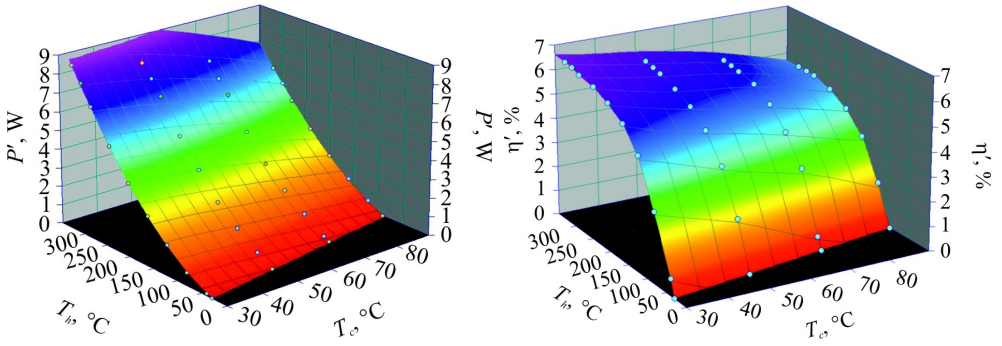

Fig. 3. Dependence of electric power P' (a) and efficiency η' (b)on the hot side T_h and cold side T_c temperature of thermoelectric module "ALTEC-1061" [10].

From the analysis of the data presented in Fig. 3 it follows that to provide the electric power output of the heater 230 – 250 W, it is necessary to have 32 modules "ALTEC-1061". From these considerations, the most efficient design of the hot heat exchanger is a regular octahedron, with 4 thermoelectric modules arranged on each side thereof. In so doing, the hot side temperature of the modules must be 280 – 330 °C, the cold side – 30 – 70 °C.

Taking into account that the efficiency of thermoelectric generators using single-stage modules based on bismuth telluride is 3 – 3.5 % [11], to assure the electric power output of the heater 230 – 250 W, it is necessary to spend ~ 6.6 – 7.2 kW of heat which corresponds to propane-butane consumption 510 – 550 g/h. It should also be stated that fuel delivery to the burner is done by a pump of GBO system, so in the design of gas heater, unlike the petrol and diesel analogs, there is no individual fuel pump, and consumption is controlled by changing nozzle holes.

As a circulating pump, the liquid pump (Fig. 2) of starting pre-heater "LGW 300" (Webasto) was used. This type of the pump is specially designed for pumping of heat carrier in transport means with engine displacement more than 10 l. Nominal supply voltage of the pump is 24 V, maximum heat carrier consumption is 5.2 m^3/h.

Physical model of thermoelectric starting pre-heater and its description

In [7] it is shown that for the calculation of the basic energy and design parameters of the heater it is convenient to use a physical model (Fig. 4) where the process of heat transfer from the source of heat to thermopile takes place as a result of gas flow passing through the hot heat exchanger at velocity v and temperature T_G.

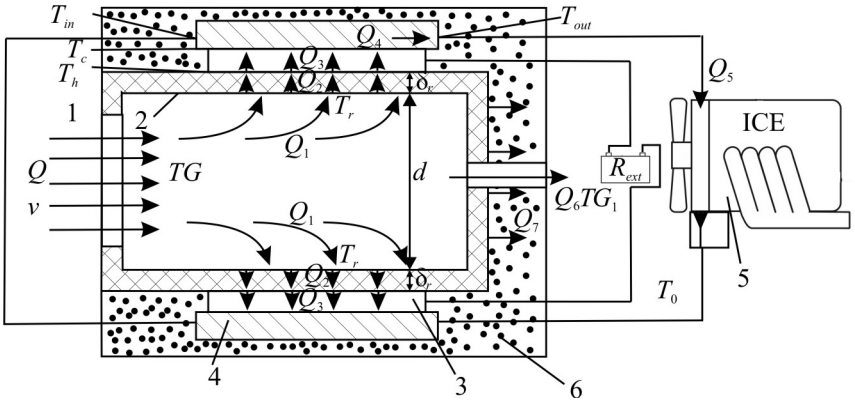

Fig. 4. Physical model of thermoelectric automobile heater: 1 – gas flow; 2 – hot heat exchanger; 3 – thermopile; 4 – cold heat exchanger; 5 – automobile engine; 6 – thermal insulation.

In so doing, the amount of heat Q released due to petrol combustion is used for heating of gases that formed as a result of complete fuel combustion:

$$g_n G_n = C_p (T_G - T_o), \quad (1)$$

where g_n and G_n are consumption and calorific power of petrol fuel, C_p is total heat capacity of gases (CO_2, H_2O, N_2 and air) that formed as a result of fuel combustion, T_0 is ambient temperature.

Heat Q_1 coming from the heated gases to the hot heat exchanger is transferred due to convection

$$Q_1 = \alpha(T_G - T_r)S_R, \quad (2)$$

where α is convective coefficient of heat transfer from the gas to the heat-absorbing surface of the hot heat exchanger;

T_r is the temperature of the heat-absorbing surface of the hot heat exchanger;

S_R is the area of the heat-absorbing surface of the hot heat exchanger.

Heat Q_2 is transferred due to thermal conductivity from the heat-absorbing surface of the hot heat exchanger to the hot side of thermopile:

$$Q_2 = \frac{S_r \lambda_r}{\delta_r}(T_r - T_h) \quad (3)$$

S_r is the area of the heat-releasing surface of the hot heat exchanger;

λ_r is the thermal conductivity of heat exchanger material;

δ_r is the thickness of heat exchanger base;

T_h is the hot side temperature of thermopile.

Useful heat Q_3 coming to thermoelectric modules was calculated from the power P' of one module with determined hot side T_h and cold side T_c temperatures of thermopile, its efficiency η' and the number of modules n:

$$Q_3(T_h, T_c) = n\frac{P'(T_h, T_c)}{\eta'(T_h, T_c)} \quad (4)$$

Heat Q_4 is removed from the cold side of thermopile by heat carrier flow circulating in the cold liquid heat exchanger 4:

$$Q_4 = g_t c_{pT}(T_{in} - T_{out}), \quad (5)$$

where g_t is heat carrier consumption c_{pT} is heat carrier heat capacity T_{in}, T_{out} are heat carrier temperatures at inlet to and outlet of thermopile cooling system, respectively.

As long as liquid heat exchangers are combined into one hydraulic loop with engine cooling system 5, the heat removed by heat carrier from the modules is spent on start heating of engine:

$$Q_5 = c_{eng} m_{eng}(T_{out} - T_0), \quad (6)$$

where c_{eng}, m_{eng} are the heat capacity and mass of automobile engine, respectively; T_0 is the ambient temperature.

Basic heat losses:

1) Q_6 – with reaction products (water H_2O, carbon dioxide CO_2 and nitrogen N_2):

$$Q_6 = C_c m_c (T_{G_1} - T_0), \quad (7)$$

where C_c is the average heat capacity of reaction products, m_c is the mass of reaction products, T_{G1} is the temperature of reaction products.

2) Q_7 – on thermal insulation:

$$Q_7 = \frac{\lambda S_{ph}}{L}(T_{termopile} - T_0), \tag{8}$$

where λ is the thermal conductivity of insulating material; S_{ph} is the area of the hot heat exchanger surface which is not occupied by thermopile; L is the thickness of thermal insulation layer.

Thus, heat balance equation for the selected model of thermoelectric automobile heater can be written as:

$$\begin{cases} Q = Q_1 + Q_6, \\ Q_1 = Q_2 + Q_7, \\ Q_2 = Q_3, \\ Q_3 - P = Q_4, \end{cases} \tag{9}$$

where P is output electric power of the heater.

Solving the system of heat balance equations (9) enables one to determine the basic energy and design parameters of thermoelectric automobile heater.

Computer design aimed at determining:

– gas temperature T_G in the hot heat exchanger and the effective area of the heat-absorbing surface of the hot heat exchanger S_R to assure on the hot side of the thermopile the temperature T_h = 280 – 330 °C.

– thermal power Q_5 removed by heat carrier to estimate pre-heating rate of automobile engine.

Calculation results

Calculation procedure of gas temperature T_G is described in detail in [7].

As a result of appropriate calculations, ratio (10) was obtained to determine air delivery velocity v to the hot heat exchanger as a function of temperature T_G:

$$v = 5\left[\frac{\frac{G_n}{T_G - T_0} - 20.29}{18.15} + 1\right] \cdot \frac{3.62\, g_n}{\rho_{T0} S_R}, \tag{10}$$

where 20.29 and 18.15 are coefficients that determine the content of carbon dioxide, water, nitrogen and air that formed as a result of complete combustion of propane-butane, 3.62 is coefficient that determines the amount of oxygen necessary for complete combustion of propane-butane, ρ_{T_0} is the density of air at given ambient temperature.

The Mathcad application software package was used to determine the inverse dependence of hot gas temperature T_G on air velocity v (Fig. 5) at G_n = 46.8 MJ/kg, g_n = 550 g/h, T_0 = 0 °C, $\rho_{T_0} = 1.29$ kg/m^3 and combustion chamber diameter d = 80 mm.

From the analysis of data in Fig. 5 it follows that for further calculations of the hot exchanger design it is not reasonable to use T_G < 300 °C and T_G > 500 °C: in the former case it is impossible to achieve the necessary hot side temperatures of module, in the latter case the rise in temperature leads to increase in the heat exchanger dimensions due to possible overheating of thermopile.

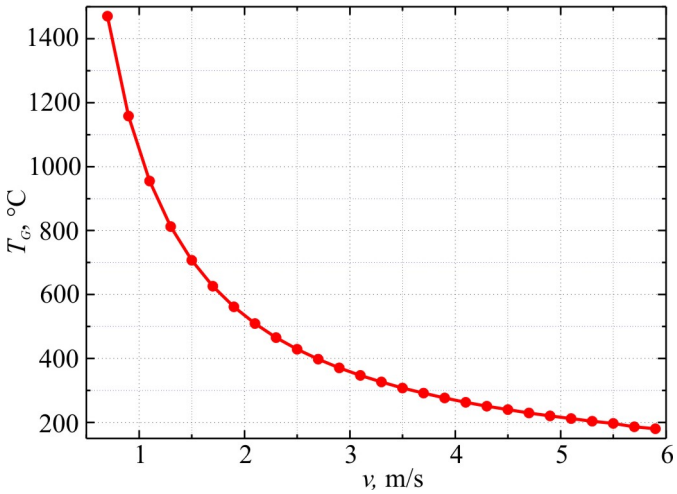

Fig. 5. Dependences of gas temperature T_G on air delivery velocity to the hot heat exchanger.

So, to determine the dependence of the module hot side temperature T_h on the area of the heat-absorbing surface, we used hot gas temperature $T_G = 300 – 500$ °C which corresponds to air velocities 2.1. – 3.5 m/s.

Simulation was done by finite element method with the use of "Comsol Multiphysics" application software package [12].

In the process of computer design the following values were used as the input data:

– the hot gas temperature T_G = (300; 400; 500) °C;

– the velocity of gas in the heat exchanger v = (3.5; 2.6; 2.1) m/s;

– the area of the heat-absorbing surface S_R = (0.05; 0.085; 0.115; 0.185) m^2;

– the thermal conductivity of the hot heat exchanger material λ_r = 140 W/m·K;

– the thermal resistance of thermoelectric module κ_m = 0.7 m·K/W.

In so doing, it was assumed that heat sinks are at the outlet of combustion products from the heat exchanger and at places of modules location, and thermal adiabatic insulation conditions are imposed on the rest of the boundaries.

Fig. 6 shows computer designed dependences of the module hot side temperature T_h on the area of the heat-absorbing surface S_R at hot gas temperature T_G within 300 – 500 °C.

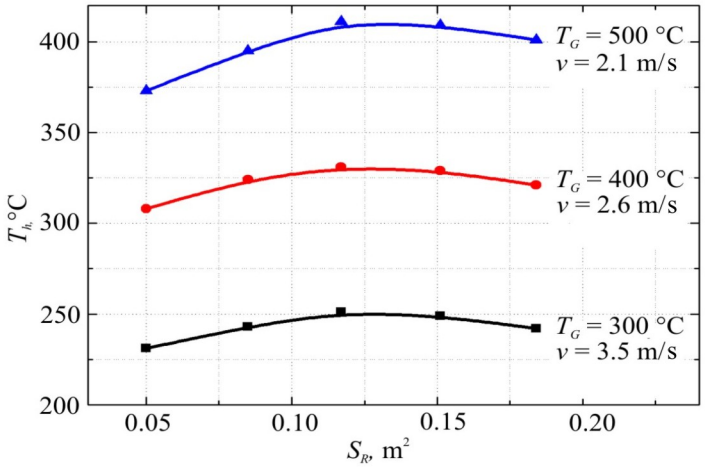

Fig. 6. Dependences of the module hot side temperature T_h on the area of the heat-absorbing surface S_R of heat exchanger.

From the data presented in Fig. 6 it is seen that the hot side temperature of module 330 °C is achieved at gas temperature T_G = 400 °C and the area of the heat-absorbing surface of the hot heat exchanger S_R = 0.12 m^2. Further increase in the number of channels on the internal surface of heat exchanger leads to creation of additional air resistances owing to which there is a drop in gas motion velocity and, hence, in the hot side temperature of thermopile.

Fig. 7 shows temperature distribution in the "hot heat exchanger-thermoelectric modules", Fig. 8 – the finite element method mesh.

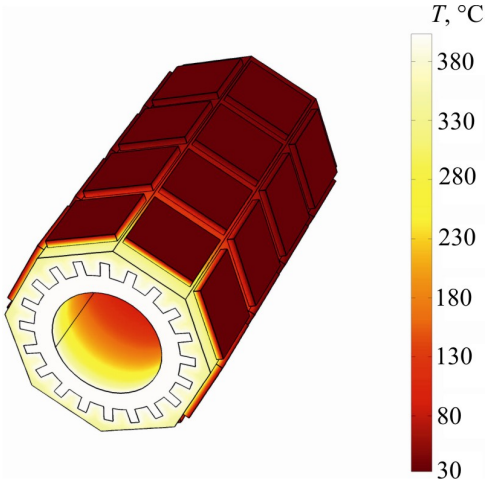

Fig. 7. Temperature distribution in the "hot heat exchanger – thermoelectric modules" system. T_G = 400 °C. S_R = 0.12 m^2.

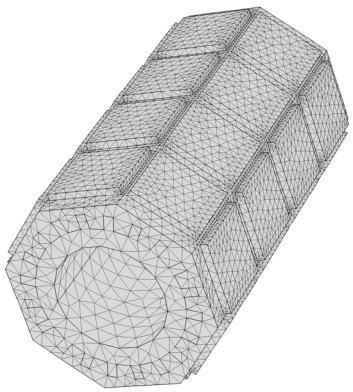

Fig. 8. Finite element method mesh.

As it follows from the analysis of temperature distribution, as the gases flow to heat sink, T_G is reduced, which results in the reduction of temperature T_h by ~ 200 °C. However, as long as in a real design the source of heat is directly in the heat exchanger, it can be considered that the hot side temperature of modules is identical.

Similar calculations to determine T_G at S_R = 0.12 m^2 and g_n = 510 g/h show that to assure the hot side thermopile temperature 280 °C, the temperature of hot gases in the heat exchanger must be 350 °C. In this case air delivery velocity must be 2.8 m/s.

For quick heating of automobile engine and the efficient operation of thermoelectric converter, it is necessary, on the one hand, to assure maximum transfer of thermal power from the modules to the cold heat carrier, on the other hand, to create such conditions whereby the difference in heat carrier temperature at the inlet to and outlet of heat exchangers would be minimal.

With this aim, the effective channel area of the cold heat exchangers and optimal consumption of liquid heat carrier were determined. The cold heat exchanger simulation was done by finite element method with the use of "Comsol Multiphysics" application software package.

In the process of computer design the following values were used as the input data:

– the temperature of cold heat carrier at inlet to cold heat exchanger T_{in} = 30 °C;

– total thermal power removed from the modules in operating mode Q_4 = 3.68 kW (115 W based on one module);

– heat carrier consumption (heat carrier – antifreeze) g_t = (1.6; 2.6; 3.6; 4.6; 5.2) m^3/h;

– channel area of the cold heat exchanger S_c = (55 – 300) cm^2;

– the thermal conductivity of cold heat exchanger material λ_{r1} = 105 W/m·K;

– heat carrier heat capacity c_{pT} = 3151 J/kg·K;

– heat carrier thermal conductivity $\lambda_T = 0.34$ W/m·K.

In the design, heat sink was assigned at points of heat carrier outlet from the heat exchanger, and adiabatic thermal insulation conditions were imposed at the rest of the boundaries.

Fig. 9 shows a dependence of thermal power Q_5 removed from thermoelectric modules to automobile engine on the total area of channels S_c of the cold heat exchangers with different heat carrier consumption.

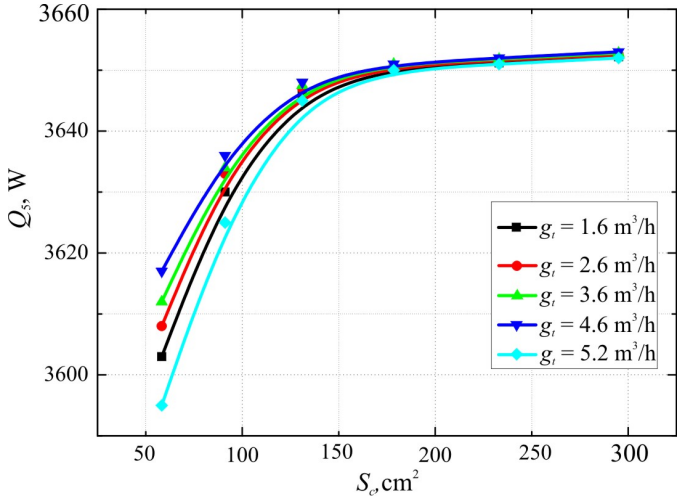

Fig. 9. Dependences of thermal power Q_5 on the channel area S_c of the cold heat exchangers.

From the analysis of data represented in Fig. 9 it follows that for complete transfer of thermal power from the modules to the engine the area of channels in the cold heat exchangers must be at least 170 cm^2. With such channel area Q_5 is practically independent of heat carrier consumption, which in turn allows reducing the losses of the output electric power of the heater on power supply to circulation pump.

Moreover, as is seen from Fig. 10, at S_c = 40 cm^2 heat carrier consumption has no essential effect on the difference in heat carrier temperature at the inlet to and outlet of cold heat exchangers ($\Delta T = 1 – 2$ °C). So, the choice of optimal g_t will be determined only by engine displacement and automobile cooling circuit.

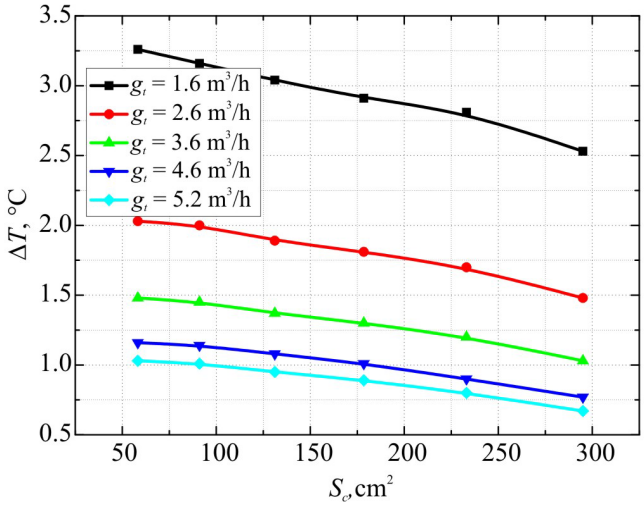

Fig. 10. Dependences of heat carrier temperature difference ΔT between the inlet to and outlet of the cold heat exchangers on the channel area S_c.

Fig. 11 and 12 show the finite element method mesh and temperature distribution for the cold heat exchanger.

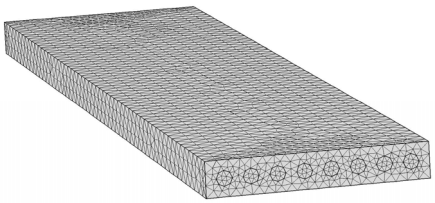

Fig. 11. Finite element method mesh.

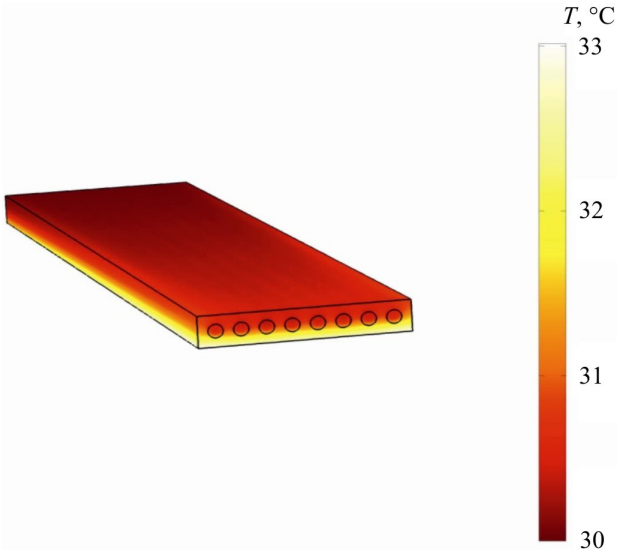

Fig. 12. Temperature distribution in the cold heat exchanger. S_c = 170 cm^2, g_t = 5.2 m^3/h.

Start heating of the engine of displacement more than 10 l (modern 8 – 12 cylinder internal combustion engines), heat capacity 0.462 kJ(kg K) from 0 °C to 30 °C will require ~ 13.9 MJ of thermal energy. Taking into account that total thermal power removed from the thermopile by heat carrier with temperature 30 – 70 °C is ~ 3.65 kW (Fig. 13), start heating of such engine will require ~ 1 hour.

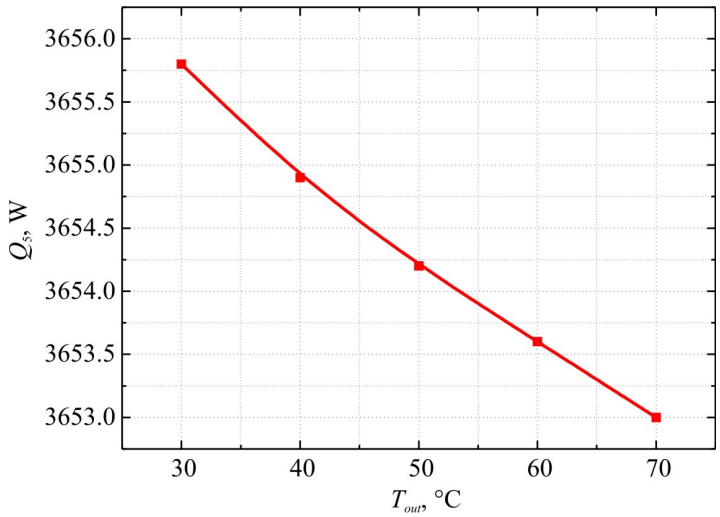

Fig. 13. Dependences of thermal power Q_5 removed by heat carrier on heat carrier temperature T_{out} at the outlet of the cold heat exchangers.

Under real conditions the time of engine heating will be somewhat longer which is related to heat losses due to engine heat exchange with the environment, losses of heat transfer along cooling circuit, as well as due to the availability of hydraulic resistances in the "heater-engine" system.

Conclusions

1. It was established that the electric power output of the heater 230 – 250 W is attained through use of 32 modules "ALTEC-1061" with the hot and cold side temperatures 280 – 330 °C and 30 –70 °C,

respectively. With the heater efficiency 3 – 3.5 %, to attain such electric power, it is necessary to spend ~ 7.2 – 6.6 kW of heat, which corresponds to fuel consumption 510 – 550 g/hour.

2. It was shown that the necessary temperature level on the hot side of thermopile 280 – 330 ºC is attained at gas temperature in the hot heat exchanger in the range of 350 – 400 °C, the velocity of air delivery to combustion chamber 2.6 – 2.8 m/s and the area of the heat-absorbing surface of the hot heat exchanger 0.12 m^2.
3. It was established that total thermal power transferred from the thermopile of the heater to heat carrier of the engine is ~ 3.65 kW. At heat carrier temperature 30 – 70 °C the start heating of engines of displacement more than 10 l from 0 °C to 30 °C will require ~ 60 min.

The author would like to express his gratitude to academician L.I. Anatychuk for the subject and the idea of the research and to junior research fellow R.M. Mochernyuk for the helpful advice on computer simulation.

References

1. https://www.iea.org.
2. V.S.Naiman, *All about Starting Pre-Heaters* (Moscow: ACT, 2007), p. 213.
3. V.Ya.Mykhailovsky, M.V.Maksimuk, Automobile Operating Conditions at Low Temperatures. The Necessity of Applying Heaters and the Rationality of Using Thermal Generators for their Work, *J.Thermoelectricity* 3, 18 – 27 (2015).
4. Patent (UA) № 72304 InCl: F01N 5/00; H01L35/00 Automobile Heater with Thermoelectric Power Supply / L.I.Anatychuk, V.Ya.Mykhailovsky. – Publ. 10.08.2012, Bul. № 15, Appl. u 2012 02055 of 23.02.2012.
5. Patent (UA) №89039 InCl F02M 1/00 System of Power Supply and Heating of Gas Internal Combustion Engine / L.I.Anatychuk, V.Ya.Mykhailovsky, M.V.Maksimuk. – Publ. 10.04.2014, Bul. № 7, Appl. u 2013 12585 of 28.10.2013.
6. V.Ya.Mykhailovsky, M.V.Maksimuk, Rational Powers of Thermal Generators for Starting Pre-Heaters of Vehicles, *J.Thermoelectricity* 4, 66 – 72 (2015).
7. V.Ya.Mykhailovsky, V.V.Maksimuk, Computer Design of Thermoelectric Automobile Starting Pre-Heater Operated with Diesel Fuel, J.Thermoelectricity 1, 50 – 63 (2016).
8. M.V.Maksimuk, Computer Design of Thermoelectric Automobile Starting Pre-Heater Operated with Petrol Fuel, J.Thermoelectricity 2, 49 – 58 (2016).
9. http://www.webasto.com/ua.
10. http://www.inst.cv.ua.
11. L.I.Anatychuk, V.Ya.Mykhailovsky, Two-Sectional Gas-Fuelled Thermoelectric Generator, *J.Thermoelectricity* 1, 76 – 86 (2008).
12. www.comsol.com.

Submitted 23.05.2016.

V.Yu. Lutsenko

V.Yu. Lutsenko[1], A.S. Zhagrov[2]

[1]Kyiv National University of Construction and Architecture, 31, Povitroflotsky Av., Kyiv, 03680 Ukraine;
[2]Zaporizhia State Engineering Academy, 226, Lenin Av., Zaporizhia, 69006 Ukraine

A.S. Zhagrov

EXPERIMENTAL INVESTIGATION OF PERIODIC TRANSIENT MODE OF THERMOELECTRIC GENERATOR

This paper presents a measuring installation and proposes a new method for experimental investigation of periodic transient mode of thermoelectric generator. It is shown that the use of periodic transient mode of thermoelectric generator allows increasing considerably the generated power as compared to steady-state mode. The value of optimal frequency of changing the external thermal fluxes is determined and a qualitative explanation of the effect of generated power increase is given.

Key words: thermoelectricity, thermoelectric generator, direct energy conversion, transient mode, heat recovery.

Introduction

The advent of new materials, improvement of their fabrication techniques, ecological and energy problems in recent several years have lead to growing interest in problems of thermoelectricity. Thermoelectric devices (generators and coolers) allow converting thermal into electric energy and vice versa. The possibility of using these devices for "thermal waste" recovery, the absence of mechanical parts and poisonous coolants, low inertia and small dimensions indicate the viability of this development. However, low efficiency of thermoelectric devices restricts their wide application.

The efficiency of thermoelectric device can be temporarily improved in its unsteady-state modes. For instance, pulse cooling mode allows reaching at certain points a deeper cooling which is accounted for by a considerable difference in time constants of electrical and thermal processes occurring in thermoelectric cooler. Pulse cooling theory was developed in [1 – 3] where the authors point to the absence of opportunity to increase the efficiency for transient modes as compared to steady-state mode.

However, recent investigations of periodic steady-state modes of thermoelectric devices substantiate their appropriateness and promising outlook [4 – 6]. In [4], two modes of thermoelectric device are analyzed – periodic switching mode (*P*-mode) and continuous sinusoidal mode (*S*-mode). The specific feature of *P*-mode is periodic instantaneous reversing the temperature of the hot and cold ends of thermoelectric conductor, whereas in *S*-mode the temperature of junctions is continuously changed harmonically. In the course of theoretical treatment the authors prove the possibility of increasing parameter ZT (Z is thermoelectric figure of merit; T is absolute temperature) which determines the efficiency of thermoelectric device by 30 % for cooling in S-mode, whereas such ZT growth for electric energy generation modes is not expected. The last conclusion, most

probably, results from the authors' assumptions in the framework of which the temperature of junctions and, accordingly, thermoEMF in P-mode are changed instantly, without regard to their thermal inertia.

In [6], a more universal model is proposed, wherein heat enters a TEG and leaves it through the plates. The numerical analysis made by the authors shows a maximum on the time dependence of generated thermoEMF the presence of which was later proved by them experimentally. Despite the fact that the mode in question was not periodic, the paper suggests its possible efficiency.

The *present paper* gives the results of experimental investigation of periodic transient modes of thermoelectric generators based on the module TEC112703. Later sections describe experimental installation, experimental procedure and the resulting data. The last section deals with discussion of the results and conclusions.

Measuring installation and experimental procedure

Experimental installation comprises three thermoelectric modules M1-M3 (Fig. 1). Modules M1 and M3 (TEC1-12708) are used as a heater and a cooler. Direct electric current is passed through these modules from the external source. If this current is positive, the surface of module M3 in contact with module M2 is heated. At the same time, the surface of module M1 in contact with module M2 is cooled. In this case module M3 can be regarded as a heater and module M1 is a cooler.

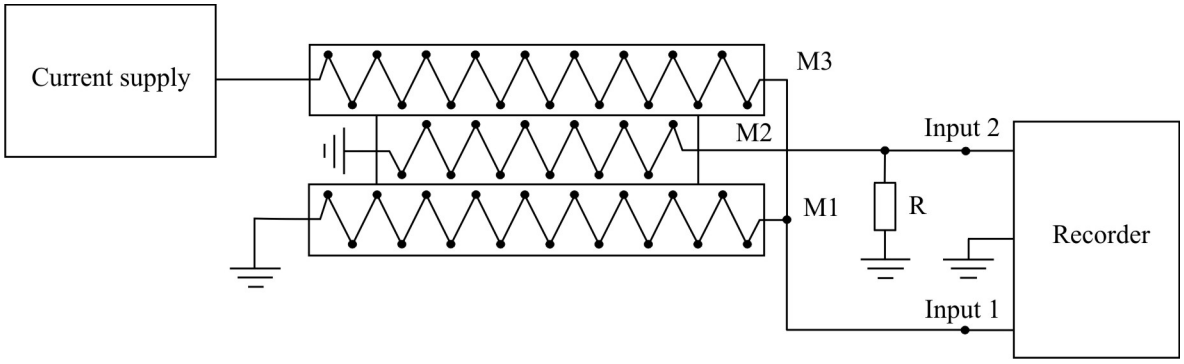

Fig. 1. Structural scheme of experimental installation.

With a change in external current direction, the heater and the cooler swap places. In this case the surface of module M3 in contact with module M2 is cooled, whereas the surface of module M1 in contact with module M2 is heated. Module M2 (TEC112703) works in the mode of generation of electric power which is released on load resistance *R*.

The voltage on module M1 is a sum of the voltage on the internal resistance of module R_{M1} denoted by U_{M1} and thermoEMF ε_{M1} developed by the module. The value $(U_{M1}+\varepsilon_{M1})$ is measured on input 1 of the recorder.

The voltage on load resistance R denoted by U_R is recorded on input 2. This voltage is the difference between thermoEMF ε_{M2} on module M2 and the voltage due to thermal current flow:

$$U_R = \varepsilon_{M2} - I_{TH2} R_{M2},$$

where I_{TH2} is thermal current of thermoelectric generator;

R_{M2} is internal resistance of module M2.

External current through modules M1 and M2 is periodic with a period T. During time $\frac{T}{2}$ there is direct current flow of one direction, then current is reversed, but its value remains the same.

This periodically reversing current, flowing through modules M1 and M3, causes the appearance on device inputs 1 and 2 of alternating periodic voltages recorded by the device.

The device operates as follows.

The signal on input 1 is recorded during 0.04 s. Then during the same time interval signal recording takes place on input 2, and so on. Thus, on each of device inputs signal recording takes place every 0.08 s, so signals on inputs 1 and 2 are shifted in time by 0.04 s.

Discussion of results

Fig. 2 shows one period of signal $(U_{M1}+\varepsilon_{M1})$ for different values of load resistance R (R = 20 Ω, 10 Ω, 5 Ω, 2.2 Ω and 1 Ω). The value of external current through modules M1 and M3 was 0.8 A, and the period T – 327.68 s.

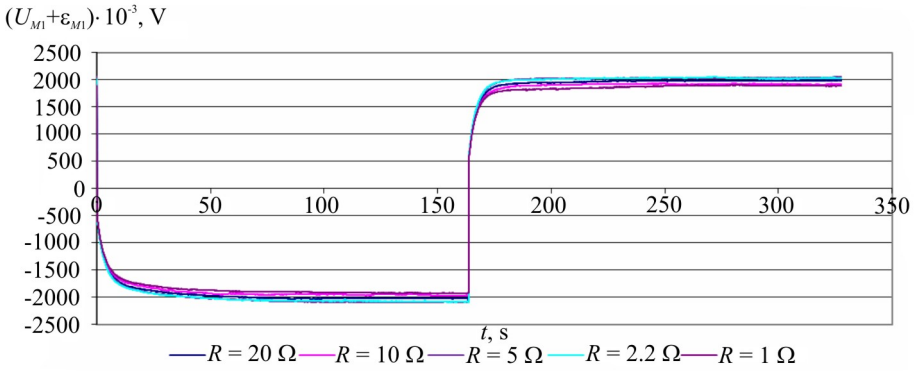

Fig. 2. Signals $(U_{M1}+\varepsilon_{M1})$ for 5 values of load resistance.

From Fig. 2 it follows that a change in the load resistance in the range of 1 ÷ 20 Ω produces a minimum effect on the signal $(U_{M1}+\varepsilon_{M1})$. The latter fact points to a marginal impact of change in the heater and cooler's thermal load in the capacity of which acts thermal generator M2.

Fig. 3 represents one period of signal U_R for the same values of load resistance, current through modules M1 and M3 and period.

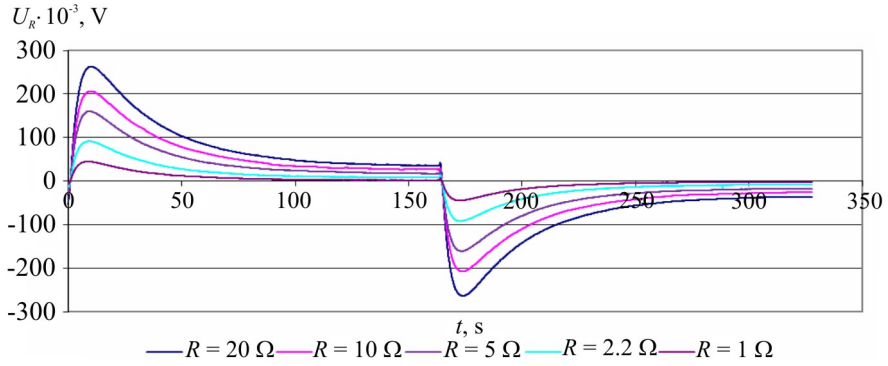

Fig. 3 Signals U_R for 5 values of resistance.

Note that with a rather large time of flow of direct current of the same direction (not less than 5 min) a steady-state value of voltage is set on the load resistance *R*. The results of measuring steady-

state values of voltage U_R with different load values for the positive $(U_{ST(+)})$ and negative $(U_{ST(-)})$ direction of external current are represented in Table 1. Also, Table 1 represents the results of calculation of power P_{ST} generated by thermoelectric generator in the steady-state mode by the formula:

$$P_{ST} = \frac{< U_{ST} >^2}{R}$$

where $< U_{ST} >$ are average values of steady-state voltages calculated by the values $U_{ST(+)}$ and $U_{ST(-)}$.

Table 1

Operating characteristics of thermoelectric generator (steady-state mode)

R, Ω	20	10	5	2.2	1
$U_{ST(+)}$, mV	32.545	24.875	17.055	7.351	1.454
$U_{ST(-)}$, mV	-32.526	-24.884	-17.073	-7.363	-1.465
$<U_{ST}>$, mV	32.54	24.88	17.06	7.36	1.46
P_{ST}, μW	52.93	61.90	58.24	24.60	2.13

The specific feature of thermoelectric generator transient mode is the presence of a maximum on the time dependence of output voltage. For signals represented in Fig. 3 the average power in the period T which is generated by thermoelectric generator can be calculated by the formula

$$P_{TR} = \frac{\int_0^T \frac{U_R^2}{R} dt}{T}.$$

The results of such calculation are presented in Table 2 and correspond to current through modules M1 and M3 equal to 0.8 A and the period of 327.68 s.

Table 2

Operating characteristics of thermoelectricgenerator (periodic transient mode)

R, Ω	20	10	5	2.2	1
P_{TR}, μW	630.16	755.54	838.38	567.44	269.47

The data given in Tables 1 and 2 testify to the presence of maximum useful electric power both for the steady-state and periodic transient modes with a well-defined load resistance close to 5 Ω.

A dependence of average in the period useful power P_{TR} on the period value was experimentally studied for T = 20.48 s, 40.96 s, 81.92 s, 163.84 s, 327.68 s. Fig. 4 represents a dependence of useful power on the period for load resistance R equal to 5 Ω and external current 0.8 A.

Analysis of the resulting experimental dependence of power generated by thermoelectric generator proves the availability of optimal value of generator operation period. In our case

maximum power P_{TR} ($P_{TR} = 1704.43 \cdot 10^{-6}$ W) corresponds to period $T = 81.92$ s. Note that in the steady-state mode with the same temperature conditions on the heater and the cooler the value of generated power P_{ST} is $58.24 \cdot 10^{-6}$ W.

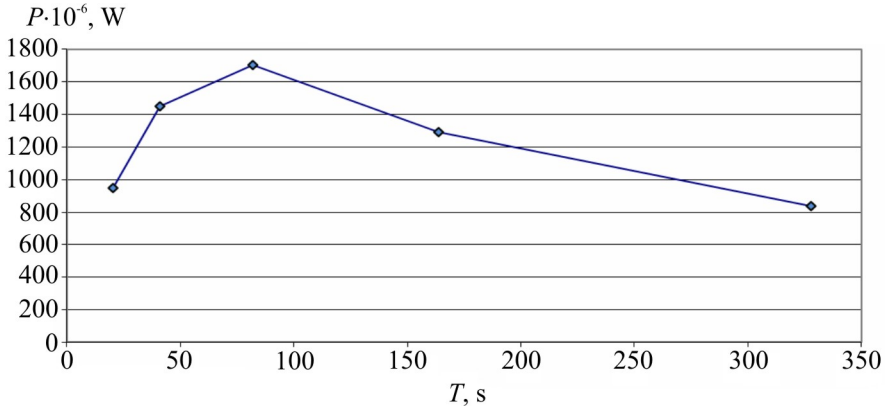

Fig. 4. Average power versus period.

Fig. 5 represents time dependence of signal U_R in maximum power generation mode. The value of external current through modules M1 and M3 was 0.8 A, period T – 82.92 s, load resistance R – 5 Ω. Also, this figure shows the values of steady-state voltages U_R for the negative $(U_{ST(-)})$ and positive $(U_{ST(+)})$ current directions through modules M1 and M3.

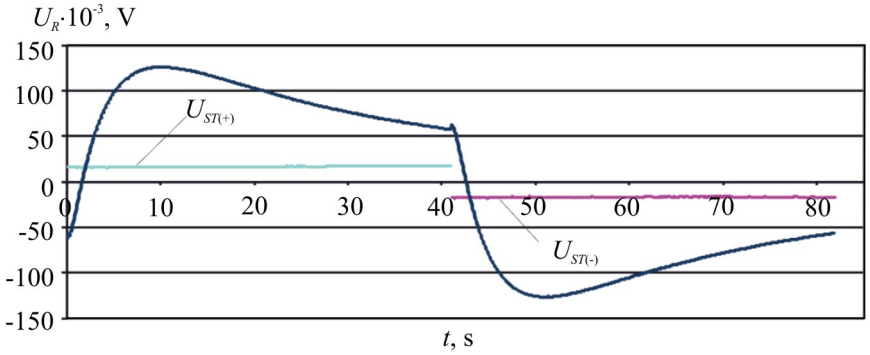

Fig. 5. Signals U_R in periodic transient and steady-state modes.

Thus, comparing powers generated by thermoelectric generator in the steady-state and periodic transient modes, it can be argued that the use of periodic transient mode leads to increase in power ($\frac{P_{TR}}{P_{ST}}$) by a factor of ~ 29.

When thermoelectric generator operates in the steady-state mode, its thermal resistance is low. It is due to considerable heat losses inside the generator, namely the heat from the hot module side passes to the cold side.

With a drastic change in the direction of heat fluxes, the thermal resistance of module is considerably increased for some time. Physically, it means that heat losses are reduced, and the heat that comes to the junctions of semiconductor thermocouples from the heater, heats the junctions to much higher temperature compared to the steady-state mode.

Similarly, a reduction of thermal energy losses due to thermal conductivity inside the module leads to the fact that cold junctions are cooled to considerably lower temperature compared to the

steady-state mode. The appearance of additional temperature difference between the hot and cold junctions determines the appearance of a maximum in the output voltage of thermoelectric generator.

The average in the period thermoEMF value in transient mode is $85.26 \cdot 10^{-3}$ V, whereas in the steady-state mode thermoEMF does not exceed $17.06 \cdot 10^{-3}$ V. Comparing these thermoEMF values it can be supposed that in transient mode the effective value of thermal conductivity is reduced by a factor of about 5, thus assuring a proportional reduction of thermal losses due to thermal conductivity inside the module.

This qualitative explanation gives an insight to the appearance of a maximum in the output signal of thermoelectric generator and possible increase of its generated power.

Conclusions

Experimental investigation of transient mode of thermoelectric generator has proved the possibility of considerable improvement of thermal into electric energy conversion as compared to steady-state conversion method. Transition to periodic transient mode of thermoelectric generator will make possible the increase of generated power by a factor of 20 and more.

The increase in the operating efficiency of thermoelectric generator when passing to the unsteady-state mode is based on the appearance of a maximum in its output voltage, which is accounted for by short-term, about 20 s, increase in generator thermal resistance. On expiry of this time, thermal resistance is reduced and steady-state generation mode is restored. The appearance in transient mode of the time dependence of generator thermal resistance indicates the need for determination of optimal generator period in terms of maximum power generation. The task of determination of optimal velocity of change in the external thermal fluxes requires separate consideration. In the course of preliminary investigation it was established that with decreasing velocity of current buildup through modules M1 and M3 with its reversal, the effect of maximum appearance in the output voltage of generator is reduced and eventually disappears.

Our investigation testifies to reduction of thermal losses due to thermal conductivity inside the module. Thus, one can expect certain efficiency increase of generators working in transient mode.

The obtained results point to promising outlook for further research and the necessity of transition to a real heater and cooler. In such systems, one will be able to change mechanically the direction of thermal fluxes in thermoelectric generator, for instance, the generator will be cylinder-shaped and periodically rotate by 180 degrees between the heater and cooler having semi-cylindrical cavities. One possible variant of such TEG is represented in Fig. 6.

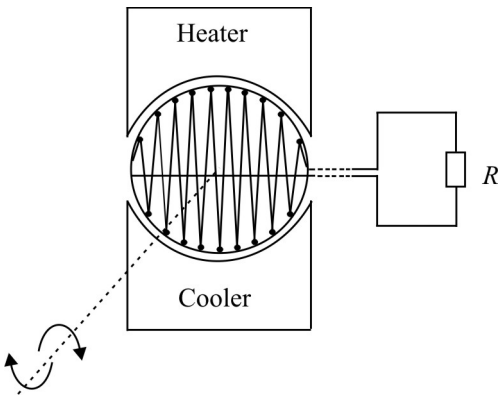

Fig. 6. Schematic of TEG working in pulse transient mode.

It should be noted that the experiment considered in this paper was performed with a slight temperature difference of the order of unit degrees. Assuming that when performing the experiment

on a real and sufficiently powerful TEG the above peculiarity (the availability of a maximum on time dependence of thermoEMF) is retained, in this case one can expect considerable increase of power produced. Naturally, in this case we are not talking about a real reduction of TEG thermal conductivity. One can only say that as a result of periodic reversal of thermal fluxes inside TEG due to thermal inertia the amount of heat passing from the hot to cold junctions is considerably reduced.

Formally, it can be said that periodic transient mode of TEG proposed here can essentially improve TEG performance, therefore one can expect the increase of both efficiency and the useful power produced.

References

1. E.K.Iordanishvili, V.P.Babin, *Unsteady-State Processes in Thermoelectric and Thermomagnetic Energy Conversion Systems* (Moscow: Nauka, 1983), 216 p.
2. A.F.Ioffe, L.S.Stilbans, E.K.Iordanishvili, and T.S.Stavitskaya, Thermoelectric Cooling (Moscow: USSR Acad. Sci., 1956).
3. E.K.Iordanishvili, Thermoelectric Power Supplies (Moscow: Sov. Radio, 1968).
4. A.A. Snarskii, I.V. Bezsudnov, Rotating Thermoelectric Device in Periodic Steady State, *Energy Conver* 94, 103 – 111 (2015).
5. Ming Ma, Jianlin Yu, and Jiaheng Chen, An Investigation on Thermoelectric Coolers Operated with Continuous Current Pulses, *Energy Conver* 98: 275 – 281 (2015).
6. Nguyen Q. Nguyen, Kishore V. Pochiraju, Behavior of Thermoelectric Generators Exposed to Transient Heat, *Applied Thermal Engineering* 51, 1 – 9 (2013).

Submitted 30.06.2016.

V.O. Dudal

Institute of Thermoelectricity of the NAS and MES of Ukraine,
1, Nauky Str., Chernivtsi, 58029, Ukraine

V.O. Dudal

ULTIMATE POTENTIAL OF UNDERGROUND THERMOELECTRIC GENERATORS

Computer model was created for the determination of temperature distribution in soil with a dynamic effect on the Earth surface of solar radiation thermal power. Temperature distributions in sandy soil for different geographic coordinates were obtained. Specific electric power of underground thermoelectric generator using temperature difference in soil which can be obtained throughout the year and on a monthly basis in different geographic coordinates was determined.
Key words: temperature distribution in soil, underground thermoelectric generator, specific electric power.

Introduction

General characterization of the problem. Underground electric energy sources are attractive for autonomous power supply to low-power devices. First of all it concerns remote and hard-to-reach areas where maintenance of special equipment is complicated. Despite very low electric powers, such energy sources may become indispensable for power supply to special-purpose equipment, protective and guard systems, electronic devices of autonomous weather stations, etc. They offer the advantage of being hidden from unauthorized persons that may affect their performance capability or render them inoperable. They do not feel a significant impact of weather conditions, which makes underground energy sources more attractive as compared to photoelectric.

Underground thermoelectric generators [1 – 6] are promising low-power energy sources which use thermal processes occurring in soils and on their surface as a source of heat.

The main indicator of soil thermal state is its temperature which is determined by solar energy input and the thermal properties of soil itself. The key thermal processes, as noted in [2], take place in the near-surface soil layer.

Soil temperature is a dynamic value which changes at different depths of soil profile in different periods of time. It is characterized by daily and annual periodicity [7, 8]. With depth, the amplitude of temperature variation is reduced and the diurnal dynamics at the depth of 50 cm decays almost completely. Annual variation, just as diurnal, is related to the input and consumption of heat and is mainly governed by radiation factors. Most frequently, the annual variation of soil temperature is tracked by its mean monthly values.

In the northern hemisphere maximal mean monthly temperatures of soil surface are observed in July-August, when heat input is the greatest, and minimal – in January-February. The difference between maximal and minimal mean monthly temperature throughout the year is called the amplitude of annual variation and it depends most of all on geographic latitude. The annual temperature mode of soils has large vibration amplitude and is expressed to a greater depth than diurnal one.

In [9], the laws of thermal processes occurring in soils were analyzed for evaluating the

efficiency of underground thermoelectric generators. The resulting temperature distributions in different types of soil at different geographic latitudes made it possible to determine maximum possible specific electric powers of underground thermoelectric generator.

The purpose of this paper is to obtain temperature distributions in sandy soil in different geographic coordinates (latitude, longitude) and to determine specific electric power of underground thermoelectric generator which can be obtained throughout the year and on a monthly basis.

Problem formulation and its solution

To obtain temperature distribution in soil, a physical model of soil area shown in Fig. 1 was considered.

The model considers thermal processes in soil with a dynamic effect on its surface of solar radiation thermal power $q_s(t)$ (W/m^2) within 24 hours. The properties of soil are characterized by the values of its heat capacity C_p, density ρ and thermal conductivity κ.

The model takes into account the diurnal variation of ambient temperature $T_{amb}(t)$, heat exchange between soil area with the environment due to heat transfer, convection and radiation. At certain depth l the temperature of soil T_0 is considered constant.

The sought-for values are temperature distribution in soil $T(t,z)$ and heat flux density $q(t)$ versus depth z and the time of day t.

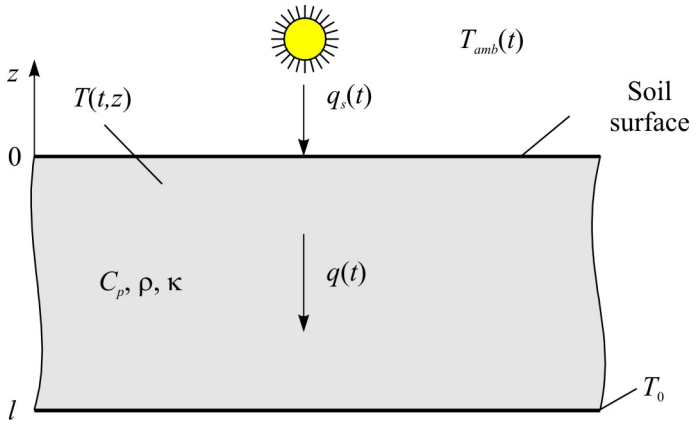

Fig. 1. Physical model of soil area.

Temperature distribution in soil stratum is described by the nonstationary Fourier's law:

$$\rho C_p \frac{dT}{dt} + \nabla\left(-\kappa \nabla T\right) = 0\,. \tag{1}$$

Convective heat exchange on the soil surface is described by equation

$$-\vec{n}\vec{q} = q_0\,, \tag{2}$$

where $\vec{n}$ is normal to soil surface, $\vec{q}$ is heat flux through soil surface, q_0 is heat flux from soil surface due to convection:

$$q_0 = h\left(T_{amb} - T\right), \tag{3}$$

where h is coefficient of convection.

Radiation from the soil surface is described by the Stephan-Boltzmann law

$$q_r = \sigma\varepsilon\left(T_{amb}^4 - T^4\right), \quad (4)$$

where σ is the Stephan-Boltzmann constant, ε is surface emissivity factor.

The boundary conditions for Eq. (1) – (4) are:

– at $z = 0$ thermal flux on the soil surface $q = (1 - k_s)q_s(t)$, where k_s is soil albedo, $q_s(t)$ is solar radiation thermal power [10];

– at $z = l$, $T = T_0$.

Computer model for solving Eq. (1) – (4) was created in Comsol Multiphysics environment [10]. Calculation of temperature distribution in soil was done by the finite element method the essence of which is that the object under study is broken up into a large number of elements, and in each of them the value of function is sought for which satisfies given second-order differential equations with the respective boundary conditions. The accuracy of solving the formulated problem depends on the level of breaking up and is assured by using a large number of finite elements.

The formulated problem was solved with the use of heat transfer with surface-to-surface radiation computer module, which is intended for simulation of heat transfer processes due to thermal conductivity, convection and radiation. The position of the Sun and its power were assigned in the external radiation source module with indication of geographic coordinates of object under study, the date and time of investigation.

Ambient temperature $T_{amb}(t)$ was assigned as the function of time according to averaged data of climatological observations within 2015 [11] for geographical points of various latitudes. Table 1 lists the cities with corresponding geographic coordinates that were selected for investigation.

In the model, the temperature of soil at the depth of 2 m is considered to be constant and equal to + 7 °C [8]. Calculations were performed for one day of each month in the year (the 15 th).

Table 1

Geographical coordinates of points under investigation and cities for which the data of climatological observations were taken

Point №	Latitude, degree		Longitude, degree		Time zone, UTC	City	Country
	North	South	West	East			
1	2	3	4	5	6	7	8
1.	60		150		-9	Seward	USA
2.	60		120		-7	Edmonton	Canada
3.	30		90		-6	New Orleans	USA
4.	0		60		-3	Boa Vista	Brazil
5.		30	60		-3	Reconquista	Arhentina
6.	30			0	+0	Adrar	Algeria
7.	60			30	+3	Saint-Petersburg	Russian Federation
8.	30			30	+2	Cairo	Egypt
9.		0		30	+3	Kampala	Uganda

Table 1 continued

1	2	3	4	5	6	7	8
10.		30		30	+2	Durban	SAR
11.	60			60	+5	Perm	Russian Federation
12.	30			60	+3	Zahedan	Iran
13.	60			90	+7	Krasnoyarsk	Russian Federation
14.	30			90	+8	Thimphu	Bhutan
15.	60			120	+9	Yakutsk	Russian Federation
16.	30			120	+8	Hangzhou	China
17.	0			120	+8	Makassar	Indonesia
18.		30		120	+8	Kalgoorlie	Australia
19.	60			150	+11	Magadan	Russian Federation
20.		30		150	+10	Dubbo	Australia

In the paper, the analysis was performed for sandy soil whose thermophysical characteristics are given in Table 2.

Table 2

Thermophysical characteristics of sandy soil

Thermal conductivity, W/(m·K)	Heat capacity, J/(kg·K)	Density, kg/m^3	Reflection factor (albedo), %	Radiation factor, %
0.52	770	1200	30 – 35	0.9

Analysis of the results and their discussion

Computer simulation was used to obtain temperature distributions in sandy soil with a dynamic effect on its surface of solar radiation thermal power at different depths from the surface to the depth of 2 m every 10 cm in different geographic coordinates.

As was stated in [9], the temperature on the soil surface has the greatest amplitude of vibration. With the depth increase, these vibrations decay and at the depth of 50 cm they are practically absent. So, subsequent calculations were performed just for the temperature difference created between the soil surface and its value at the depth of 50 cm.

Specific thermal flux passing through the soil surface to the depth of 50 cm can be determined by means of expression:

$$q = \kappa \frac{(T_2 - T_1)}{L}, \tag{5}$$

where κ, L are thermal conductivity and sandy soil layer thickness, respectively; T_1, T_2, are temperatures of the soil surface and at the depth of 50 cm, respectively.

To calculate the efficiency of underground thermoelectric generator, one can use the expression

$$\eta = \frac{1}{4}\frac{(T_2 - T_1)}{T_2} Z \frac{(T_2 + T_1)}{2}, \tag{6}$$

where Z is the figure of merit of thermoelectric material which for calculations was $3 \cdot 10^{-3}$ K^{-1}. According to [12], the divergence between the efficiency in formula (6) and the exact values usually does not exceed 10 %.

Thus, from the formula

$$W = \eta q, \tag{7}$$

one can determine specific electric power W that can be obtained from underground thermoelectric generator.

Integration by the formula

$$A = \int_0^{\tau} \eta q(t) dt, \tag{8}$$

of the electric power (7) yields the value of total specific energy that can be obtained from underground generator within the day ($\tau = 24$ h). The calculations were based on the mean monthly values of ambient temperature, so the specific energy during the month was determined as the product of produced diurnal energy on the number of days in respective month. Fig. 2 gives the results of calculation of specific electric energy that can be produced by underground thermoelectric generator throughout the year in sandy soil for different latitudes.

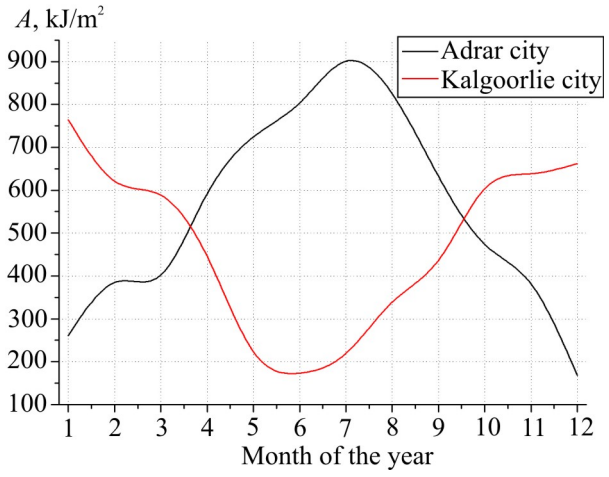

Fig. 2. Annual variation of specific electric energy of underground thermoelectric generator at the North (Adrar city) and South (Kalgoorlie city) latitudes.

Fig. 2 clearly shows annual amplitude variations and seasonality at different latitudes.

Fig. 3 gives mean monthly values of specific electric energy that can be obtained from underground thermoelectric generator along equatorial zone at different geographic longitudes (*a*) and along the latitude for 30^0 and 120^0 of East longitude (*b*), where sign «-» corresponds to West longitude and South latitude.

Analyzing Fig. 3 *a* it may be noted that the mean value of specific electric energy is 538 kJ/m^2 in which case the deviation along equatorial zone does not exceed 4 %. Fig. 3 *b* shows a clear latitude dependence of specific electric energy, which is attributable to the value of thermal radiation obtained throughout the year as a result of the position of the Sun. The slight deviation of the values from the longitude can be explained by climatic conditions of certain region.

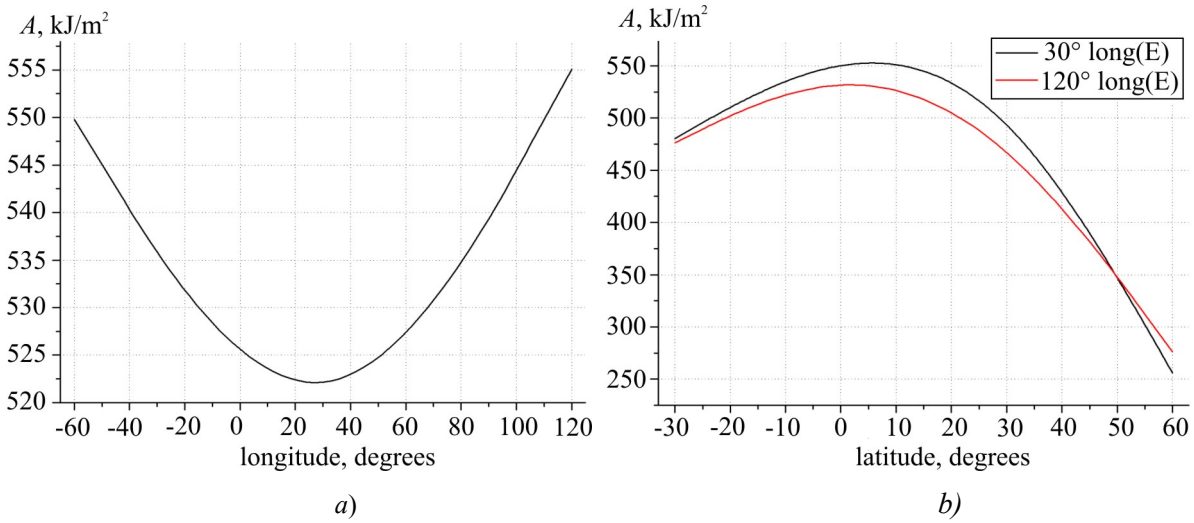

Fig. 3. Mean monthly values of specific electric energy that can be obtained from underground thermoelectric generator along equatorial zone at different geographic longitudes (a) and along latitude for 30^0 and 120^0 East longitude (b).

Fig. 4 shows the distribution of specific electric energy that can be obtained from underground thermoelectric generator throughout the year in different geographic coordinates.

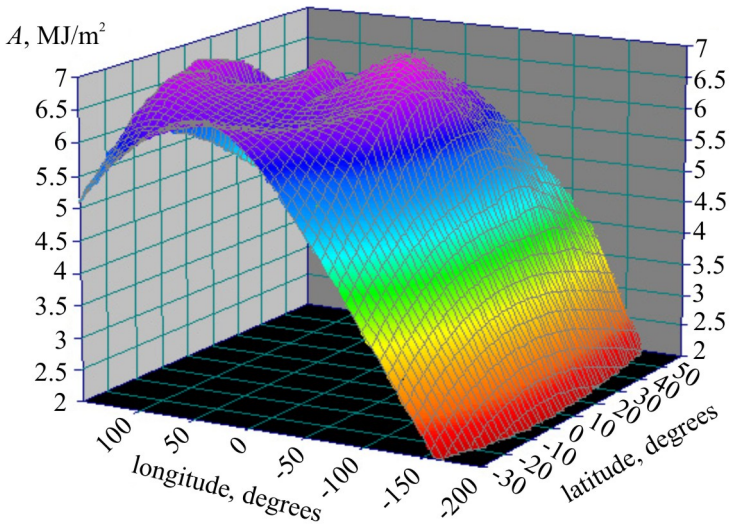

Fig. 4. Specific electric energy that can be obtained from underground thermoelectric generator throughout the year in different geographic coordinates.

On the basis of Fig. 4 one can determine the approximate values of electric energy that can be obtained from underground thermoelectric generators in any region which allows evaluating the efficiency and expedience of their use.

Conclusions

1. Maximum possible values of specific electric energy that can be obtained throughout the year and on a monthly basis from underground thermoelectric generators in different geographic coordinates were calculated which makes it possible to evaluate the efficiency of their use.
2. It was established that the mean value of specific electric energy throughout the year along equatorial zone is 538 kJ/m^2 and the deviation at different latitudes does not exceed 4 %.

3. It was determined that the mean value of specific electric energy along latitude is 400 kJ/m^2 and the deviation at different longitudes does not exceed 6 %.

References

1. L.I.Anatychuk, P.D.Mykytyuk, Thermal Generators Using Thermal Flows in Soils, *J.Thermoelectricity* 3, 86 – 95 (2003).
2. P.D.Mykytyuk, Devices for Thermoelectric Conversion of Thermal Energy of Soil, *Thesis for PhD in Physics and Mathematics:* 01.04.01, 2004 p.
3. P.D.Mykytyuk, N.S.Petrenko, Thermoelectric Power Supply Using the Heat of Soil, *J.Thermoelectricity* 2, 73 – 80 (2003).
4. P.D.Mykytyuk, V.O.Dudal, Testing Area for Studies of Renewable Thermoelectric Generators in Soil, *Scientific Herald of Chernivtsi University: Proceedings. Physics. Electronics*, Vol.4, Issue 1 (Chernivtsi: Chernivtsi National University, 2015), p. 54 – 59.
5. V.O.Dudal, Peculiarities of Using Soil Thermoelectric Generators and Thermoelectric Converters for Them, *Scientific Herald of Chernivtsi University: Proceedings. Physics. Electronics,* Vol 3, Issue 2 (Chernivtsi: Chernivtsi National University, 2014), p. 75 – 81.
6. P.D.Mykytyuk, Thermal Generators with Renewable Sources of Thermal Energy, *Avtonomnaya Energetika* 26, 61 – 68 (2009).
7. V.A.Kovda, B.G.Rozanova, *Soil Science, Part 1, Soil and Pedogenesis* (Moscow: Vysshaya Shkola, 1988), 400 p.
8. V.A.Kovda, B.G.Rozanova, *Soil Science, Part 2, Types of Soils, their Geography and Use* (Moscow: Vysshaya Shkola, 1988), 368 p.
9. V.O.Dudal, R.V.Kuz, Temperature Distributions in Soil and Possibilities of Underground Thermoelectric Generators, *J.Thermoelectricity* 2, 59 – 65 (2016).
10. *Comsol Multiphysics User's Guide* (COMSOLAB, 2010), 804 p.
11. https://rp5.ua.
12. L.I.Anatychuk, *Thermoelements and Thermoelectric Devices. Reference Book* (Kyiv:Naukova Dumka, 1979), 767 p.

Submitted 25.05.2016.

V.V. Lysko

V.V. Lysko

Institute of Thermoelectricity of the NAS and MES of Ukraine,
1, Nauky Str., Chernivtsi, 58029, Ukraine

ANALYSIS OF ERRORS IN DETERMINING THE THERMOELECTRIC PROPERTIES OF MATERIALS BY THE HARMAN METHOD

The results of computer studies of the Harman method accuracy for comprehensive determination of the figure of merit, thermoEMF, electric conductivity and thermal conductivity of thermoelectric materials in the temperature range of 30 – 500 °C were presented. A computer model of the Harman method based on a real physical model was developed. Analysis of possible errors of the method for the case of determining the properties of Bi-Te thermoelectric material was made. The results of calculations of measurement errors due to sample heat exchange with the environment through current conductors and thermocouples, as well as heat exchange by radiation were presented. The possibility of reducing the errors by introducing corrections was considered. Residual values of measurement errors due to inaccuracy in determining these corrections were determined.

Key words: measurements, Harman method, figure of merit, thermoEMF, electric conductivity, thermal conductivity, errors.

Introduction

General characterization of the problem. Progress in thermoelectricity is directly related to increase in the efficiency of thermoelectric power converters which, in turn, is governed by the figure of merit of material of which they are made. For selection of material composition and its optimization for a specific practical task it is necessary to establish clear connection between material properties and its fabrication technique. In so doing, the methods and equipment for measuring material properties will be of vital importance.

Until now in most cases use is made of methods for measuring on different samples the electric conductivity σ, thermoEMF α and thermal conductivity κ [1 – 5] which make it possible to determine by calculation the figure of merit Z of thermoelectric material

$$Z = \frac{\alpha^2 \sigma}{\kappa}. \qquad (1)$$

However, finding the figure of merit Z in this way is accompanied by considerable reduction of accuracy as compared to the accuracy of determination of σ, α, κ at least for two reasons.

First, in the calculation of Z by formula (1) in conformity with theory of errors [6] the values of errors are added

$$\delta Z = 2\delta\alpha + \delta\sigma + \delta\kappa,$$

where δ Z is the error in determining Z; δα, δσ, δκ the errors in determining σ, α, κ , respectively.
As long as these errors are approximately δα = 1 – 2 %, δσ = 3 – 5 %, δκ = 5 – 7 %, the error in determining Z can reach δZ = 10 – 16 %.

Second, measurements of σ, α, κ conducted on various samples that are not identical are the cause for additional errors related to inhomogeneity of the source material of which the samples are made. As a result of inhomogeneity, measurements of σ, α, κ are actually performed on the samples with different thermoelectric properties, through supposed to be identical. In so doing, the greater inhomogeneity of the source material, the larger in proportion is the error in determining *Z*. Moreover, there will be errors in determining the geometry of the samples and the distances between potential and temperature probes (thermocouples) that will be also different when measuring different samples.

These errors can be considerably reduced when measuring σ, α, κ on the same sample.

Analysis of the literature. As far back as the 50-s of the last century T.C. Harman proposed a method for direct measurement of the figure of merit of thermoelectric materials, subsequently named after him [7, 8]. This method allows measuring directly the figure of merit of material. For this purpose the sample under study is mounted in the thermostat on two conductors (Fig. 1). The electrically and thermally conducting contacts which create homogeneous thermal and electrical fields in the sample are mounted at the sample ends.

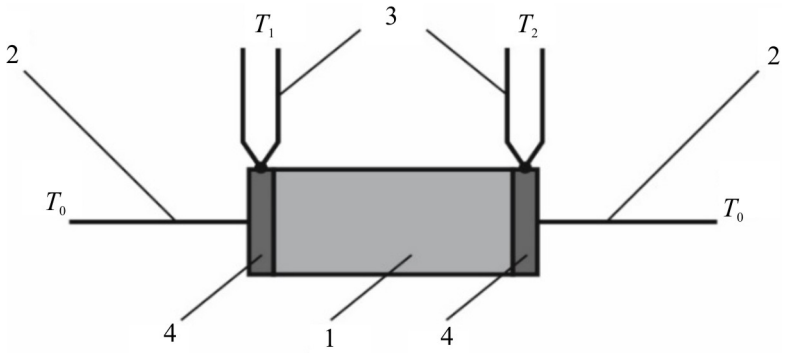

Fig. 1. Schematic of the Harman method
1 – sample; 2 – current conductors; 3 – thermocouples; 4 – contacts.

The measurements reduce to determination of potential difference $U_{\approx}$ on the contacts on the passage of an alternating current through the sample and potential difference $U_{=}$ on the passage of a direct current. With the identical values of alternating and direct currents *I*

$$Z = \frac{1}{T}\frac{U_{=} - U_{\approx}}{U_{\approx}}, \tag{2}$$

where *T* is average sample temperature.

Moreover, the Harman method allows finding the values of α, σ and κ on this very sample.

The Seebeck coefficient is found from the formula

$$\alpha = \frac{U_{=} - U_{\approx}}{\Delta T}, \tag{3}$$

where ΔT is temperature difference $T_1 - T_2$ at the sample ends on the passage of a direct current.

The electric conductivity of sample material is determined from expression

$$\sigma = \frac{I_{\approx}}{U_{\approx}}\frac{l}{S}, \tag{4}$$

where $I_{\approx}$ is the value of an alternating current, *l* is sample length, *S* is sample cross-section.

The thermal conductivity of material is found from the Fourier law

$$\kappa = \frac{\alpha I_{=} T}{\Delta T} \frac{l}{S}. \tag{5}$$

The errors in the Harman method are primarily due to the assumption of an idealized model of sample surfaces adiabaticity which cannot be realized in measurements. The reason for this is the presence of a number of heats which are not taken into account in formula (2). Among them – the Joule heats in the sample, in the contacts and conductors through which electric current is supplied to the sample, thermal fluxes through the conductors from the sample to the thermostat, etc. In order to reduce measurement errors, one must take into account their influence by introducing corrections γ_i into formula (2) for the calculation of the figure of merit, namely

$$Z = \frac{1}{T} \frac{U_{=} - U_{\approx}}{U_{\approx}} \left(1 + \sum_i \gamma_i \right). \tag{6}$$

Thus, the main complexity of this method is the necessity to determine correction factors, for which purpose one should know a large number of parameters, namely the emissivity factors of the sample, contact plates and conductors, their temperature dependences, precise values of the electric conductivity and thermal conductivity of conductor materials, etc.

Therefore, *the purpose of this paper* is to establish real values of possible errors of the Harman method with regard to corrections for heat exchange between the sample and the thermostat, as well as the influence of errors in the determination of corrections on the residual measurement error.

Physical and computer models of the Harman method

A real physical model of the Harman method is shown in Fig. 2.

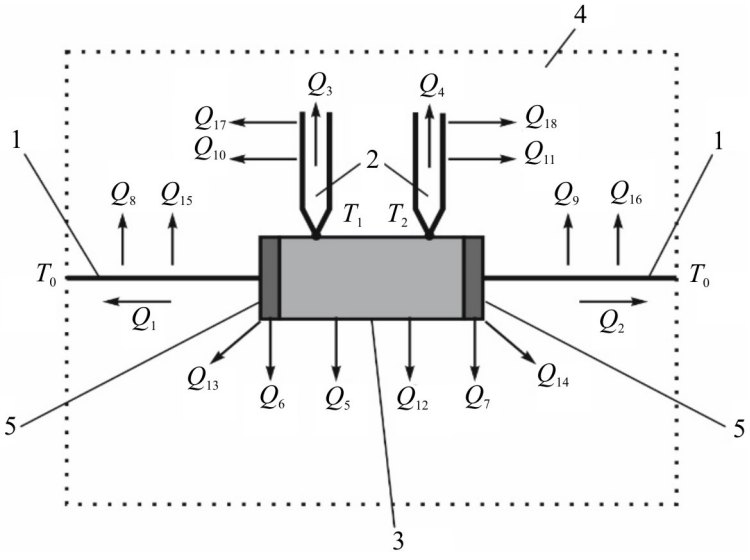

Fig. 2. A real physical model of the Harman method 1 – current conductors, 2 – thermocouples, 3 – sample, 4 – thermostat, 5 – contacts.

The steady-state conditions are created in the sample by virtue of balance of a number of heats, namely the Peltier heat on the contacts, the Joule heat generated in the sample, the contacts and the conductors along which electric current is supplied to the sample, heat flux in the sample and heat fluxes to thermostat with temperature T_0 through current conductors, thermocouple conductors and by heat exchange due to convection and radiation.

Thus, in addition to the Peltier heat one must take into account the Joule heat, the Thomson heat and several more heat fluxes:
Q_1, Q_2 – heat exchange between the sample and the thermostat through current conductors;
Q_3, Q_4 – heat exchange between the sample and the thermostat through thermocouple conductors;
Q_5 – heat exchange by radiation between the sample and the thermostat;
Q_6, Q_7 – heat exchange by radiation between the contacts and the thermostat;
Q_8, Q_9 – heat exchange by radiation between current conductors and the thermostat;
Q_{10}, Q_{11} – heat exchange by radiation between thermocouple conductors and the thermostat;
Q_{12} – convective heat exchange between the sample and thermostat;
Q_{13}, Q_{14} – convective heat exchange between the contacts and the thermostat;
Q_{15}, Q_{16} – convective heat exchange between current conductors and the thermostat;
Q_{17}, Q_{18} – convective heat exchange between thermocouple conductors and the thermostat.

The possibilities of excluding the above additional kinds of heat are extremely limited. High vacuum created around the sample is the only real condition that can improve this situation. In this case one can assume:

$$Q_{12} = Q_{13} = Q_{14} = Q_{15} = Q_{16} = Q_{17} = Q_{18} = 0. \tag{7}$$

As regards other heats (Q_1 – Q_{11}), most of them are practically inevitable, and one must estimate their influence on the measurement results and take into account as a series of corrections.

Calculation of the influence of these thermal fluxes on the error in measuring the figure of merit by the Harman method is a complicated mathematical problem that can be written a as system of second-order differential equations in partial derivatives

$$\begin{cases} -\nabla((\kappa_i + \alpha_i^2 \sigma_i T_i)\nabla T_i) - \nabla(\alpha_i \sigma_i T_i \nabla U_i) - \alpha_i((\nabla U_i)^2 + \alpha_i \nabla T_i \nabla U_i) = 0 \\ \nabla\left(\sigma_i \nabla U_i\right) + \nabla(\sigma_i \alpha_i \nabla T_i) = 0, \quad i = 1, 2..5 \end{cases} \tag{8}$$

where σ_i, α_i, κ_i are electric conductivity, thermoEMF and thermal conductivity of physical model elements, U is electrical potential, T is temperature.

Solution of this system of equations with corresponding boundary conditions was obtained by means of computer simulation using Comsol Multiphysics application software package.

Computer simulation results

Determination of the figure of merit

The elaborated computer model was used to obtain the distributions of temperature and electric potential in the sample and the elements of measuring unit intended for determination of thermoelectric properties of material by the Harman method in the temperature range of 30 – 500 °C on the samples of *Bi-Te* based material of diameter 4 mm and length 10 mm. The obtained distributions allowed calculating possible errors in determining the figure of merit by the Harman method without regard to corrections, as well as the values of required corrections and the influence on them of information on the properties and geometry of sample, contacts, current conductors and thermocouples. The results of investigation are given below. If necessary, computer model allows reproducing these results for other materials, temperature ranges and sample dimensions.

Total error in determining the figure of merit Z versus temperature is given in Fig. 3. This dependence was obtained for the case of measurements without regard to correction factors. As is

seen from the plot, the error in determining the figure of merit at room temperature is a little more than 10 % and greatly increases with a rise in temperature. As mentioned above, these errors can be taken into account by introducing into the formula for calculating the figure of merit the correction factors taking into account heat exchange between the sample and the measuring unit elements. However, this requires information on a large number of values characterizing measuring unit, namely precise geometrical dimensions of current conductors, thermocouples and contacts, their thermal conductivity, electric conductivity, thermoEMF, emissivity, thermostat temperature, etc. The errors in determining these values will have a direct influence on the error in determining corrections, hence the figure of merit of the sample. The results of computer simulation of this influence are given below in the form of dependences of errors in determining corrections $\delta\gamma_i$ on the errors in measuring each of the values necessary for their calculation.

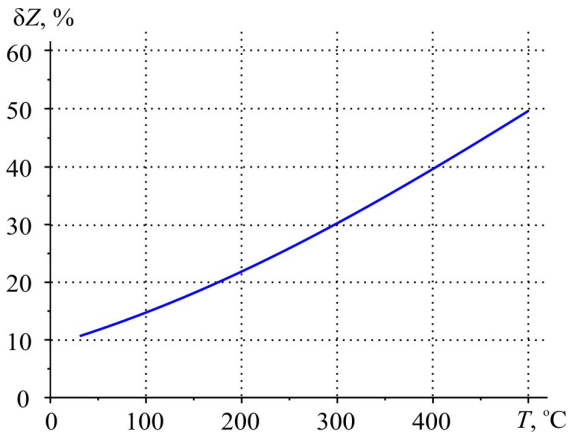

Fig. 3. Total error in determining the figure of merit Z by the Harman method without regard to corrections versus temperature.

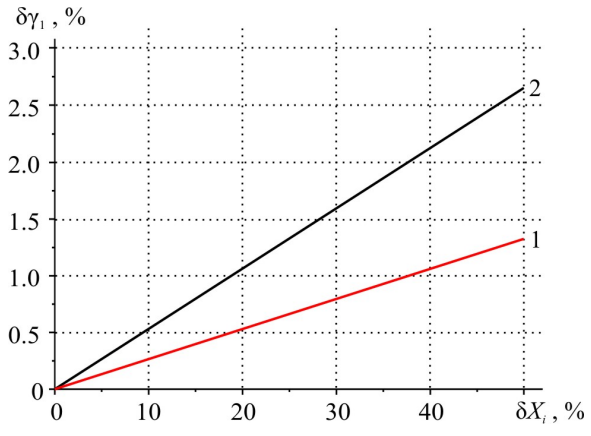

Fig. 4. The error in determining correction γ_1 for heat exchange through current conductors versus the errors in measuring their length L_1, diameter d_1, thermal conductivity κ_1 and temperature difference ΔT_1. δX_i: 1 – δL_1, $\delta\kappa_1$, $\delta(\Delta T1)$; 2 – δd_1.

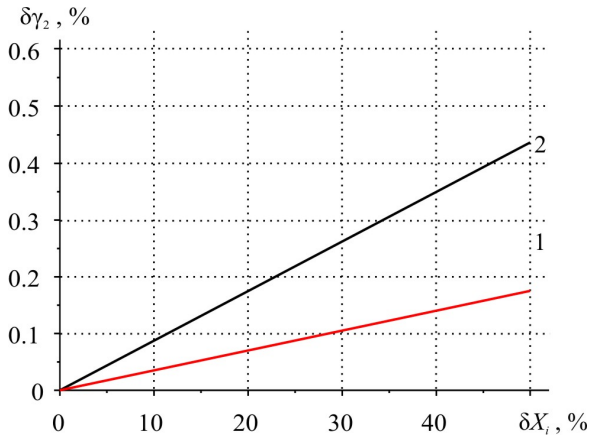

Fig. 5. The error in determining correction γ_2 for heat exchange through thermocouple conductors versus the errors in measuring their lengths L_2 and L_3, diameters d_2 and d_3, thermal conductivities κ_2 and κ_3 and temperature differences ΔT_2 and ΔT_3. δX_i: 1 – δL_2, δL_3, $\delta\kappa_2$, $\delta\kappa_3$, $\delta(\Delta T_2)$, $\delta(\Delta T_3)$; 2 – δd_2, δd_3.

Fig. 4, 5 show the errors in determining corrections for heat exchange through current conductors, as well as chromel-alumel thermocouple conductors versus the errors in measuring their lengths, diameters and temperature differences.

Further shown are the errors in determining corrections related to radiation from the surface of sample (Fig. 6, 7), contacts (Fig. 8, 9), current conductors and thermocouple conductors (Fig. 10, 11). The figures show the errors in determining corrections versus the errors in measuring the geometry and emissivity of physical model elements for three values of thermostat temperature – 30, 250 and 500 °C.

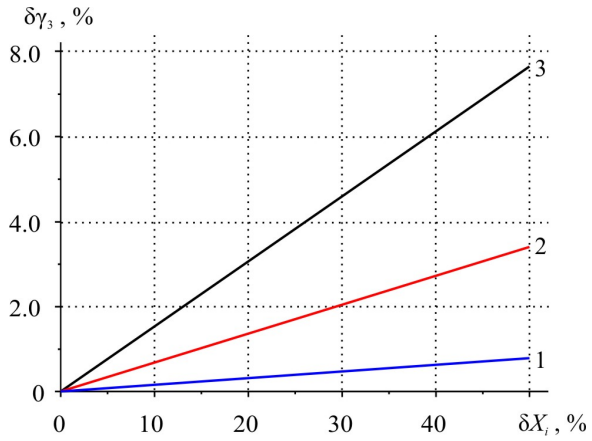

Fig. 6. The error in determining correction γ_3 for heat exchange by radiation between sample and thermostat versus the errors in measuring sample length L_3 and diameter d_3 , sample emissivity ε_3 and thermostat emissivity ε_4. 1 – 30 °C, 2 – 250 °C, 3 – 500 °C. δX_i: δL_3, δd_3, $\delta\varepsilon_3$, $\delta\varepsilon_4$.

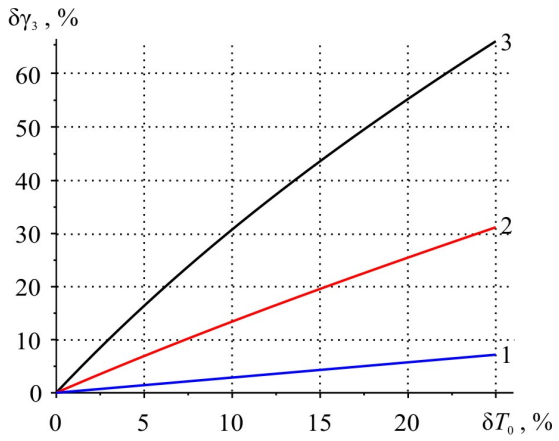

Fig. 7. The error in determining correction γ_3 for heat exchange by radiation between sample and thermostat versus the error in measuring thermostat temperature T_0. 1 – 30 °C, 2 – 250 °C, 3 – 500 °C.

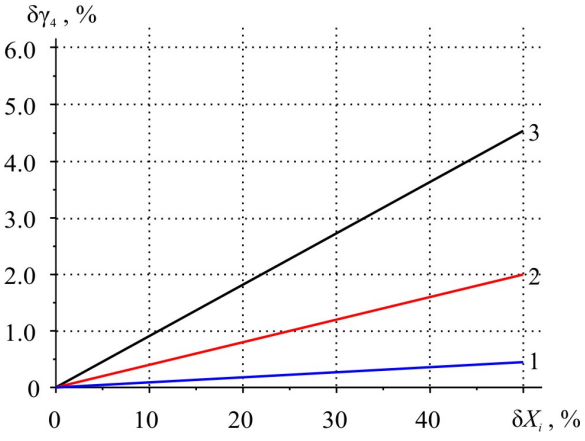

Fig. 8. The error in determining correction γ_4 for heat exchange by radiation between contacts and thermostat versus the errors in measuring thickness L_5 and diameter d_5 of contacts, contact emissivity ε_5 and thermostat emissivity ε_4. 1 – 30 °C, 2 – 250 °C, 3 – 500 °C. δX_i: δL_5, δd_5, $\delta\varepsilon_4$, $\delta\varepsilon_5$.

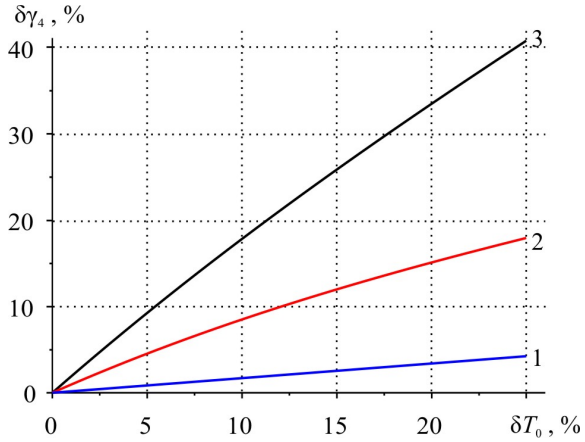

Fig. 9. The error in determining correction γ_4 for heat exchange by radiation between contacts and thermostat versus the error in measuring thermostat temperature T_0. 1 – 30 °C, 2 – 250 °C, 3 – 500 °C.

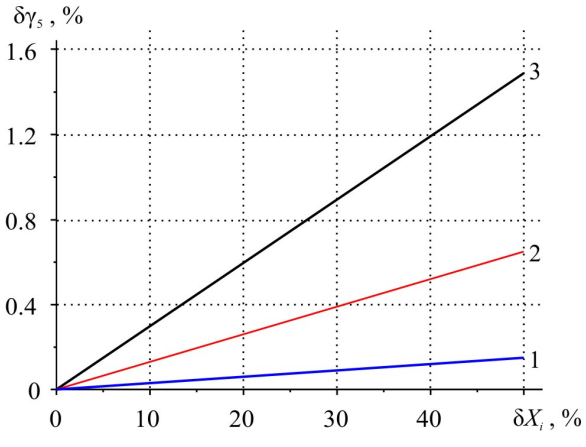

Fig. 10. The error in determining correction γ_5 for heat exchange by radiation between conductors (current and thermocouple) and thermostat versus the errors in measuring length L_6 and diameter d_6 of conductors, conductor emissivity ε_6 and thermostat emissivity ε_4. 1 – 30 °C, 2 – 250 °C, 3 – 500 °C. δX_i: δL_6, δd_6, $\delta\varepsilon_4$, $\delta\varepsilon_6$.

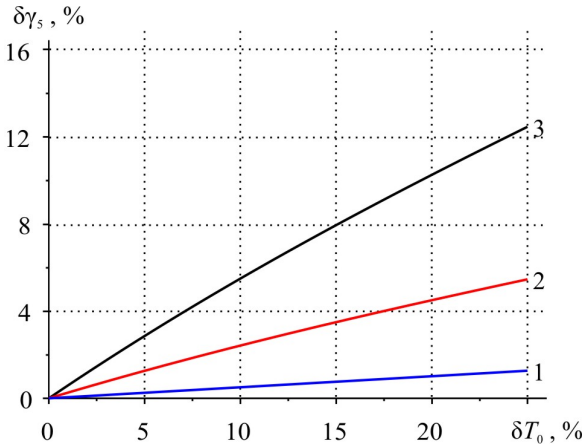

Fig. 11. The error in determining correction γ_5 for heat exchange by radiation between conductors (current and thermocouple) and thermostat versus the error in measuring thermostat temperature T_0. 1 – 30 °C, 2 – 250 °C, 3 – 500 °C.

From the above dependences one can obtain the expected total error in determining corrections for typical errors in measuring the values necessary for their calculation. The values of errors in determining these corrections are given in Table.

Table

Expected errors in determining corrections for the figure of merit calculation

№	Correction	Parameter	Parameter value	Parameter measurement error	Correction determination error
1	2	3	4	5	6
Temperature 30 °C					
1.	γ_1 – account of heat exchange through current conductors	Current conductor length, L_1, mm	30	3 – 5 %	0.09 – 0.14 %
		Current conductor diameter, d_1, mm	0.1	5 – 10 %	0.26 – 0.52 %
		Thermal conductivity of conductor material, κ_1, W/(m*K)	400	5 – 7 %	0.14 – 0.22 %
		Temperature difference on conductor, ΔT_1, °C	~ 2	~ 5 %	0.14 %
2.	γ_2 – account of heat exchange through thermocouple conductors	Conductor length, L_2, mm	50 mm	3 – 5 %	< 0.01 %
		Conductor diameter, d_2, mm	0.1 mm	5 – 10 %	0.02 – 0.08 %
		Thermal conductivity of conductor material, κ_2, W/(m*K) – chromel – alumel	 18 27	 5 – 7 % 5 – 7 %	 0.01 – 0.02 % 0.01 – 0.02 %
		Temperature difference on conductor, ΔT_2, °C	~ 2	~ 5 %	< 0.01 %

Table (continued)

1	2	3	4	5	6
3.	γ_3 – account of heat exchange by radiation between sample and thermostat	Sample length, L_3, mm	10	0.5 %	< 0.01 %
		Sample diameter , d_3, mm	4	0.25 %	< 0.01 %
		Sample emissivity, ε_3	0.7	20 – 30 %	0.28 – 0.42 %
		Thermostat emissivity, ε_3	0.7	20 – 30 %	0.28 – 0.42 %
		Thermostat temperature, T_0, °C	30	1 – 2 %	0.34 – 0.68 %
4.	γ_4 – account of heat exchange by radiation between contacts and thermostat	Contact thickness, L_4, mm	2	0.5 %	< 0.01 %
		Contact diameter, d_4, mm	4	0.25 %	< 0.01 %
		Contact emissivity, ε_4	0.7	20 – 30 %	0.16 – 0.24 %
		Thermostat emissivity, ε_4	0.7	20 – 30 %	0.16 – 0.24 %
		Thermostat temperature, T_0, °C	30	1 – 2 %	0.2 – 0.4 %
5.	γ_5 – account of heat exchange by radiation between conductors and thermostat	Length – current conductors, L_1, mm – thermocouple conductors, L_2, mm	 30 50	 3 – 5 % 3 – 5 %	 < 0.01 % < 0.01 %
		Diameter – current conductors, d_1, mm – thermocouple conductors, d_2, mm	 0.1 0.1	 5 – 10 % 5 – 10 %	 0.01 – 0.03 % 0.01 – 0.03 %
		Emissivity – current conductors, ε_1 – thermocouple conductors, ε_2	 0.7 0.7	 20 – 30 % 20 – 30 %	 0.06 – 0.09 % 0.06 – 0.09 %
		Thermostat emissivity, ε_4	0.7	20 – 30 %	0.06 – 0.09 %
		Thermostat temperature, T_0, °C	30	1 – 2 %	0.06 – 0.11 %
Sum $\gamma_1 – \gamma_5$, %					2.3 – 4.0 %
Temperature 250 °C					
1.	γ_1 – account of heat exchange through current conductors	Current conductor length, L_1, mm	30	3 – 5 %	0.08 – 0.12 %
		Current conductor diameter d_1, mm	0.1	5 – 10 %	0.21 – 0.42 %
		Thermal conductivity of conductor material, κ_1, W/(m*K)	385	5 – 7 %	0.09 – 0.19 %
		Temperature difference on conductor, ΔT_1, °C	~ 2	~5 %	0.12 %
2.	γ_2 – account of heat exchange through thermocouple conductors	Conductor length, L_2, mm	50 mm	3 – 5 %	< 0.01 %
		Conductor diameter, d_2, mm	0.1 mm	5 – 10 %	0.02 – 0.06 %
		Thermal conductivity of conductor material, κ_2, W/(m*K) – chromel – alumel	 22.7 32	 5 – 7 % 5 – 7 %	 < 0.01 % < 0.01 %
		Temperature difference on conductor, ΔT_2, °C	~ 2	~5 %	< 0.01 %
3.	γ_3 – account of heat exchange by radiation between sample and thermostat	Sample length, L_3, mm	10	0.5 %	0.03 %
		Sample diameter, d_3, mm	4	0.25 %	0.01 %
		Sample emissivity, ε_3	0.7	20 – 30 %	1.19 – 1.78 %
		Thermostat emissivity, ε_3	0.7	20 – 30 %	1.19 – 1.78 %
		Thermostat temperature, T_0, °C	250	1 – 2 %	1.45 – 2.9 %

Table (continued)

1	2	3	4	5	6
4.	γ_4 – account of heat exchange by radiation between contacts and thermostat	Contact thickness, L_4, mm	2	0.5 %	0.02 %
		Contact diameter, d_4, mm	4	0.25 %	0.01 %
		Contact emissivity, ε_4	0.7	20 – 30 %	0.68 – 1.02 %
		Thermostat emissivity, ε_4	0.7	20 – 30 %	0.68 – 1.02 %
		Thermostat temperature, T_0, °C	250	1 – 2 %	0.85 – 1.7 %
5.	γ_5 – account of heat exchange by radiation between conductors and thermostat	Length – current conductors , L_1, mm – thermocouple conductors, L_2, mm	 30 50	 3 – 5 % 3 – 5 %	 < 0.01 % < 0.01 %
		Diameter – current conductors, d_1, mm – thermocouple, d_2, mm	 0.1 0.1	 5 – 10 % 5 – 10 %	 0.04 – 0.12 % 0.04 – 0.12 %
		Emissivity – current conductors, ε_1 – thermocouple conductors, ε_2	 0.7 0.7	 20 – 30 % 20 – 30 %	 0.25 – 0.38 % 0.25 – 0.38 %
		Thermostat emissivity, ε_4	0.7	20 – 30 %	0.25 – 0.38 %
		Thermostat temperature, T_0, °C	250	1 – 2 %	0.25 – 0.46 %
Sum $\gamma_1 – \gamma_5$, %					7.7 – 13.1 %
Temperature 500 °C					
1.	γ_1 – account of heat exchange through current conductors	Current conductor length, L_1, mm	30	3 – 5 %	0.06 – 0.09 %
		Current conductor diameter, d_1, mm	0.1	5 – 10 %	0.17 – 0.34 %
		Thermal conductivity of conductor material, κ_1, W/(m*K)	366	5 – 7 %	0.07 – 0.15 %
		Temperature difference on conductor, ΔT_1, °C	~ 2	~5 %	0.17 %
2.	γ_2 – account of heat exchange through thermocouple conductors	Conductor length, L_2, mm	50 mm	3 – 5 %	< 0.01 %
		Conductor diameter, d_2, mm	0.1 mm	5 – 10 %	0.01 – 0.03 %
		Thermal conductivity of conductor material, κ_2, W/(m*K) – chromel – alumel	 27.8 37.5	 5 – 7 % 5 – 7 %	 < 0.01 % < 0.01 %
		Temperature difference on conductor, ΔT_2, °C	~ 2	~5 %	<0.01 %
3.	γ_3 – account of heat exchange by radiation between sample and thermostat	Sample length, L_3, mm	10	0.5 %	0.07 %
		Sample diameter, d_3, mm	4	0.25 %	0.04 %
		Sample emissivity, ε_3	0.7	20 – 30 %	2.72 – 4.07 %
		Thermostat emissivity, ε_3	0.7	20 – 30 %	2.72 – 4.07 %
		Thermostat temperature, T_0, °C	500	1 – 2 %	3.29 – 6.59 %
4.	γ_4 – account of heat exchange by radiation between contacts and thermostat	Contact thickness, L_4, mm	2	0.5 %	0.04 %
		Contact diameter, d_4, mm	4	0.25 %	0.02 %
		Contact emissivity, ε_4	0.7	20 – 30 %	1.55 – 2.33 %
		Thermostat emissivity, ε_4	0.7	20 – 30 %	1.55 – 2.33 %
		Thermostat temperature, T_0, °C	500	1 – 2 %	1.94 – 3.88 %

Table (continued)

1	2	3	4	5	6
5.	γ_5 – account of heat exchange by radiation between conductors and thermostat	Length – current conductors, L_1, mm – thermocouple conductors, L_2, mm	30 50	3 – 5 % 3 – 5 %	< 0.01 % < 0.01 %
		Diameter – current conductors, d_1, mm – thermocouple conductors, d_2, mm	0.1 0.1	5 – 10 % 5 – 10 %	0.09 – 0.26 % 0.09 – 0.26 %
		Emissivity – current conductors, ε_1 – thermocouple conductors, ε_2	0.7 0.7	20 – 30 % 20 – 30 %	0.58 – 0.87 % 0.58 – 0.87 %
		Thermostat emissivity, ε_4	0.7	20 – 30 %	0.58 – 0.87 %
		Thermostat temperature, T_0, °C	500	1 – 2 %	0.58 – 1.12 %
Sum $\gamma_1 - \gamma_5$, %					16.9 – 28.6 %

From Table it follows that the expected total error in determining corrections for typical errors in measuring the values necessary for their calculation will increase with a rise in temperature from ~ 2.3 – 4.0 % at room temperature to ~ 16.9 – 28.6 % at 500 °C (for the above indicated geometrical dimensions of sample and measuring unit elements).

The error in measuring figure of merit by the Harman method, apart from the errors in determining corrections for heat exchange with the environment, will also include other errors, namely the errors in measuring voltages $U_{\approx}$ (~ 1.5 %), $U_{=}$ (~ 0.1 %) and average temperature of sample (~ 0.5 %). Therefore, total error in measuring figure of merit by the Harman method will make from ~ 4.4 – 6.1 % at room temperature to ~ 19 – 30.7 % at 500 °C.

Determination of thermoEMF, electric conductivity and thermal conductivity

There were also calculated possible errors in determining by the Harman method of other thermoelectric parameters of material, namely thermoEMF, electric conductivity and thermal conductivity.

The errors in measuring thermoEMF and electric conductivity are mainly governed by instrumental errors in measuring the values which enter into formulae (3) and (4) – the errors in measuring voltage $U_{\approx}$ on the passage of an alternating current through the sample (~ 1.5 %), voltage $U_{=}$ on the passage of a direct current through the sample (~ 0.15 %), sample length (~ 0.25 %), sample cross-sectional area (~ 0.5 %), temperature difference on the sample (~ 3 %), the Seebeck coefficient of chromel (~ 2 %), the value of an alternating current $I_{\approx}$ (~ 0.5 %).

Additional error is measuring electric conductivity is also introduced by current density inhomogeneity in the sample (~ 1 %). As regards the influence of thermoEMF on electric conductivity measurement, the use of an alternating current due to thermal inertia at not very low frequencies eliminates the influence of the Peltier effect on temperature distribution in the sample and, accordingly, the influence of thermoEMF on the measurements.

Thus, total error in measuring the Seebeck coefficient will make ~ 6.7 %, electric conductivity ~ 3.8 %.

The situation with thermal conductivity measurement is more difficult. As in the case of the

figure of merit, the errors in determining thermal conductivity will depend on the accuracy of finding corrections for heat exchange between the sample and the environment. The resulting distributions of temperature and electric potential in the sample and measurement unit elements allowed calculating possible errors in measuring thermal conductivity by the Harman method without regard to corrections, the values of the necessary corrections and the influence on them of precise information on the properties and geometry of sample, contacts, current conductors and thermocouples. The error in measuring thermal conductivity related to thermal losses versus temperature is shown in Fig. 12.

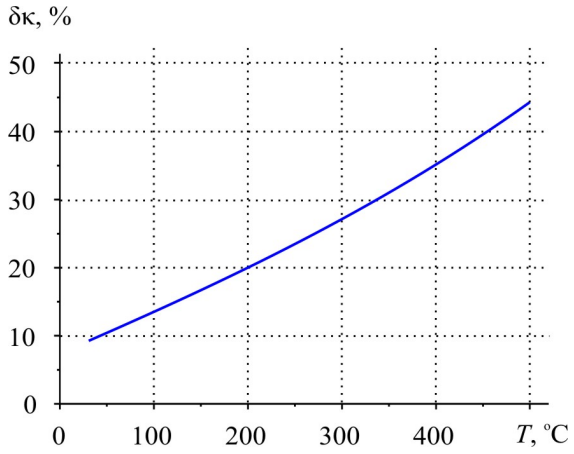

Fig. 12. Total error in determining thermal conductivity by the Harman method versus temperature (without regard to corrections).

The error in determining thermal conductivity at room temperature is of the order of 9.5 % and, similar to the error in measuring figure of merit, increases with a rise in temperature to ~ 45 % at 500 ºC. These errors can be reduced by introducing corrections. Dependences of the accuracy in determining these corrections on the accuracy in measuring the values necessary for their calculation were obtained. It was established that total error in determining corrections for thermal conductivity calculation by the Harman method increases from ~ 2.2 – 3.7 % at room temperature to ~ 15.3 – 26 % at 500 °C. The error in measuring thermal conductivity, apart from the errors in determining corrections for heat exchange with the environment, will also include the errors in measuring sample length (~ 0.25 %), cross-sectional area (~ 0.5 %), voltages $U_{\sim}$ (~ 1.5 %) and $U_{=}$ (~ 0.1 %), current $I_{=}$ (~ 0.1 %), sample average temperature (~ 0.5 %) and temperature difference on sample (~ 3 %). Total error in measuring thermal conductivity by the Harman method will make from ~ 8.2 – 9.7 % at room temperature to ~ 21.3 – 32 % at 500 °C.

Thus, the possibility of using the Harman method for a comprehensive determination of thermoelectric properties of material is essentially restricted by the necessity to know additional accurate information on many values, as well as by a narrow range of temperatures with acceptable values of measurement errors.

Conclusions

1. By computer simulation of a real physical model of the Harman method it was established that the error in determining the figure of merit of thermoelectric materials based on *Bi-Te* by this method at room temperature is ~ 10 % and drastically increases with a rise in temperature to ~ 50 % at 500 °C.

2. The influence of the accuracy of information on the geometry and physical properties of the sample and measuring unit elements on the accuracy of determining corrections for the figure of merit calculation was determined. It was established that total error in determining corrections for the case of measuring the figure of merit of thermoelectric materials based on *Bi-Te* and typical errors in measuring the values necessary for calculation of these errors increases from ~ 2.3 – 4.0 % at room temperature to ~ 16.9 – 28.6 % at 500 °C. Total error in measuring the figure of merit with regard to instrumental errors of measured values is from ~ 4.4 – 6.1 % at room temperature to ~ 19 – 30.7 % at 500 °C.
3. Possible errors in measuring other thermoelectric properties by the Harman method were evaluated. It was established that total error in measuring the Seebeck coefficient is ~ 6.7 %, electric conductivity ~ 3.8 %, thermal conductivity – from ~ 8.2 – 9.7 % at room temperature to ~ 21.3 – 32 % at 500 °C.

References

1. L.I.Anatychuk, *Thermoelements and Thermoelectric Devices* (Kyiv: Naukova Dumka, 1979), 768 p.
2. H. Czichos, T. Saito, and L. Smith*, Springer Handbook of Metrology and Testing* (Springer, 2011), 1500 p.
3. T.Tritt, Electrical and Thermal Transport Measurement Techniques for Evaluation of the Figure-of-Merit of Bulk Thermoelectric Materials, in: *Thermoelectric Handbook: Macro to Nano, ed.by D.M. Rowe* (CRC Press, 2006).
4. L.I.Anatychuk, S.V.Pervozvansky, and V.V.Razinkov, Precise Measurement of Cooling Thermoelectric Material Parameters: Methods, Arrangements and Procedures, *Proc. of the 12th Intern. Conf. Thermoelectrics (Japan, 1993),* pp. 553 – 564.
5. A.S.Okhotin, A.S.Pushkarsky, R.P.Borovikova, and V.A.Simonov, *Methods for Measuring Characteristics of Thermoelectric Materials and Converters* (Moscow: Nauka, 1974).
6. E.S.Polischuk, M.M.Dorozhovets, V.O.Yatsuk et al., Metrology and Measuring Equipment, Ed. by prof. E.S.Polischuk (Lviv: Beskyd Bit Publ., 2004), 544p.
7. T.C. Harman, J.H. Cahn, and M.J. Logan, Measurement of Thermal Conductivity by Utilization of the Peltier Effect, *J. Applied Physics* **30**(9), 1351 – 1359 (1959).
8. *US 2994818*, T.C.Harman, Method and Apparatus for Measuring Thermoelectric Properties, 1959.

Submitted 28.03.2016.

NEWS
OF INTERNATIONAL THERMOELECTRIC ACADEMY

BOGDAN IVANOVYCH STADNYK

(Dedicated to 80th birthday)

Bogdan Ivanovych Stadnyk, Doctor of Science in Engineering, professor, academician of Ukrainian Academy of Engineering Sciences, academician of the International Thermoelectric Academy, Director of the Institute of Computer Technologies, Automation and Metrology at the National University "Lvivska Politechnika", Head of Department of Information Measurement Technology, has celebrated his glorious 80th anniversary.

Bogdan Ivanovych Stadnyk was born on June 1, 1936 in Hirne village, Stryi district in the Lviv region. In 1958 he graduated from Lviv Polytechnic Institute.

He began his research activity at Scientific and Production Association "Thermoprylad" to study thermoelectric characteristics of different materials used with change in temperature. Later on, in cooperation with G.V. Samsonov and P.S. Kyslyi, academicians of the Academy of Sciences of Ukraine, he studied in detail the thermoelectric characteristics of metal-ceramic semiconductor materials to be used for measuring high temperatures in aggressive environments.

The main lines of the numerous scientific research and practical developments pursued by the scientist are as follows:

– creation of temperature measuring instruments with the use of thermoelectric effects;

– development of theoretical basis and practical methods for investigation of thermoelectric effects;

– simulation and study of interaction between the conversion error of thermoelectric temperature sensors and the gradient of their internal mechanical stresses.

Professor B.I. Stadnyk leads the scientific school of means for measuring physical quantities which laid theoretical, technological and metrological foundations for the creation of new instruments and systems of temperature measurement, namely development of a new direction founded by him – the problems of interaction between the errors of primary transducers of physical quantities and the gradients of their internal mechanical stresses, the ways for their reduction.

Ukrainian scientist shared his achievements with the researchers during his business trips to France, Germany, Poland, Hungary, at numerous international scientific conferences, seminars and symposiums.

B.I. Stadnyk is the author of over 450 scientific works – monographs, papers, patents and inventions. Bogdan Ivanovych is chairman of Specialized Council on Doctoral Theses in the National University "Lvivska Politechnika". Under his supervision 32 PhD and 10 Doctoral Theses have been defended.

For his selfless work of many years a well-known scientist, honoured inventor of Ukraine B.I. Stadnyk was awarded with two orders, numerous medals, diplomas, lapel badges, honorary titles and premiums.

International Thermoelectric Academy, Institute of Thermoelectricity of the National Academy of Sciences and Ministry of Education and Science of Ukraine, “Journal of Thermoelectricity” Publishers cordially greet the esteemed Bogdan Ivanovych Stadnyk, sincerely wishing him sound health, happy longevity and new creative achievements.

ARTICLE PREPARATION RULES

The article shall conform to the journal profile. The article content shall be legible, concise and have no repetitions.

The article shall be submitted to the editorial board in electronic version.

The text shall be typed in text editor not lower than MS Word 6.0/7.0.

Page setup: "mirror margins"- top margin – 2.5 cm, bottom margin – 2.0 cm, inside – 2.0 cm, outside– 3.0 cm, from the edge to page header – 1.27 cm, page footer – 1.27 cm.

Graphic materials, pictures shall be submitted in color or, as an exception, black and white, in .opj or .cdr formats, .jpg or .tif formats being also permissible. According to author's choice, the tables and partially the text can be also in color.

The article shall be submitted in English on A4 paper sheets; the number of pages shall not exceed 12. By agreement with the editorial board, the number of pages can be increased.

To accelerate publication of the article, please adhere to the following rules:

- the authors' initials and names are arranged in the centre of the first page at the distance of 1 cm from the page header, font Times New Roman, size 12 pt, line spacing 1.2;
- the name of organization, address (street, city, postal code, country) – indent 1 cm below the authors' initials and names, font Times New Roman, size 11 pt, line spacing 1.2, center alignment;
- the title of the article is arranged 1 cm below the name of organization, in capital letters, semi-bold, font New Roman, size 12 pt, line spacing 1.2, center alignment. The title of the article shall be concrete and possibly concise;
- the abstract is arranged 1 cm below the title of the article, font Times New Roman, size 10 pt, in italics, line spacing 1.2 ,center alignment;
- key words are arranged below the abstract, font Times New Roman, size 10 pt, line spacing 1.2, justified alignment. The title "Key words" – font Times New Roman, size 10 pt, semi-bold;
- the main text of the article is arranged 1 cm below the abstract, indent 1 cm, font Times New Roman. size 11 pt, line spacing 1.2, justified alignment;
- formulae are typed in formula editor, fonts Symbol, Times New Roman. Font size is "normal" – 12 pt, "large index" – 7 pt, "small index" – 5 pt, "large symbol" – 18 pt, "small symbol" – 12 pt). The formula is arranged in the text, centre aligned and shall not occupy more than 5/6 of the line width, formulae are numbered in round brackets right;
- dimensions of all quantities used in the article are represented in the International System of Units (SI) with the explication of the symbols employed;
- figures are arranged in the text. The figures and pictures shall be clear and contrast; the plot axes – parallel to sheet edges, thus eliminating possible displacement of angles in scaling;
- tables are arranged in the text. The width of the table shall be 1 cm less than the line width. Above the table its ordinary number is indicated, right alignment. Continuous table numbering throughout the text. The title of the table is arranged below its number, center alignment;
- references should appear at the end of the manuscript. References within the text should be enclosed in square brackets. References should be numbered in order of first appearance in the text. Examples of various reference types are given below.

– L.I. Anatychuk, *Thermoelements and Thermoelectric Devices: Handbook* (Kyiv: Naukova Dumka, 1979), p.766. (Book)
– T.M. Tritt, Thermoelectric Phenomena, Materials, and Applications, *Annual Review of Materials Research* **41**, 433 (2011). (Journal paper)
– U. Ghoshal, *Proceedings of the XXI International Conference on Thermoelectrics* (N.Y., USA, 2002), p. 540. (Proceedings Conference)

The article should be supplemented by:

• letter from the organization where the work was performed or from the authors of the work applying for the publication of the article;

• information on the author (authors): last name and initials; full name and postal address of the institution where the author works; academic degree; position; telephone number; E-mail;

• author's (authors') photo in color or, as an exception, in black and white. With the number of authors more than two their photos are not given;

• author's application to the following effect:

We, the undersigned authors, … transfer to the founders and editors of "Journal of Thermoelectricity" the right to publish the article…in Ukrainian, Russian and English. This is to confirm that the present publication does not violate the copyright of other persons or organizations.

Date Signatures